



Kansai Institute for Photon Science  
National Institutes for Quantum Science and Technology



**KPSI**  
**ANNUAL**  
**REPORT**  
**2023**



# Contents

<b>Preface</b> .....	<b>1</b>
<b>Activities of KPSI</b> .....	<b>4</b>
<b>User Facilities</b> .....	<b>10</b>
<b>Research Highlights</b> .....	<b>16</b>
<b>Publication Lists</b> .....	<b>62</b>
<b>The Kids' Science Museum of Photons</b> .....	<b>76</b>
<b>Appendix</b> .....	<b>82</b>

## はじめに



関西光子科学研究所  
所長 田中 淳

本年報では、関西光子科学研究所（以下、関西研）において2023年度に実施された研究開発の主だった成果を紹介しています。関西研は国立研究開発法人量子科学技術研究開発機構（以下、QST）の研究開発拠点であり、けいはんな学研都市にある京都府木津地区と播磨科学公園都市にある兵庫県播磨地区の二箇所に研究サイトを持っています。特に木津地区では、レーザーの短パルス性を活かした超高速計測技術開発や世界トップレベルの高強度レーザー技術を基盤としたレーザー加速研究、またそれらのレーザー技術を用いた医療・産業等への応用研究等を実施しています。播磨地区では、大型放射光施設 SPring-8 の2本の専用ビームラインと計算機シミュレーションを活用することで、新しい放射光 X 線利用技術開発と物質材料科学の最先端研究を展開しています。

2023年度は QST として第2期中長期計画の初年度に当たりますが、様々な分野で多くの進展がみられています。超高速光技術などで量子技術開発を行う量子応用光学分野では、衝突で駆動される一般的な化学反応を、従来よりも高速に解明することを目指した衝突型液膜ジェット法を用いたサブマイクロ秒溶液混合技術の開発や量子論理ゲートに用いる分子の設計のための励起子ダイナミクスの研究、また、最先端レーザー加工に向けたシリコンのレーザー励起による損傷閾値の理論的および数値的な解析や X 線レーザーを用いたサファイア結晶へのサブナノメートル深さのパターニング、さらには EUV リソグラフィーのためのスズプラズマからの EUV 放射を計算するモデル開発が進められています。また医療への応用研究では、量子メスの入射器開発で重要なターゲット表面に付着する不純物高速除去技術の開発や医療用複合光ファイバースコープの開発などが進められています。量子生命科学分野においては、Homo-FRET 法に基づく蛍光変更法を用いた DNA 損傷クラスターの検出などの成果が得られています。

一方、高強度レーザー研究分野では、J-KAREN-P を用いたレーザー駆動重イオン加速を最適化する高密度プラズマの X 線診断手法を開発するとともに、200MeV を超える陽子の実現に向けて両面が自由表面のグラフェンターゲットを用いたレーザー加速実験などの挑戦的な研究が進められています。また、レーザー航跡場電子加速で発生する高エネルギー電子ビームの3次元電子密度分布を再構成する計算手法の開発や高強度テラヘルツ場の理解のための強力なテラヘルツ自由電子レーザーからの単一パルス抽出に成功しました。さらに、基礎科学に貢献するものとして、宇宙核時計  $^{176}\text{Lu}$  の半減期の信頼性の高い値を計測し、半減期の矛盾問題を解決しました。

播磨地区においては、誘電体材料で観察されるサイズ効果の本質に迫るためのブラッグコヒーレント回折法によるチタン酸バリウムのナノ結晶の物理的特性の解明や X 線磁気円偏光発光を用いた方向性電磁鋼板の磁区の可視化について成果が得られています。また、計算機シミュレーションを活用して、注目されている光照射による強相関電子系のダイナミクス解明のためのモット絶縁体における時間分解磁気励起の理論的研究や第一原理分子動力学法による水素ハイドレート C1' 相におけるプロトン秩序化の解析研究などが進展致しました。

関西研は、「光子」をキーワードとして我が国の量子科学技術の発展とイノベーションの創出へ貢献する研究拠点としての役割を果たすとともに地域にも世界にも開かれた研究所となれるよう、職員一同、より一層努力してまいります。皆様のご理解・ご協力を宜しくお願い申し上げます。

2024年吉日

## Preface

This annual report from Kansai Institute for Photon Science (KPSI) provides highlights of the scientific and technical research that was conducted over the FY2023. KPSI is one of the R&D bases of the National Institutes for Quantum Science and Technology (QST) and has two sites, the Kizu site in Keihanna science city in Kyoto prefecture and the Harima site in Harima Science Garden City in Hyogo prefecture. At the Kizu site, we are conducting state-of-art research such as developing new-type laser-driven radiation sources such as laser accelerated particle beams and ultrashort X-rays based upon world-leading top-class high-intensity laser technology, ultrafast measurement methodology using ultrashort pulse technology, and quantum life science which helps us to understand radiation effects and to develop new medicines. At the Harima-site, using two contract beamlines of SPring-8 and computer simulation, we are developing new technology to utilize synchrotron radiation X-rays and carrying out state-of-art research in material science.

FY2023 is the first year of the second mid- to long-term plan for QST, and much progress has been made in various research fields. In the field of quantum applied photonics, quantum technology is being developed with ultrafast laser technology and others at the Kizu site. Here several fruitful results have been presented such as the free impinging liquid-sheet jet technique as a micro-mixer for investigating general chemical reactions driven by molecular collisions faster than before, the exciton dynamics study for molecular design of quantum logic gates, the theoretical and numerical analysis of the damage threshold of the laser excitation of silicon for cutting edge laser processing, the sub-nanometer scale digging patterning of sapphire crystals using an X-ray laser, and the calculation modelling of EUV emission from tin plasma for advanced EUV lithography technology. In addition, for medical applications, advanced R&D is underway, including the development of a new method of fast cleaning of target surface contamination by induction heating for the laser-driven carbon-ion injector system of Quantum Scalpel, and the development of composite optical fiberscopes for testing and treatment. In the field of quantum life science, a new method to characterize DNA damage clusters by fluorescence anisotropy measurements based on the homo-FRET method has been developed.

In the field of high-intensity lasers and their application at the Kizu site, an x-ray diagnostic method for high-density plasmas for optimizing laser-driven heavy ion acceleration has been developed, and laser ion acceleration with large-area suspended graphene (LSG) targets have been investigated for the realization of over 200 MeV protons. In addition, a numerical study on the three-dimensional electron density distribution of high-energy electrons from laser wakefield electron acceleration has been studied. For the high-field effects in THz radiation, extraction of a single pulse from an intense THz free-electron has been demonstrated. Furthermore, as a contribution to basic science, the half-life of a long-lived radioisotope,  $^{176}\text{Lu}$ , has been measured accurately, contributing to the study of the formation and evolution of our solar system and so on.

At the Harima site, results have been obtained in the observation of buried magnetic domains by the X-ray magnetic circularly polarized emission (XMCPPE) technique and in clarifying the physical properties of barium titanate single particles in ceramics using the Bragg-CDI method to get to the essence of the size effect observed in dielectric materials. In addition, theoretical studies have been conducted in the time-resolved magnetic excitation in a photoexcited Mott insulator and in the analysis of proton disordering in the  $c1'$  phase of  $\text{H}_2$  hydrate using a first-principles molecular dynamics method.

KPSI will play a role as a research base that contributes to the development of quantum science and technology in Japan and the creation of innovation with the keyword "photon" and will be a research institute open to the community and society. We appreciate your understanding and cooperation.

Sincerely, 2024  
TANAKA Atsushi  
Director General of KPSI



# Activities of KPSI

## 関西光量子科学研究所の主な動き

関西研での各種シンポジウム・出展・アウトリーチ活動については、Appendix にまとめてあります。ここでは主なものについてご紹介いたします。

### シンポジウム・研究会の開催等

2023年4月10日～11日

#### 【光量子・量子機能創成連携ワークショップ】

国から指定された「量子技術基盤拠点」における、光技術も活用した量子技術の研究開発の一環として、高崎量子技術基盤研究所（以下、高崎研）の量子機能創製センターとの連携強化に向けたワークショップを開催しました。高崎研の材料開発技術や関西研の極短パルスレーザー発生・計測技術について情報交換を行い、関西研のレーザー・実験設備を見学し、今後の連携研究について活発な議論が成されました。



見学通路にて

2023年6月13日～14日

#### 【光・量子ビーム科学合同シンポジウム 2023 (OPTO 2023)】

大阪大学との包括協定に基づき、合同シンポジウム OPTO 2023 を開催いたしました。2022年に続き2023年も会場およびオンライン配信によるハイブリッド開催を行いました。参加者は約170名で、招待講演を含む講演10件、パワーレーザーコミュニティ会議、ポスター発表と若手ポスター賞表彰、大阪大学近藤賞受賞講演が行われました。ポスター発表は2020年以来の対面開催となり、大変盛況でした。



ポスター会場の様子

2023年7月10日～13日

#### 【第79回藤原セミナー：高強度場科学の展望 (PHFS2023)】

藤原科学財団の支援を受け、淡路夢舞台国際会議場にて第79回藤原セミナー：高強度場科学の展望 (Prospects for High-field Science, PHFS2023) を開催しました。本セミナーは2020年に開催予定のところ新型コロナウイルス感染症の影響で延期し、2023年によりやうく開催することができ、海外から22名、総勢58名の方が参加しました。会議では高強度レーザーを用いた高強度場科学を中心に、宇宙や原子核実験での高強度場、雷からの放射線など幅広い分野を網羅し、コーヒープレークはもちろん、朝食から夜の親睦会まで熱心に議論が行われました。



参加者集合写真

2023年9月29日

【令和5年度文部科学省マテリアル先端リサーチインフラ事業 JAEA&QST 合同放射光利用講習会】

マテリアル先端リサーチインフラ（ARIM）事業の新規利用者を開拓するために実験装置とその利用方法を説明する講習会を日本原子力科学研究開発機構（JAEA）と共催で播磨地区の放射光物性研究棟付属建屋「萌光館」およびオンラインでのハイブリッドで開催しました。まずはQST 綿貫センター長、JAEA 岡本ディビジョン長がそれぞれ「マテリアル先端リサーチインフラ事業の概要」について説明し、ARIM センターハブの物質・材料研究機構 松波副代表に「ARIMのDX基盤を活用したデータ駆動型研究支援」について解説していただきました。続いて石井上席研究員から「高分解能 X線吸収分光・発光分光による電子状態解析」について、大和田グループリーダーから「ナノ結晶非破壊3次元イメージング技術」について、JAEAからの2件の放射光計測技術について説明が行われました。現地、オンライン合わせて43名（講師、スタッフ含む）もの参加があり、盛況でした。

2024年3月14日

【兵庫県立大学高度産業科学技術研究所ニューズバルシンポジウム2024】

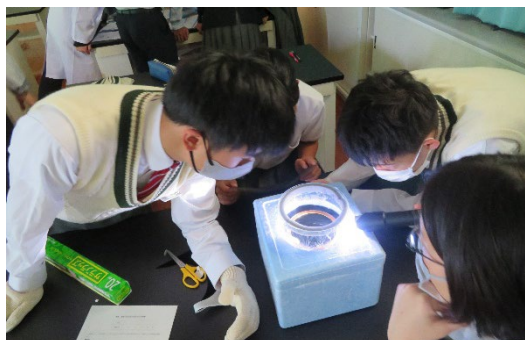
マテリアル先端リサーチインフラ（ARIM）事業の広報と新規利用者開拓のために、アクリエひめじで開催された兵庫県立大学高度産業科学技術研究所ニューズバルシンポジウムに協賛して、QST-ARIM 事業についてポスター発表しました。ニューズバルや兵庫県立大学工学部の先生方および企業からの参加者等にQST-ARIMの登録装置や制度の利点を説明しました。

## 出展・イベント

2023年10月17日

【令和5年度播磨高原東中学校出前授業】

SPring-8 近郊に所在する播磨高原東中学校の3年生を対象に、「核エネルギーと放射線」をテーマに、放射線に関する講義と、自然放射線の観察として霧箱実験を実施しました。実験を通して、目に見えないために普段は意識の外にある放射線が意外に身近に存在することを実感したことにより、放射線に対する興味関心が高まったようで、授業後に熱意ある感想を頂きました。



実験の様子

2023年11月11日

【関西光量子科学研究所（木津地区） 施設公開】

2023年度は感染症対策の制限解除後初の開催となり、木津川アート2023イベントとの共催の影響もあって、過去最多の1,402名の方々にご来場いただきました。従前の工作教室やセミナー、実験施設や装置の見学に加え、大阪科学技術館や国立研究開発法人情報通信研究機構等、たくさんの外部団体の方にご出展をいただきました。4年ぶりに木津南中学校吹奏楽部の演奏会も開催し、大盛況の中イベントを終えることができました。



施設公開告知チラシ



大人気のふおとん君



量子生命研の出張出展も好評でした(左)、普段は見られない装置見学@実験棟見学廊下(右)

## プレスリリース（研究成果）

1. ～人の手に頼らないロボット点検技術のイノベーション～  
道路橋のレーザー打音検査によるリモート検査の実証実験（2023年5月30日）  
<https://www.qst.go.jp/site/press/20230530-2.html>
  
2. 超高压合成、添加剤が選択的物質合成の決め手に  
—電池材料等への応用に期待—（2023年7月25日）  
<https://www.qst.go.jp/site/press/20230725.html>  
論文タイトル：Selective Synthesis of Perovskite Oxyhydrides Using a High-Pressure Flux Method
  
3. がん治療用新型イオン入射装置の原型機が完成  
～重粒子加速器の小型化をレーザー技術で目指す～（2023年8月30日）  
<https://www.qst.go.jp/site/press/20230830.html>
  
4. 宇宙核時計ルテシウム 176 の半減期問題を解決（2023年11月3日）  
<https://www.qst.go.jp/site/press/20231103.html>  
論文タイトル：Half-life of the nuclear cosmochronometer  $^{176}\text{Lu}$  measured with a windowless  $4\pi$  solid angle scintillation detector

5. 道路政策の質の向上に資する技術研究開発（令和 3 年度採択）において、優秀技術開発賞を受賞しました（2023 年 11 月 15 日）

<https://www.qst.go.jp/site/press/20231115.html>

受賞タイトル：レーザー打音検査装置を用いた橋梁・トンネル等の道路構造物のうき・剥離の定量的データ化による診断技術の技術研究開発

6. 電子にはたらく特殊な力をマイクロメートルの高解像度で可視化  
—「量子マテリアル」のデバイス評価に新展開—（2023 年 12 月 21 日）

<https://www.qst.go.jp/site/press/20231221.html>

論文タイトル：Quantitative measure of correlation strength among intertwined many-body interactions

7. 電子・スピンの運動を可視化する走査型顕微鏡の開発  
—マイクロメートル領域のスピン流を精密に測定—（2024 年 1 月 12 日）

<https://www.qst.go.jp/site/press/20240112.html>

論文タイトル：Laser-based angle-resolved photoemission spectroscopy with micrometer spatial resolution and detection of three-dimensional spin vector

8. がん組織近くで使える高エネルギー電子線をレーザーで発生  
—内視鏡型電子線発生装置を用いた放射線がん治療の実現へ—（2024 年 3 月 29 日）

<https://www.qst.go.jp/site/press/20240329.html>

論文タイトル：Experimental realization of near-critical-density laser wakefield acceleration: Efficient pointing 100-keV-class electron beam generation by microcapillary targets



# User Facilities

## 主要な施設・装置

### 木津地区

#### ○J-KAREN-P レーザー装置

##### 【装置概要】

世界トップクラスの極短パルス超高強度レーザーです。最大 30 J のレーザーエネルギーを 30 フェムト秒（1 フェムトは 1000 兆分の 1）の時間に閉じ込めることにより 1000 兆ワットの超高出力を実現します。システムアップグレードによりプラズマミラー使用時の時間コントラスト比が改修前と比べて向上しました。



##### 【供給装置性能】

- ・ 中心波長：810 nm
- ・ 繰り返し：シングルショット～0.1 Hz
- ・ ターゲット照射エネルギー：～10 J/pulse
- ・ パルス幅：30～50 フェムト秒
- ・ 集光強度： $10^{20}\sim 10^{22}$  W/cm<sup>2</sup>
- ・ 時間コントラスト比：<math><10^{-11}</math>（プラズマミラー不使用時）  
<math><10^{-14}</math>（シングルプラズマミラー使用時）  
<math><10^{-17}</math>（ダブルプラズマミラーへアップグレード後の予定）

##### 【主要な研究課題】

超高強度レーザーの技術開発、イオンや電子の加速技術開発、高輝度 X 線等の量子ビーム源開発

#### ○QUADRA-T レーザーシステム

##### 【装置概要】

高平均出力ピコ秒パルスレーザーです。システムアップグレードにより照射エネルギー、繰り返しを向上し、1 秒間に 5000 発のレーザーパルスが繰り返せるようになりました。

##### 【装置性能】

- ・ 照射エネルギー：20 mJ/pulse
- ・ 波長：1030 nm
- ・ 繰り返し：5 kHz
- ・ パルス幅：約 1 ピコ秒



##### 【主要な研究課題】

高繰り返し高出力レーザー（パラメトリック増幅器等）の開発、高強度テラヘルツ光源の開発

#### ○その他

その他、kHz チタンサファイアレーザー、X 線回折装置及び成膜装置を共用に供しています。

## 播磨地区

播磨地区では大型放射光施設 SPring-8 に 2 本の QST 専用ビームラインを設置しているほか、日本原子力研究開発機構 (JAEA) の専用ビームラインにも複数の放射光専用実験装置を常設しています。一方で、QST 専用ビームラインにも、JAEA の専用実験装置が常設されています。

### ○BL11XU (QST 極限量子ダイナミクス I ビームライン)

#### 【装置概要】

SPring-8 標準の真空封止アンジュレータを光源とし、マルチ結晶交換システムを装備することで、広範囲のエネルギー領域の高輝度放射光 X 線を高効率に利用できるビームラインです。

#### 【装置性能】

- ・光源：真空封止アンジュレータ
- ・エネルギー領域：6~70 keV
- ・分光結晶：Si(111)、Si(311)
- ・実験装置：放射光メスバウアー分光装置、共鳴非弾性 X 線散乱装置、及び表面 X 線回折計

#### 1. 放射光メスバウアー分光装置

$^{57}\text{Fe}$ 、 $^{61}\text{Ni}$  等のメスバウアー核種を対象とした放射光メスバウアー分光が可能で、物質の電子、磁気状態から格子振動状態に関する情報などを得ることができます。さらに、斜入射法や同位体置換試料を利用することで、金属薄膜の表面部を原子層単位で測定することも可能です。



#### 2. 共鳴非弾性 X 線散乱装置

入射 X 線、散乱 (発光) X 線の双方のエネルギーを 0.1 eV 程度のエネルギーで分光実験が可能な装置です。4 軸回折計配置で共鳴非弾性 X 線散乱により電子励起の運動量依存性が測定できるほか、高エネルギー分解能 X 線吸収分光、X 線発光分光の実験も可能です。試料温度は 10 K から 800 K まで可変です。



#### 3. 表面 X 線回折計

分子線エピタキシー (MBE) チェンバーを搭載した表面構造解析用 X 線回折計です。半導体量子ドットや半導体多層膜などの成長過程を X 線回折によりその場観察・リアルタイム観察が可能です。2 台の MBE を交換し、GaAs、InAs などのヒ素化合物成長と RF-MBE による GaN、InN などの窒化物半導体成長を行うことができます。



#### 【主要な研究課題】

金属薄膜の原子層単位での磁性探査、遷移金属化合物における電荷・スピン・軌道励起の観測、触媒や電池電極材料のオペランド電子状態解析、半導体量子ドットや半導体多層膜の成長過程のリアルタイム解析

## ○BL14B1 (QST 極限量子ダイナミクスⅡビームライン)

### 【装置概要】

偏向電磁石を光源とすることで、連続スペクトルを持つ白色 X 線や高エネルギーの単色 X 線が利用可能なビームラインです。全反射ミラーや分光結晶の曲げ機構によって、試料位置への集光が可能となっています。

### 【装置性能】

- ・光源：偏向電磁石
- ・エネルギー領域：白色 X 線 (5~150 keV)、単色 X 線 (5~90 keV)
- ・実験装置：高温高压プレス装置、汎用四軸 X 線回折計及び分散型 XAFS 測定装置 (JAEA)

#### 1. 高温高压プレス装置

10 GPa (13 万気圧)、2300 K 程度までの圧力・温度状態下の試料を、白色 X 線を用いたエネルギー分散型 X 線回折法やラジオグラフィ法、単色 X 線を用いた XAFS (X 線吸収微細構造) 法や角度分散型 X 線回折法等によって調べることができます。

【主要な研究課題】 高压下での金属水素化物形成過程のその場観察



#### 2. 汎用四軸 X 線回折計

令和 2 年 3 月に RI 実験棟から移設。X 線照射位置を可視化するためのレーザーを整備しており、がん研究等のための単色 X 線を利用した照射実験に使用できます。高エネルギー単色 X 線を利用した回折法により、大型構造材料中の応力・ひずみ、結晶方位分布計測の測定も可能です。

【主要な研究課題】 応力・ひずみ、結晶方位の三次元分布測定、及び照射実験等



## ○BL22XU (JAEA 専用ビームライン) における放射光専用実験装置

#### 1. 高速 2 体分布関数計測装置 (旧ダイヤモンドアンビルセル回折計)

最高 70 keV の高エネルギー X 線と大型二次元 X 線検出器の利用により最大  $Q = 27 \text{ \AA}^{-1}$  までの X 線全散乱プロファイルが迅速に得られ、約 100  $\text{\AA}$  までの距離相関の原子二体分布関数が導出できます。専用アタッチメントにより、室温、1 MPa 未満の水素と窒素ガス雰囲気でのその場観察ができます。試料-検出器間距離が可変のため高角データから高分解能データまで取得が可能であり、ダイヤモンドアンビルセルを用いた高圧力下 X 線回折測定にも適用可能です。



#### 2. コヒーレント X 線回折イメージング装置 (旧大型 X 線回折計)

X 線領域のブラッグ反射を利用したコヒーレント X 線回折イメージングが実施できる水平振りの大型 X 線回折計です。粒径 100 nm 以下のナノ結晶ひと粒のサイズや形状、内部構造 (応力、ドメイン等) を含む 3 次元イメージングが可能です。



### 【主要な研究課題】

水素貯蔵合金、負の熱膨張材料、100~500 nm 級チタン酸バリウムナノ結晶粒子一粒の 3 次元可視化、40 nm 級パラジウムナノ結晶粒子一粒の 3 次元可視化

## 施設の稼働実績と利用状況

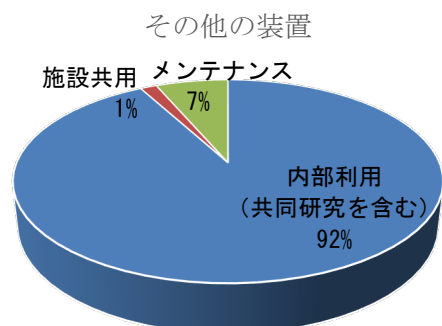
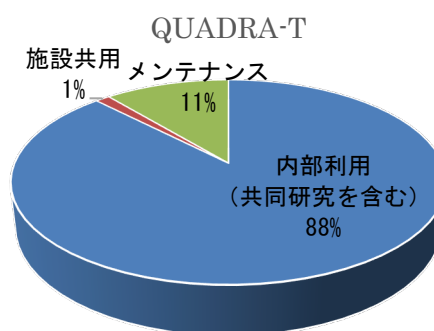
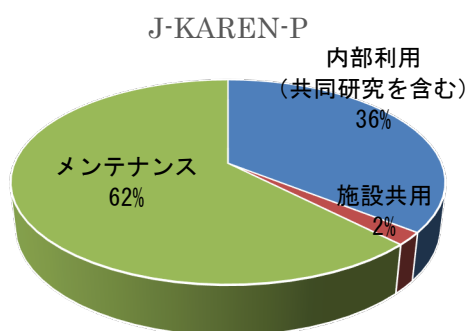
### 木津地区

2023年度の運転時間はJ-KAREN-Pは1660時間、QUADRA-Tは1023時間、その他装置は合計678時間でした。

#### 実施課題件数

装置名称	独自研究	受託研究	共同研究	施設共用
J-KAREN-P レーザー装置	2	0	0	2
QUADRA-T レーザーシステム	1	2	0	1
kHz チタンサファイアレーザー	4	1	1	1
X線回折装置	0	0	0	0

#### 稼働時間内訳



## 播磨地区

2023年度のSPring-8蓄積リングの運転時間は5112時間で、放射光利用時間はそのうちの4464時間でした。QST、JAEAとも専用ビームラインでは10%程度の調整時間を除き、放射光利用時間で独自研究や受託研究、外部利用者への施設共用と研究支援を行っています。

### 実施課題件数

ビームライン	独自研究	受託研究	共同研究	施設共用
BL11XU	9	0	3	22
BL14B1	22	0	5	13
BL22XU	6	0	8	15

### 利用日数

ビームライン	独自研究	受託研究	共同研究	施設共用
BL11XU	74(93)	0	15(18)	80(103)
BL14B1	74(114)	0	18(25)	37(49)
BL22XU	25(38)	0	24(39)	28(43)

\*件数、日数ともにQSTの利用課題のみ

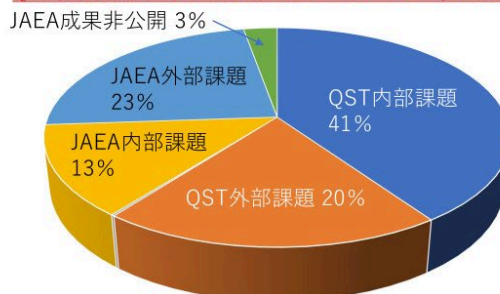
\*日数は3シフトを1日とした。括弧内はマテリアル先端リサーチインフラ事業での算定法による。

### 稼働時間内訳

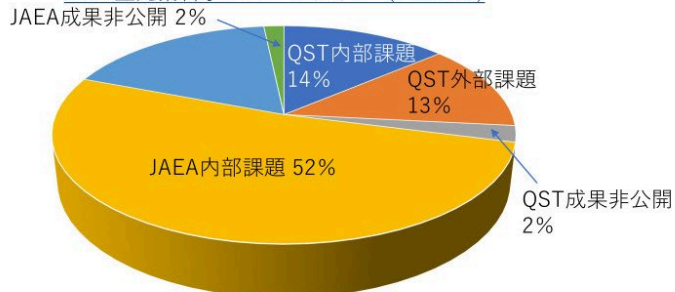
QST極限量子ダイナミクスIビームライン (BL11XU)



QST極限量子ダイナミクスIIビームライン (BL14B1)



JAEA重元素科学Iビームライン (BL22XU)



# Research Highlights

# Quantum Applied Photonics Activities

KONDO Kiminori

Department of Quantum Applied Photonics



From the beginning of FY2023, a new medium to long-term plan of QST has been initiated, wherein KPSI is required to study optics research related to quantum technology. The Ministry of Education, Culture, Sports, Science, and Technology has defined quantum computing, information, and sensing technologies as “quantum technology.” Although a laser is an optical maser, which was invented by applying quantum mechanics in 1954, it is not included under “quantum technology.” Moreover, KPSI is required to research the high field of basic science along with social contributions. Thus, the Department of Quantum Applied Optics has been established for research focusing on social contributions. While the science and technology related to advanced lasers are the foundation for research conducted in our department, high peak power, high repetition rate, high stability, and ultrafast laser system are more important as we develop these technologies in-house and apply them to various projects, as in the past. The research and development activities of our department have been shown in Fig. 1. Cutting-edge laser technology and the world’s leading simulation code support the department’s activities.

by DrYamakawa, Dr. Itakura, Dr. Ishino, and I, respectively. A project review was held at the end of last year. Further, various activities of the department have been described.

The observable shortest pulse duration in the world is realized with a soft X-ray pulse in the attosecond region. Currently, KPSI focuses on attosecond science by adopting the technology awarded the Nobel Prize in Physics last year. Although no detection has been demonstrated at KPSI and related articles have not been included in this annual report, the development of a pump laser system for generating attosecond soft X-rays, involving high-order harmonic generation (HHG) from neutral atoms and/or molecules, is near completion. For shorter wavelength HHG, a long wavelength pump laser is required. Moreover, to recover the decrease in HHG yield with a long wavelength pump laser, the order of high average power pump source should be prepared. Currently, the QUADRA-T laser system is under improvement based on a thin-disk Yb: YAG power amplifier. Thus, an eventual and clear application of stable, bright, usable attosecond HHG is expected shortly.

In our department, groups have been replaced by a project system from the beginning of FY2023, where a project leader proposes a project and adopted projects proceed. Four projects have been initiated for the fiscal year including the medical laser application, ultrafast electronic dynamics, x-ray ultrafine structure processing, and laser-driven ion accelerator projects led

As a social contribution, the ultrafast switching technology of spin-photonics is important for high-speed digital clock technology. The project led by Dr. Itakura has initiated collaboration with Dr. Sakai’s group at Takasaki Institute for Advanced Quantum Science, QST, to study spin-photonics in two-dimensional materials. The preparation for their

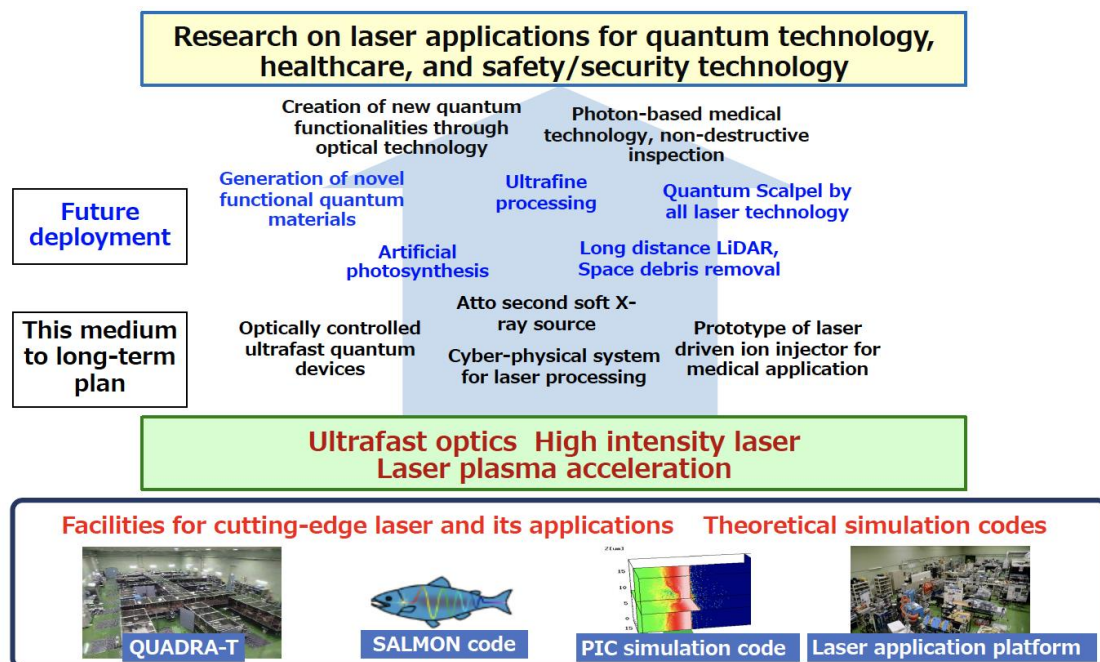


Fig.1 Research and development activities of the Department of Quantum Applied Photonics.

collaboration started from this fiscal year. Additionally, the project led by Dr. Ishino is in collaboration with Takasaki Institute to focus on spintronics and diamond nitrogen-vacancy (NV) center generation with high-power laser. NV center technology is a quantum sensing technology that can be used as the qubit in quantum computing and information technology in the future. Owing to its relation with quantum life science technology, the project led by Dr. Itakura is in collaboration with the Adachi team of the Institute for Quantum Life Science, QST, to study giant molecule coherence. Ultrafast two-dimensional electron spectroscopy has been used to detect ultrafast coherence dynamics in proteins. The aforementioned collaborations have been held for initiating quantum technology research at KPSI.

Dr. Endo from the ultrafast electronic dynamics project reports rapid solution mixing in a micro-mixer with free impinging jets, which is a new target technology that enables two liquid materials to be mixed with a thin enough thickness for laser interaction. Dr. Otobe from the ultrafast electronic dynamics project reports theoretical and numerical analyses of the damage threshold of silicon. Dr. Otobe is one of the key developers of the SALMON code, which is the leader code that treats ultrafast interaction between laser light and material. Furthermore, he plays an important role in the Q-LEAP project to develop a cyber-physical system for laser processing based on theory. Laser processing is one of the most important applications of high-power lasers, and its social contribution is expected to be large, especially in semiconductor technology. Recently, cutting-edge integration technology has emerged as the most important semiconductor technology that includes laser processing. A fine structure production with coherent X-ray is also important in laser processing. As the leader of the X-ray ultrafine structure processing project, Dr. Ishino reports sub-nanometer scale depth patterning on sapphire crystal. The present semiconductor integration technology is based on EUV lithography. Although the technology is utilized in the real fabrication of advanced semiconductors, improvements to efficiency can be implemented. However, the estimation of efficient EUV generation by theoretical analysis is important. Dr. Sasaki from the X-ray ultrafine structure processing project reports the effect of multiply excited states on EUV emission from yttrium-like tin.

One of the most important high-field sciences continued at the KPSI Kizu site is laser-plasma acceleration. To use the featured physical phenomenon, a compact carbon ion injector for Quantum Scalpel (a new-generation heavy-ion cancer therapy machine) is being developed since the establishment of QST eight years ago. Quantum Scalpel is one of the main projects of QST. The JST-MIRAI research and development program (large-scale type) started in November 2017, intending to demonstrate the proof of concept (POC) for a laser-plasma accelerator. In addition to an ion accelerator, a laser plasma electron accelerator is also under development at KPSI, under the MIRAI program. The POC of the laser-driven heavy-ion injector is expected to be demonstrated by the end of FY2026. In FY2020, the first-stage gate was successfully passed. In this fiscal year, a second-stage gate exam was held for JST-MIRAI. We built and operated a prototype machine of the carbon ion injector in collaboration with the Hitachi Zosen and Sumitomo Heavy Industry. Dr. Kojima from the laser-driven ion accelerator project reports the development of important target technologies.

The most important application of high-power laser science and technology involves industrialization. A non-destructive tunnel-inspection technology is under development within the X-ray ultrafine structure processing project during the second term SIP program and in Sin Dohro Gijutsu Kaigi at MLIT. The technology is being tested for applications to commercial technology at the venture company Photon-Labo. Non-destructive tunnel inspection is possible using laser-hammering technology, which is expected to find applications involving the inspection of tunnels and various concrete structures. From FY2023, paid joint research between QST and Photon-Labe has been established. Although no special article is included in this annual report, the activity is one of the most important research projects in this department.

Moreover, Dr. Yonetani reports an exciton dynamics study for the molecular design of quantum logic gates, which is related to quantum computation technology. Dr. Oka reports the medical applications of composite optical fiber scope, which is important for advanced medical technology.

# Induction heating for the desorption of contamination for laser-driven carbon-ion acceleration

KOJIMA Sadaoki



Laser Driven Ion Accelerator Project, Department of Quantum Applied Photonics

The National Institutes for Quantum Science and Technology (QST), Japan, has progressed toward developing a compact accelerator called “Quantum Scalpel” for carbon-ion radiotherapy to overcome existing issues.<sup>1</sup> The Quantum Scalpel comprises a laser-driven injector (acceleration of 4 MeV/u), superconducting synchrotron (diameter of 8 m), and superconducting gantry. The required ion-beam parameters of the laser-driven ion injector are set by referencing the current ion injector of HIMAC using radiofrequency acceleration. The laser-driven ion injector is required to inject  $>10^9$  carbon ions ( $C^{4+}$  or  $C^{6+}$ ) with quasi-monochromatic energy (10% bandwidth) of 4 MeV per nucleon within 2 s. To suppress beam divergence caused by space-charge effects during acceleration in the synchrotron, the maximum number of particles that can be injected in a single acceleration phase is limited to  $\approx 10^8$ . Therefore,  $10^8$  ions are repeatedly injected at 10 Hz until the required number of particles is injected into the synchrotron. Additionally, pre-accelerated ions are injected into the synchrotron after compressing them to 1 % bandwidth using the phase rotation cavity. The synchrotron accelerates the carbon ions to 430 MeV/u, which is sufficient for heavy ion radiotherapy. The gantry enables the treatment of tumors located deep inside the body from any direction.<sup>2</sup>

A laser-driven carbon-ion injector requires three systems (laser, target supply, and surface contamination cleaner) that can operate at repetition rates of over 10 Hz. With the recent advent of diode-pumped solid-state lasers,<sup>3</sup> the irradiation of 10 J-class laser pulses at several hertz is possible, while a high-repetition-rate laser irradiation above 10 Hz can be achieved.

However, the performance of surface contaminant cleaners at a high repetition rate is insufficient for the immediate cleaning of target surface contamination supplies. In the target normal sheath acceleration mechanism, protons are selectively accelerated over other heavier ion species owing to their largest charge-to-mass ratio. The origin of such protons is known to be water vapor and hydrocarbons that adsorb into the target surface during target manufacturing or after installation in the vacuum chamber. The surface contamination layer is  $\sim 1$  nm thick<sup>4,5</sup> and comprises  $CH_2$  (60 %) and  $H_2O$  (12 %). The contamination molecules are chemisorbed on the surface and require  $\sim 100$  kJ/mol of energy for desorption. Desorption of such molecules by thermal motion requires heating above 200 °C.<sup>6</sup>

In this paper, a new method for cleaning surface contamination by induction heating is reported. The developed induction heater heats a 5  $\mu m$  thick nickel tape to over 400 °C in 100 ms and is expected to scale to carbon-ion acceleration at 10 Hz shortly. Three concentric-ly-turned coils (pancake shape) on a copper pipe are designed. Cooling water flows inside the pipe, while AC flows through the conductor portion. The coils are placed 4 mm apart parallel to a tape target. The outer shape of the coil is 25 mm, larger than the 20 mm width of the nickel tape, such that both ends of the coil protrude from the tape.

Figure 1(a) shows the temperature distribution of the nickel tape, experimentally observed by infrared thermography, when heated at an AC power of 0.6 kW. The white dotted lines represent

both ends of the 20-mm-wide tape, whereas the black dotted lines indicate the simulated 350 °C isotherm. The temperature distribution observed experimentally accurately reproduces the distribution obtained from the simulation, including the asymmetry of hot spots due to coil asymmetry. The red line in Fig. 1(b) depicts the time variation of temperature of the left hot spot (a small white square region in Fig. 1(a)) during heating.

A partial volume of nickel tape ( $\sim 5 \times 5 \times 5$   $\mu m$ ) was heated to 400 °C in  $\sim 100$  ms. Utilizing data on the specific heat of nickel and the volume of the heating area, the heating areal power density due to induction heating was estimated as  $\sim 2$  W/cm<sup>2</sup>. When the target was heated to  $\sim 400$  °C,  $\sim 2$  W/cm<sup>2</sup> of energy was lost by radiation. However, radiation loss and heat generation were balanced, causing the temperature rise to saturate. The target temperature at laser irradiation varied with the time interval between heating and laser irradiation. The blue line in Fig. 1(c) depicts the time variation of hot spot temperature after leaving the heating coil. When the vacuum pressure was 0.05 Pa, the vacuum gap limited thermal conduction along the perpendicular direction to the nickel surface. The nickel tape heated to  $\sim 400$  °C rapidly cooled to 180 °C within 1 s (radiation cooling); then, it cooled down slowly to below 100 °C for  $\sim 12$  s (thermal conduction).

For this study, laser-driven ion acceleration was employed as a time-resolved analytical technique for surface contamination, and the temperature dependence of desorption and re-adsorption of adsorbate molecules was evaluated. A linearly polarized (p-polarized on target), 40 fs laser pulse (full-width half maximum, FWHM) with a central wavelength of 795 nm was focused on a 5  $\mu m$  thick nickel foil at a 45° incidence angle using an F/2.7 off-axis parabolic mirror. Then, 23 % of 389 mJ (total energy) was focused into a focal spot of diameter 5  $\mu m$  (FWHM), and the average laser intensity in the spot was measured as  $6 \pm 1 \times 10^{18}$  W/cm<sup>2</sup>.

The top spool was pre-wound with nickel tape, and the motor-driven rubber roller (comprising heat-resistant silicon that can be used for 10,000 h or more at 200 °C) drew the tape target from the top spool. The heating coil was placed 10 cm along the tape passing above the laser irradiation point. A series of experiments were performed under six conditions, as depicted in Fig. 2: one case of no heating condition and five cases of heating conditions with varying target temperatures of 50, 80, 110, 130, and 150 °C at laser irradiation. The target temperature at the laser irradiation point was varied with the time interval between heating and laser irradiation. Accelerated ion species were analyzed using a Thomson parabola ion spectrometer.<sup>7</sup> A phosphor screen assisted in detecting 30 ions, the scintillation light was transported using a lens, and a cooled charged-coupled device camera was used to record.

Under the no heating condition, the strongest trace agrees with that of the theoretical trace of proton ( $Z/A = 1.00$ ), as shown in Fig. 2(a). The charge-to-mass ratios,  $Z/A$ , of the weaker four traces observed in Fig. 2(a) are estimated as  $\sim 0.083$ , 0.17, 0.25, and 0.33. These ratios are consistent with the theoretical charge-

to-mass ratios of  $C^+$ ,  $C^{2+}$ ,  $C^{3+}$ , and  $C^{4+}$ , respectively. Under the five heating conditions of 50, 80, 110, 130, and 150 °C, ion species with different trends are accelerated. When the target temperature is cooled to 50 and 80 °C, the proton signal is dominant, similar to that in the non-heated case, and the maximum charge state of carbon ion is 4 (Fig. 2(b) and (c)). The obtained results indicate that once desorbed by heating, hydrogen is reabsorbed by the surface as it cools below 80 °C. In the case of 110 and 130 °C (Fig. 2(d) and (e)), the proton signal is still dominantly observed, but the maximum charge state of carbon ions increases to 5, and the higher signal energy part of carbon ions increases. Nickel ions originating from the target bulk are also accelerated. When the laser is promptly irradiated and kept at 150 °C (Fig. 2(f)), the proton signal reduces, and the  $C^{4+}$  and  $C^{5+}$  ion signals are dominant.

An analysis code is used to precisely link the particle position on the detector with its kinetic energy and convert the recorded parabolic traces to ion spectra. On the ion spectra for no heating conditions (Fig. 2(a)), the maximum observed energies of protons and carbons are 1.0 MeV ( $H^+$ ), 0.9 MeV ( $C^+$ ), 1.3 MeV ( $C^{2+}$ ), 2.05 MeV ( $C^{3+}$ ), and 2.5 MeV ( $C^{4+}$ ).

On the ion spectra for heating conditions at 150 °C (Fig. 2(f)), the maximum observed energies of protons and carbons are 1.0 MeV ( $H^+$ ), 3.25 MeV ( $C^{3+}$ ), 5.2 MeV ( $C^{4+}$ ), and 6.52 MeV ( $C^{5+}$ ). Regardless of the difference in conditions with no heating and heating, the maximum proton energy remains constant at 1 MeV. However, the number of protons in the low-energy region (< 0.5 MeV) decreases by two orders of magnitude. Moreover, in the energy spectrum of carbon ions, the maximum charge state of the accelerated carbon ions increases from 4 to 5, with the maximum energy increasing to 6.5 MeV. The obtained results indicate that heating causes the desorption of contamination hydrogens and reduces contamination layer coverage such that the sheath field for TNSA can efficiently accelerate the carbon ions.

## Acknowledgments

This work was supported by the Japanese Ministry of Education, Culture, Sports, Science and Technology (MEXT) through the JST-Mirai Program (no. JPMJMI17A1) and Grants-in-Aid, KAKENHI (Grant No. 21J22132 and No. 22K14021).

## References

1. N. Kanematsu, T. Furukawa, et al., *Radiat. Phys. Chem.* **162**, 90 (2019).
2. Y. Iwata, T. Shirai, et al., *Nucl. Instruments Methods Phys. Res. Sect. A: Accel. Spectrometers, Detect. Assoc. Equip.* **1053**, 168312 (2023).
3. R. Lera, P. Bellido, et al., *Appl. Phys. B* **125**, 4 (2019).
4. Z. Léczi, J. Budai, A. Andreev, and S. Ter-Avetisyan, *Phys. Plasmas* **27**, 013105 (2020).
5. M. Allen, P.K. Patel, A. Mackinnon, D. Price, S. Wilks, and E. Morse, *Phys. Rev. Lett.* **93**, 265004 (2004).
6. K. Fukutani, *J. Vac. Soc. Japan* **56**, 204 (2013).
7. S. Kojima, S. Inoue, T.H. Dinh, N. Hasegawa, M. Mori, H. Sakaki, Y. Yamamoto, T. Sasaki, K. Shiokawa, K. Kondo, T. Yamanaka, M. Hashida, S. Sakabe, M. Nishikino, and K. Kondo, *Rev. Sci. Instrum.* **91**, 053305 (2020).

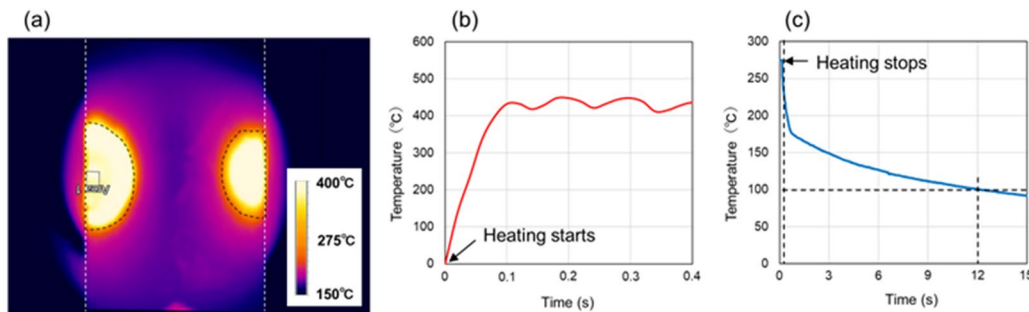


FIG. 1. (a) Temperature distribution of the nickel tape observed by infrared thermography when heated at an AC power of 0.6 kW. (b) Time variation of the temperature of the hot spot during heating. (c) Time variation of the hot spot temperature after leaving the heating coil.

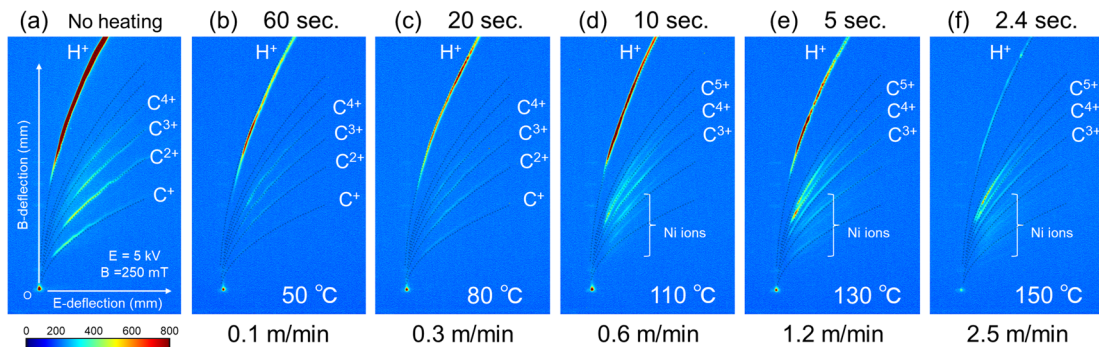


FIG. 2. Parabolic trace of TPS is observed under six experimental conditions: no heating condition (a) and five cases of heating conditions of (b) 50, (c) 80, (d) 110, (e) 130, and (f) 150 °C.

# Exciton dynamics study for molecular design of quantum logic gates



YONETANI Yoshiteru

X-ray Ultrafine Structure Processing Project, Department of Quantum Applied Photonics

Exciton transfer has been recognized as a significant process in various molecular and quantum phenomena. Recent studies have shown that exciton flow is well regulated in a photosynthetic biological system, revealing the mechanism of efficient light-energy harvesting. Such fundamental knowledge of exciton transfer not only enhances understanding but also advances the wide applicational range of molecular technologies including fluorescence imaging, engineered photosynthesis, and solar-light batteries.

An exciton-based molecular device that works as a logic gate is one of the potential applications. Logic gate circuits with precise control of exciton flow can enable molecular-scale computation, particularly at a low energy cost. In principle, such logic gate operation can be implemented even in a quantum regime if the quantum coherent states can be maintained for a long duration, promoting dramatic improvements in high-speed computing technology. Nonetheless, the realization of exciton-based molecular quantum computing is still unclear. Currently, the development of quantum computing is majorly based on other architectures including nuclear spin, superconductor, quantum dot, trapped ion, and optics technology [1].

Recently, Castellanos *et al.* [2] theoretically investigated the possibility of exciton-based molecular quantum computing. They constructed model Hamiltonians for quantum logic gates (such as NOT, Hadamard,  $\pi/8$ , and CNOT) and performed quantum dynamics calculations for exciton flow. A pair of cyanine dyes embedded into DNA was considered as a test case, where exciton switching between the two cyanine dyes served as a logic gate operation. The result showed that fidelity was not enough to conduct correct logic gate operation, mainly due to noise from the molecular environment. Thus, quantum computing with such a molecular system is far from realization. Nonetheless, such a theoretical investigation can serve as an important step for future challenges in quantum computing.

In this study [3], quantum dynamic calculations are performed using logic gate Hamiltonians, NOT and Hadamard, to gain a deeper understanding of the feasibility of exciton-based molecular quantum computing. The semiclassical path integral method originally proposed by Miller and coworkers [4] is employed. According to the scheme, not only exciton dynamics but environmental effects can be naturally incorporated into the quantum regime; vibrational motions of surrounding molecules including solvent or molecular scaffold are described as a set of harmonic oscillators. In this case, an environmental feature is mainly characterized by temperature ( $T$ ) and reorganization energy ( $\lambda$ ). Thus, the calculations performed in this study provide further information about the relationship between the exciton logic-gate system and environmental effects. Quantum dynamic calculations are performed over a wide range of parameters, which reveal molecular and electronic conditions required for realizing the exciton-based quantum logic gates. The results suggest that fast exciton transfer and a large excitonic coupling are required to avoid environmental noise during logic gate operation.

The methods adopted for calculations are shown below. Operations of the quantum logic gates (NOT and Hadamard) are given by unitary operators as

$$\begin{aligned} \hat{U}_{NOT} &= \begin{bmatrix} 0 & 1 \\ 1 & 0 \end{bmatrix} \\ \hat{U}_{Had} &= \frac{1}{\sqrt{2}} \begin{bmatrix} 1 & 1 \\ 1 & -1 \end{bmatrix} \end{aligned} \quad (1)$$

Assuming the input state as  $|1\rangle = [1 \ 0]^t$ , the NOT gate transforms the input state into  $|2\rangle = [0 \ 1]^t$ . On the other hand, Hadamard gate transforms the input state into  $\frac{1}{\sqrt{2}}(|1\rangle + |2\rangle) = \left[\frac{1}{\sqrt{2}} \ \frac{1}{\sqrt{2}}\right]^t$ . The corresponding Hamiltonians can be derived from the relation  $\hat{H} = \frac{i\hbar}{\tau} \ln \hat{U}$ , such that

$$\begin{aligned} \hat{H}_{NOT} &= \frac{\pi\hbar}{2\tau} \begin{bmatrix} -1 & 1 \\ 1 & -1 \end{bmatrix} \\ \hat{H}_{Had} &= \frac{\pi\hbar}{2\tau} \begin{bmatrix} 1/\sqrt{2} - 1 & 1/\sqrt{2} \\ 1/\sqrt{2} & -1/\sqrt{2} - 1 \end{bmatrix} \end{aligned} \quad (2)$$

With the Hamiltonians, the logic gate transformation realizes at time  $t = \tau$ , such that the state is postulated to be analyzed at  $t = \tau$ .

According to Castellanos *et al.* [2], the logic gate Hamiltonians of this study are constructed using the framework of the Frenkel exciton model; both NOT and Hadamard require Hamiltonian with two excitation sites, *site 1* and *site 2*, such that

$$\hat{H}_s = \begin{bmatrix} \varepsilon_1 & J_{12} \\ J_{21} & \varepsilon_2 \end{bmatrix} \quad (3)$$

where  $\varepsilon_i$  ( $i = 1$  and  $2$ ) denotes the energy level of each site and  $J_{ij}$  represents excitonic coupling between the two sites. With the aforementioned framework,  $|1\rangle = [1 \ 0]^t$  shows the state where *site 1* and *site 2* are in the excited and ground states, respectively. Whereas  $|2\rangle = [0 \ 1]^t$  shows the opposite situation. With the framework of  $\hat{H}_s$ , the logic gate operations expressed by Eq. (2) are implemented. To construct  $\hat{H}_{NOT}$ , the conditions required include

$$\varepsilon_1 = \varepsilon_2$$

and

$$J_{12} = J_{21} \quad (4)$$

Herein, the readout time  $\tau$  is given by  $\pi\hbar/2J_{12}$ . Two identical chromophores with the same energy level are required for the construction of NOT gate, as expressed by Eq. (4). Similarly, to construct the Hadamard gate  $\hat{H}_{Had}$ , the conditions required include

$$J_{12} = J_{21}$$

and

$$\varepsilon_1 - \varepsilon_2 = 2J_{12} \quad (5)$$

Herein,  $\tau = \pi\hbar/2\sqrt{2}J_{12}$ . Additionally, a bath part  $\hat{H}_B$  is introduced for examining the effect of environmental noise. Thus, the total Hamiltonian is given by

$$\hat{H} = \hat{H}_s + \hat{H}_B. \quad (6)$$

where  $\hat{H}_B$  represents the vibrational motions of surrounding molecules described by a set of harmonic oscillators.

The results of the Hadamard gate with the excitonic coupling  $J = 1000 \text{ cm}^{-1}$  are shown in Fig. 1; where Figs. 1(a) and (b) show the effect of  $T$  and  $\lambda$ , respectively. The Hadamard gate transforms the starting state  $\rho_{11} = 1$  and  $\rho_{22} = 0$  into  $\rho_{11} = \rho_{22} = 0.5$  at  $t = \tau$ . The no-bath result shown in Fig. 1 completely reproduces the behavior. Conversely, when the environmental bath is attached, deviations from the no-bath case are observed. The deviations become smaller with the reduction in  $T$  and  $\lambda$ . Furthermore, the other case of NOT gate shows a similar trend.

The resultant fidelity ( $F$ ) as a function of excitonic coupling ( $J$ ) is shown in Fig. 2. The result shows that  $J = 200 \text{ cm}^{-1}$  does not provide good  $F$  scores. Conversely,  $J$  over  $1000 \text{ cm}^{-1}$  provides a good  $F$  score, even when the environmental condition is not particularly special; for instance  $(T, \lambda) = (320 \text{ K}, 320 \text{ cm}^{-1})$ . Thus, the possibility that a molecular system with such a large excitonic coupling can work as a logic gate of computation is established. Notably, the setting of  $J$  demands another condition of energy level; the Hadamard case with  $J = 1000 \text{ cm}^{-1}$  demands  $|\varepsilon_1 - \varepsilon_2| = 2000 \text{ cm}^{-1}$ , as expressed by Eq. (5).

This study shows that excitonic coupling  $J$  is highly dominant and an extremely high value of  $\sim 1000 \text{ cm}^{-1}$  is required. Thus, the possibility of realizing such a condition is discussed through a comparison of existing molecular systems. Biological systems of proteins FMO, PE545, PE645, LH-I, and LH-II serve for light harvesting during photosynthesis. For FMO with seven or eight chlorophylls, the  $J$  value is at most  $\sim 90 \text{ cm}^{-1}$ . As another light-harvesting molecule, PE645 has a larger  $J$  of  $319 \text{ cm}^{-1}$ . However, the values are still small compared to the present requirement of  $J > 1000 \text{ cm}^{-1}$ .

For light-harvesting complexes LH-I and LH-II, reported values vary among different studies. Some studies have considered significantly large values, such as  $J = 1800$  and  $1600 \text{ cm}^{-1}$  for LH-I and  $J = 806$  and  $730 \text{ cm}^{-1}$  for LH-II. Although such large couplings can provide a good fidelity score, most studies have provided smaller values,  $200\text{--}500 \text{ cm}^{-1}$ , which are considered most likely at present.

Castellanos *et al.* [2] embedded cyanine dyes into a DNA scaffold as a test example of exciton quantum computing. Such DNA-based dye systems are considered candidates for molecular excitonic circuits, where the excitonic coupling is in the range of  $360\text{--}530 \text{ cm}^{-1}$ . The range is larger than that of FMO and PE645 cases. However, the range is not yet sufficient for high-fidelity computation.

Thus, extremely high excitonic coupling is required for realizing quantum logic gate operations. The presented evaluations based on fidelity show the requirement of a strong excitonic coupling for over  $\sim 1000 \text{ cm}^{-1}$  to realize high-fidelity computation of  $F > 0.98$ . Currently, a satisfactory molecular system is difficult to obtain. However, organic conjugate molecules arranged suitably can offer good results, wherein molecular arrangement with orientation tuned at a short distance is required. A more detailed examination involving electronic state calculations is required.

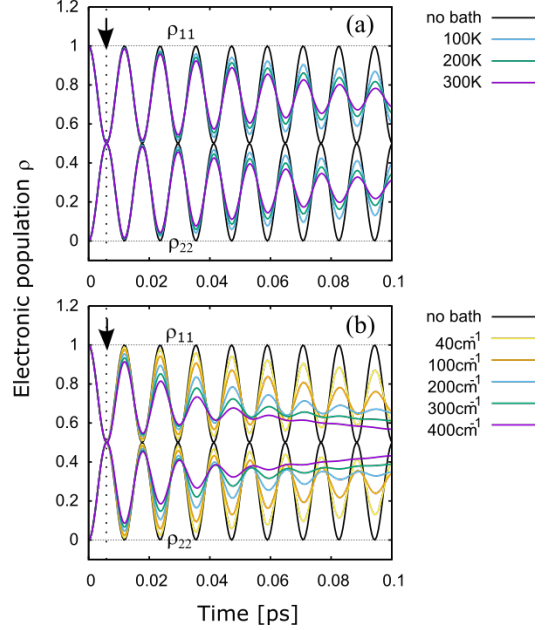


Fig. 1: Electronic populations ( $\rho_{11}$  and  $\rho_{22}$ ) of the Hadamard gate with  $J = 1000 \text{ cm}^{-1}$ : (a)  $T$ - and (b)  $\lambda$ -dependences. The “no bath” result denotes that the system is not coupled with the environment. The arrows denote the time ( $\tau \sim 0.00584 \text{ ps}$ ) at which readout is expected to be conducted.

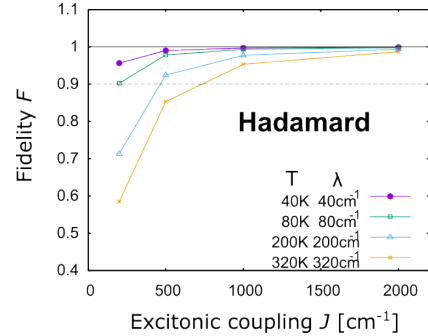


Fig. 2: Fidelity for the Hadamard gate ( $T$ : temperature,  $\lambda$ : reorganization energy).

## Acknowledgments

The author is grateful to Dr. Y. Kurosaki and Dr. M. Adachi for their helpful discussions. This work was supported by JSPS KAKENHI Grant Number 22K03480. Parts of the computation were carried out on the supercomputer SGI8600 at the Japan Atomic Energy Agency.

## References

1. M. A. Nielsen and I. L. Chuang, *Quantum Computation and Quantum Information*, Cambridge University Press, 2011.
2. M. A. Castellanos, A. Dodin, and A. P. Willard, *Phys. Chem. Chem. Phys.* **22**, 3048-3057, 2020.
3. Y. Yonetani, *Chem. Phys.* **570**, 111860, 2023.
4. H. Wang, X. Song, D. Chandler, and W. H. Miller, *J. Chem. Phys.* **110**, 4828-4840, 1999.

# Sub-nanometer scale depth patterning on sapphire crystal

ISHINO Masahiko



X-ray Ultrafine Structure Processing Project, Department of Quantum Applied Photonics

Surface processing using pulse laser ablation is a widely used. In laser surface processing, irradiation wavelength shortening is essential to realize small and precise subject formation. Recently, soft X-ray lasers including plasma-based soft X-ray lasers and soft X-ray free electron lasers (SXFELs), having emission photon energy (or oscillation wavelength) in the soft X-ray region, are widely available. Applications relative to surface processing using such soft X-ray laser sources are under study. Dinh et al. [1] reported femtosecond soft X-ray laser processing and revealed that a 120 eV (wavelength of 10.3 nm) laser process was useful for fine processing, with no heat-affected-zone (HAZ) on a Si surface. Mikami et al. [2] reported a decrease in the damage threshold of SiO<sub>2</sub> due to impurities by performing a 92 eV (13.5 nm) SXFEL irradiation experiment. The short penetration depth and large absorption of soft X-rays into materials cause an efficient deposition of laser energy and small damage thresholds. Si and SiO<sub>2</sub> are essential materials in electronic devices, wherein small and precise surface machining is key during semiconductor manufacturing.

Another essential substrate material includes sapphire crystal, which has a high dielectric constant and thermal conductivity [3]. The surface processing of sapphire crystals requires investigations to analyze their contributions toward a wide range of industrial applications. Additionally, focusing devices that convert a soft X-ray laser beam to a sub-micrometer order spot-size beam have been developed [4]. Therefore, the feasibility of nanometer-scale surface processing by a soft X-ray laser should also be discussed. In this study, the feasibility of surface processing on a sapphire crystal is examined by using femtosecond SXFEL pulses [5].

For this study, Al and sapphire crystal were used as target samples because sapphire is an Al<sub>2</sub>O<sub>3</sub> crystal and Al is considered as a reference. An optical grade sapphire crystal with a c-plane orientation of 10×10 mm and thickness of 0.5 mm was prepared, and the surface roughness was evaluated as ~0.15 nm (root-mean-square value). The Al sample was prepared as a 500 nm thick film, which was evaporated onto a sapphire substrate. A 500 nm thick Al film could also be used as the bulk sample because the film shows the same processing tendency [6].

The femtosecond SXFEL laser irradiation experiments were performed using a soft X-ray beamline of BL1 at the SPring-8 Angstrom Compact Free Electron Laser (SACLA) facility [7]. The SXFEL pulse had a pulse duration of  $28 \pm 5$  fs [8], and the emission photon energy was tuned to 120 eV (10.3 nm). The SXFEL beam was focused onto the sample surface using a two-staged focusing system, comprising the Kirkpatrick–Baez (K–B) mirror focusing system and an ellipsoidal mirror [4]. The focal spot size was measured using the knife-edge scanning method, the spot size defined by the full width at half maximum was evaluated as 0.5–0.6  $\mu\text{m}$  (horizontal and vertical), and the focal area was  $\sim 0.25 \mu\text{m}^2$ . To reduce and control irradiation fluences onto the sample surfaces, Zr and Si thin films of various thicknesses were adapted to attenuate the pulse energy. Transmittance calibration of the thin films was performed in

advance for the evaluation beamline of BL-11D at the High Energy Accelerator Research Organization-Photon Factory (KEK-PF). As each pulse energy was monitored by a gas intensity monitor, every irradiation fluence was calculated from the measured energy and focal area.

Figures 1(a) and 1(b) show irradiation fluence dependence damage depths on (a) Al and (b) sapphire crystal, respectively. All plots denoted by red rectangles show damage depths created by a single-shot regime. The lines shown in the figures represent fitting to effective ablation depth [9]. The damage thresholds were defined as a fluence when the depth was zero, such as a cross point between the horizontal axis and fitted line.

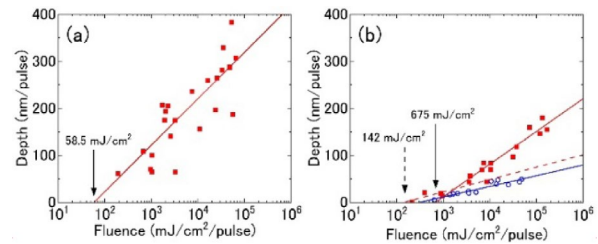


Fig. 1. Irradiation fluence dependence on damage depths of (a) Al and (b) sapphire crystal surfaces.

Herein, the tabulated penetration depths of Al and Al<sub>2</sub>O<sub>3</sub> are 31.7 and 30.2 nm [10], respectively. For Al, the effective penetration depth and the damage threshold are estimated from the fitting calculation as 42.9 nm and 58.5 mJ/cm<sup>2</sup>, respectively. The obtained effective penetration depth of Al is comparable to the referred value, and the estimated damage threshold of Al is consistent with the theoretical value assuming 89 eV soft X-ray laser irradiation [11]. For sapphire crystal, the slope of the damage depth curve changes in the fluence region of 3000–10,000 mJ/cm<sup>2</sup>. Two different fitting lines are adopted (dashed and solid red lines), as shown in Fig. 1(b). The estimated effective penetration depths are 11.4 and 30.2 nm for low and high fluence regions, respectively. Furthermore, the estimated damage thresholds for low and high fluence regions are 142 and 675 mJ/cm<sup>2</sup>, respectively. When the single-shot irradiation fluence is higher, above 10,000 mJ/cm<sup>2</sup>, the effective penetration depth agrees with the referred value. Conversely, when the single shot fluence exists around the damage threshold, the effective penetration depth is 1/3 times shorter than that of the referred value. The damage depths formed by accumulations of 10 SXFEL pulse shorts are shown in Fig. 1(b) as blue circles. The total irradiation energy and measured damage depth are divided by the shot number. All 10-shot damage depths (averaged value per single shot) almost overlap with single-shot depths in the low fluence region, and the fitted line (dashed blue line) is close to that at the low fluence region. The estimated effective penetration depth and damage threshold for the 10-shot regime are 9.8 nm

and 308 mJ/cm<sup>2</sup>, respectively. A femtosecond laser ablation study generally observes and discusses the incubation effect involving the reduction of damage threshold value by multiple laser pulse irradiations [12]. In the sapphire crystal, a reduction in threshold from 675 to 308 mJ/cm<sup>2</sup> is observed. Thus, the extremely short effective penetration depth around the threshold implies the potential for shallower surface processing than the referred values.

The surface morphologies of the irradiated area are observed using an atomic force microscope (AFM). Similar observation Figures are presented in an original article [5]. On the Al surface, rims are observed on the periphery of the irradiated spot. When the irradiation fluence decreases, the damage size grows small, but rim and dome structures remain until the threshold. Thus, the presence of HAZ on the Al surface is beyond control because the first change in the Al surface structure is the melting of the surface due to the splash of the molten layer [6]. On the sapphire crystal surface, the damaged structure reflecting the morphology of HAZ is small. Therefore, the experimental results imply a potential for the realization of surface processing without HAZ.

To confirm the feasibility of HAZ-free shallow surface processing as aforementioned, shallow patterns with a shorter depth than the attenuation length was drawn on the sapphire crystal. The experimental results are shown in Figs. 2(a) and 2(b). Figure 2(a) shows the AFM image of four irradiation damages. Each damage was obtained by the single-shot irradiation regime. The sample surface was set to 20 μm before the best focal position, such that the sample was located close to the light source.

Owing to the aberration of focusing optics, the focal shape of SXFEL pulses is not circular but has line-like profiles. Damage line widths and lengths on the sapphire crystal are ~100–200 nm and ~2 μm, which represent the focal sizes themselves. Damage depths on the crystal are ~0.5 nm, as shown in Fig. 2(b). Irradiation fluences for these patterns are estimated to be ~170 mJ/cm<sup>2</sup>, which nearly agrees with the damage threshold value. By repeating SXFEL irradiation and sample movement, long lines with micrometer lengths were drawn on the crystal, as shown in Fig. 2(c). For long-line drawings, the sample stage was scanned at 50 μm/s. SXFEL pulses were irradiated at an interval of 0.83 μm/pulse because the repetition rate of SXFEL was set to 60 Hz.

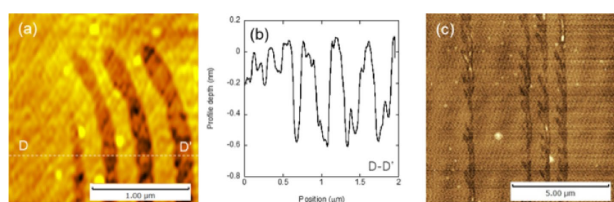


Fig. 2. (a) AFM image and (b) cross-sectional depth profile of the laser patterning process on a sapphire crystal by SXFEL pulse irradiations of ~170 mJ/cm<sup>2</sup>. (c) AFM image of line pattern writing on a sapphire crystal.

The lattice constants of the sapphire crystal were  $a = 0.477$  nm (4.77 Å) and  $c = 1.304$  nm (13.04 Å). The damage depths on the crystal are equivalent to some thin atomic layer in a single lattice along the  $c$ -axis. At the low fluence region, especially around the ablation threshold, a spallation process is known as an ablation regime [13]. The depth by spallation damage is comparable with the penetration depth [14]. The damage structure with an extremely shallow depth on the sapphire crystal is completely different from the known spallation structures. To our best knowledge, this is a novel damage phenomenon, which is known as peeling. Additionally, the peeling process can have the potential to be one of high-precision surface processing.

In this study, SXFEL irradiation damage phenomena are characterized for metal Al and sapphire crystal. For Al, HAZ involving rim structures at the edges is formed. For sapphire, HAZ has little effect on the damaged structure, although the damage threshold is 2.4 times higher than that of Al. Additionally, the effective penetration depth is confirmed to be 1/3 times shorter than that of the referred value around the damage threshold. Further, the peeling process is demonstrated on a sapphire surface, which represents the damaged structure with an extremely shallow depth. The peeling process demonstrated in this study can serve as a milestone in the pursuit of ablation science and surface machining.

## Acknowledgments

This work was supported by the JSPS KAKENHI Grant (Nos. JP19K15402, JP21H03750, JP23H01884), and the Quantum Leap Flagship Program of the Ministry of Education, Culture, Sports, Science and Technology of Japan (MEXT Q-LEAP JPMXS0118067246, JPMXS0118070187). XFEL experiments were performed at BL1 in SACLA with the approval of the Japan Synchrotron Radiation Research Institute (JASRI) (Proposal No. 2020A8024). Transmittance calibration of thin film filters was performed at BL11D of the Photon Factory, KEK Japan (Proposal Nos. 2017G638 and 2019G547).

## References

1. T.-H. Dinh *et al.*, *Commun. Phys.* **2**, 150 (2019).
2. K. Mikami *et al.*, *Opt. Lett.* **45**, 2435 (2020).
3. V. N. Kurlov, *Encyclopedia of Materials: Science and Technology* 2nd ed. (Pergamon Imprint, 2001).
4. H. Motoyama *et al.*, *J. Synchrotron Radiat.* **26**, 1406 (2019).
5. K. Mikami *et al.*, *Opt. Lett.* **48**, 5041 (2023).
6. M. Ishino *et al.*, *Appl. Phys. A* **124**, 649 (2018).
7. S. Owada *et al.*, *J. Synchrotron Radiat.* **25**, 282 (2018).
8. S. Owada *et al.*, *J. Synchrotron Radiat.* **27**, 1362 (2020).
9. S. Preuss *et al.*, *Appl. Phys. A* **61**, 33 (1995).
10. B. L. Henke *et al.*, *At. Data Nucl. Data Tables* **54**, 181 (1993).
11. S. V. Starikov *et al.*, *Appl. Phys. B* **116**, 1005 (2014).
12. Y. Jee *et al.*, *J. Opt. Soc. Am. B* **5**, 648 (1988).
13. D. Perez and L. J. Lewis, *Phys. Rev. B* **67**, 184102 (2003).
14. N. A. Inogamov *et al.*, *Appl. Phys. A* **101**, 87 (2010).

# Effect of multiply excited states on the EUV emission from yttrium-like tin

SASAKI Akira



X-ray Ultrafine Structure Processing Project, Department of Quantum Applied Optics

Extreme ultraviolet (EUV) lithography has been realized based on laser-pumped plasma (LPP) tin sources. More than 500 W of EUV power at a wavelength of 13.5 nm has been obtained by irradiating tin droplets using a CO<sub>2</sub> laser [1]. In laser-produced plasmas with electron temperatures in the range of 20–50 eV, tin ions are ionized to 8 to 13 times their ionized states for emitting EUV radiation through 4d-4f and 4p-4d atomic transitions. In contrast to the emission spectrum of lighter elements, the atomic transition of tin ions consists of a larger number of fine structure lines, which appear as a broad peak called an unresolved transition array (UTA). Due to the effect of configuration interaction (CI), the wavelengths of the 4d-4f and 4p-4d transitions are constant over charge states, resulting in the emission spectrum of tin plasma showing a single peak near 13.5 nm [2].

Improvements to the power and efficiency of EUV sources are required to enhance the productivity of present scanners and realize future scanners with a numerical aperture of NA > 0.5 for exposure to finer images. Further improvements to conversion efficiency (CE), which represents the ratio of the power of EUV light at the intermediate focus to that of the pumping laser, are being pursued [3] because even the current LPP EUV sources produce EUV emissions with 5 % CE. The spectral width that is useful as an EUV source for lithography is limited to 2 % by the bandwidth of multilayer optics. Therefore, a plasma source should produce EUV emission with a high spectral purity that corresponds to the in-band emission to the total emission.

Figure 1 shows the energy level structure of yttrium-like tin (Sn<sup>11+</sup>). A tin ion has the ground configuration of 4d<sup>3</sup> and a large number of multiply excited states, which have an excitation energy below the ionization limit for a large population and contribute to the EUV emission through 4d-4f and 4p-4d UTA. The emission from the multiply excited states appears at the shorter and longer wavelength side of the main peak due to the screening effect of holes in the 4d shell and additional electrons in the outer orbits. Therefore, although the emission from multiple excited states can contribute to EUV emission, the emission can appear outside the required emission band, causing the degradation of spectral purity. Furthermore, the emission may not contribute to an increase in usable EUV power. The effect of opacity can cause additional broadening of UTA. Therefore, a better understanding of the spectral profile of UTA and analysis of spectral purity are necessary for improvements to the power and efficiency of EUV sources [4].

Although the atomic processes in tin plasma are complex, a collisional radiative model of tin ions has been developed by using computational atomic data that include atomic energy levels and rates of collisional and radiative processes for the analysis of EUV spectra [5].

The effect of emission from multiple excited states should become significant when a solid-state laser is used as a pumping source because the density of plasma depends on the wavelength of the laser and should be higher to increase collisional excitation to multiple excited states. The efficiency of solid-state lasers is

higher than that of CO<sub>2</sub> lasers, but further optimization of pumping conditions is necessary to increase the source power and efficiency through the analysis of EUV emission spectra [6,7].

In previous studies, the resonance lines from each ion have been investigated, which correspond to emission from one electron excited state to the ground state. The results show that the emission spectrum from CO<sub>2</sub> LPP can be reproduced by calculations. Furthermore, the calculations using radiation hydrodynamics simulations predict CE > 5 %, thereby providing a valuable guide for the realization of EUV lithography [8]. In this study, a structural analysis of yttrium-like tin ion (Sn<sup>11+</sup>) is performed by extending the model to consider the effect of emission from multiple excited states on the EUV spectrum.

A model of the yttrium-like tin ion is developed based on a configuration average (CA) model, including multiple excited states. The atomic state is defined by a set of orbitals determined by principal, orbital quantum number ( $n, l$ ), and occupation number for each orbit. Groups of levels consisting of a common core and one excited electron are defined. Then, the model is developed by including groups of atomic states and determining the number of groups. The number of groups is increased, and the size of the model is obtained by choosing the core state as an ascending order of energy until the convergence of the population and emission spectra.

The set of atomic states of each ion is determined from the set of ion states, one charge higher than the target ion. For instance, the set of states of yttrium-like ion (Sn<sup>12+</sup>) is determined by taking the direct product of strontium-like (Sn<sup>11+</sup>) core states and one electron, as shown in Fig. 2. Then, the states with unphysical configuration and duplicated states are removed. All electron orbits up to  $n_{max} = 8$  and  $l_{max} = 3$  are considered. Consequently, the energy level of yttrium-like ion is calculated using the HULLAC code [9], and the set of core states that is used to generate the atomic state of zirconium-like tin (Sn<sup>10+</sup>) is selected. In the present method, the atomic model is determined by repeating the generation of a set of atomic states and the calculation of the energy level using the HULLAC code. Based on the CA model, the present method is reproducible using a few parameters such as the range of charge states,  $n_{max}$ ,  $l_{max}$ , and the number of state groups with the same core and one excited electron [10].

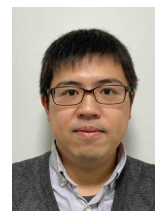
Figure 1 shows ~20 state groups of yttrium-like tin that have low excitation energy. Large populations are produced from core states of strontium-like tin. The first five cores include 4d<sup>2</sup>, 4d5s, 4p<sup>5</sup>4d<sup>3</sup>, 4d4f, and 4d5p, from which the ground state of 4d<sup>3</sup> and excited states of 4d<sup>2</sup>nl, 4d5s<sub>nl</sub>, 4p<sup>5</sup>4d<sup>3</sup>nl, 4d4f<sub>nl</sub>, and 4d5p<sub>nl</sub> are produced. The intensity of UTA is indicated by the thickness of the line to show that the 4d-4f and 4p-4d UTA to the ground state such as 4d<sup>3</sup>-4d<sup>2</sup>4f and 4d<sup>3</sup>-4p<sup>5</sup>4d<sup>4</sup>, along with UTA from multiple excited states such as 4p<sup>5</sup>4d-4p<sup>5</sup>4d<sup>3</sup>4f, 4p<sup>5</sup>4d-4p<sup>4</sup>4d<sup>5</sup>, and 4p<sup>5</sup>4d34f-4p<sup>5</sup>4d<sup>2</sup>4f<sup>2</sup> significantly contribute to emission.

Figure 3(a) shows the EUV spectrum from yttrium-like tin, calculated based on the model presented in Fig. 1. The population of the atomic state at an electron temperature of 35 eV is



# Rapid solution mixing in a micro-mixer with free-impinging jets

ENDO Tomoyuki



Ultrafast Electronic Dynamics Project, Department of Quantum Applied Photonics

Intermediates in chemical reactions driven by solution mixing have been investigated to understand their reaction mechanisms and driving forces. However, the identification of intermediates with lifetimes of a few seconds or less is difficult with a spectroscopic technique for steady states. Rapid solution mixing techniques including continuous-flow [1] and stopped-flow [2] methods are used to observe the intermediates. Typically, mixing time by such methods is on a timescale of milliseconds. To access short-lived chemical species on a timescale of microseconds, a variety of micro-mixers with different inner structures has been proposed [3-5], and the shortest mixing time in nanoseconds has been reported [6]. Mixing time and mixing efficiency can be controlled by changing the inner structure. However, precise design and microfabrication are required to achieve the desired mixing time.

Other simple approaches for rapid solution mixing involve impinging two liquid jets in confined T-shaped and Y-shaped reactors or in free space. With a free-impinging jet technique, a thin liquid-sheet jet can be formed. A mixing time shorter than the aggregation time of tens of milliseconds [7] can be achieved, and the potential of rapid mixing in microseconds has been discussed on the basis of the dissipation energy [8] in the liquid-sheet jet. However, the mixing time in free-impinging jets has not been directly measured yet, and the mixing mechanism is still under discussion. In this study [9], we measured mixing time in the liquid-sheet jets following a conventional technique using a quenching reaction of N-acetyl-L-tryptophan amide (NATA) by N-bromosuccinimide (NBS). Additionally, the theoretical mixing time was calculated by two different models assuming laminar and turbulent flows to clarify the mixing mechanism in the liquid-sheet jets.

Details of the experimental setup for the formation and characterization of the liquid-sheet jet are described elsewhere [9]. Briefly, two cylindrical jets of H<sub>2</sub>O were impinged to form the liquid-sheet jet. The cylindrical jet diameter and colliding angle were fixed at 50  $\mu\text{m}$  and 48 deg, respectively. In this study, we obtained liquid-sheet jet  $\sim 4$  mm long,  $\sim 1$  mm wide, and a few micrometer thick. A schematic of the experimental setup to measure the mixing time is shown in Fig. 1. The output of a Ti:Sapphire laser system (central wavelength of 800 nm) was used to generate an ultraviolet (UV) pump pulse (266 nm) by using a third-order harmonic generation technique. The obtained

UV pulse was separated from the residual second harmonic and fundamental pulses by using dielectric mirrors. The liquid-sheet jet was irradiated with the UV pulses to excite NATA. A bandpass filter (357 nm) with a bandwidth of 44 nm was employed to extract the emission from NATA. A UV CMOS camera with a UV camera lens and an uncoated fused silica lens ( $f = 50$  mm) was used to detect the emission from NATA, which was oxidized by NBS to form a bromohydrin compound. Since NBS and the products are non-fluorescent species, the intensity at 357 nm is proportional to the amount of NATA in the liquid-sheet jet.

Figure 2(a) shows an emission image from NATA (50  $\mu\text{M}$ ) in the liquid-sheet jet formed with NATA solution and pure H<sub>2</sub>O. The liquid-sheet jet flowed from the top to the bottom. To compensate for the non-uniformity due to the spatial distribution of pump pulse intensity and fluorescence collection efficiency, the emission image taken with NBS was normalized by the image taken without NBS. A normalized image with an NBS concentration of 32 mM is shown in Figure 2(b). The relative intensity clearly decreased as  $z$  increased, reflecting the quenching reaction of NATA by NBS. The relative intensities along the  $z$ -axis are shown in Figure 2(c) at three different NBS concentrations of 8, 16, and 32 mM. The curves were obtained by averaging over 20 pixels (corresponding to  $\sim 53$   $\mu\text{m}$ ) along the  $y$ -axis, showing position and concentration dependencies.

Since the quenching reaction of NATA by NBS can be regarded as a pseudo-first-order reaction in the presence of excess NBS, the relative intensity shows an exponential decay. A least-squares fit of a mono-exponential function was performed for the relative intensities. The three fitting curves crossed at  $z = 0.20$  mm, which was regarded as the effective initial position for mixing. The mixing time was estimated from the distance between the effective initial position and the position where the absolute value of the residual between the experimental and fitting results became smaller than 0.01 ( $z = 1.0$  mm). Furthermore, the maximum time range was determined from the position where the absolute value of the residual between the experimental and fitting results became larger than 0.01 ( $z = 2.5$  mm). Since the flow speed of the liquid-sheet jet was measured to be 22.3 m/s in the present experimental condition, the mixing time and the maximum time range were estimated to be 36(3)  $\mu\text{s}$  and 103(3)  $\mu\text{s}$ , respectively. In addition, an obtained second-order rate constant of the quenching reaction of NATA by NBS was  $k =$

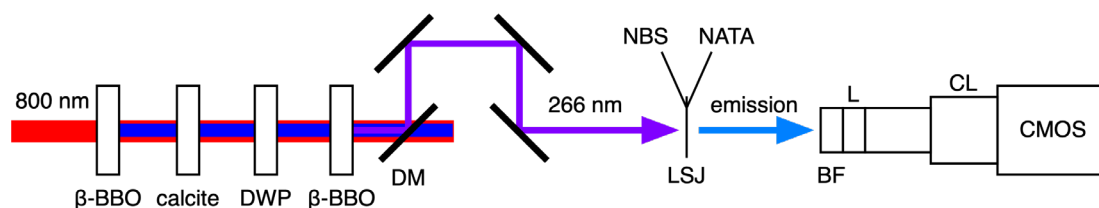


Figure 1. Schematic of the experimental setup for mixing time measurement. BBO: barium borate crystal, DWP: dual-wavelength waveplate, DM: dielectric mirror, LSJ: liquid-sheet jet, BF: band-pass filter, L: lens, CL: camera lens, CMOS: complementary metal-oxide-semiconductor camera.

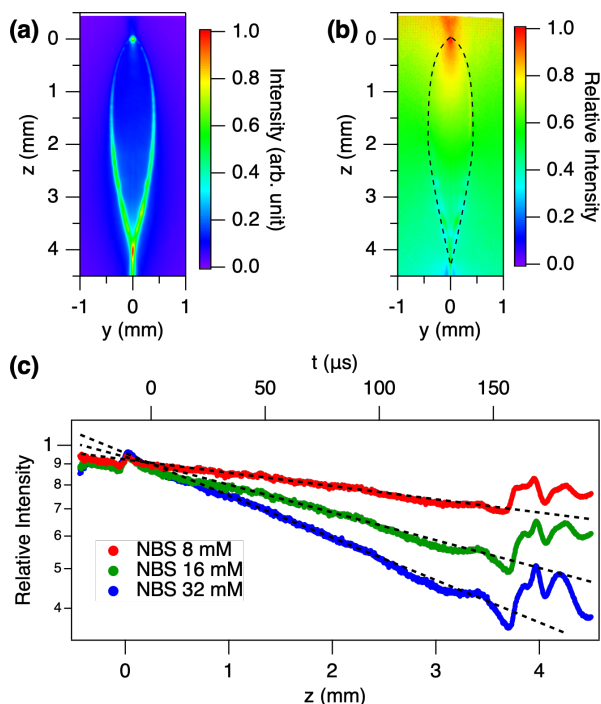


Figure 2. (a) Emission image from NATA (50  $\mu\text{M}$ ) at 357 nm without NBS. (b) Emission image taken with an NBS concentration of 32 mM normalized by (a). Dotted line denotes a rim of the liquid-sheet jet. (c) Relative intensity along the  $z$ -axis at three different NBS concentration of 8, 16, and 32 mM. Dotted lines are the fitting results of a mono-exponential function.

$3.5(3) \times 10^5 \text{ M}^{-1}\text{s}^{-1}$ , which was comparable to previous results of between  $4.1$  and  $7.9 \times 10^5 \text{ M}^{-1}\text{s}^{-1}$  with a confined micro-mixer [10, 11]. Thus, two solutions were mixed uniformly and efficiently in the micro-mixer with free-impinging jets.

The details of simulation with a laminar flow model are described elsewhere [9]. Briefly, the simulation for the laminar flow was based on the Fick's law of diffusion and the fact that the quenching reaction of NATA by NBS was a second-order reaction. Two-dimensional plots of the simulated NATA concentration without and with NBS are shown in Figures 3(a) and (b), respectively. For comparison with the experimental results, the simulated NATA concentration was integrated along the  $x$ -axis. To remove the effect of liquid-sheet jet thickness, the integrated intensity with NBS was normalized by that obtained without NBS. The relative intensity plotted in Fig. 3(c) exhibits a large discrepancy from the experimental result, indicating that laminar mixing is not a dominant mixing mechanism in the liquid-sheet jet.

The mixing time in turbulent flow is calculated on the basis of the energy dissipation rate ( $\epsilon$ ) in the impinging area [8]. The supplied and removed kinetic energy fluxes to/from the impinging area were evaluated from the measured pressure and flow speed. In this study,  $\epsilon$  attains  $1.62 \times 10^8 \text{ W/kg}$  owing to a tiny volume of 0.121 nL impinging zone. From the empirical formula [12], the mixing time  $\tau_{\text{mix}}$  is given by

$$\tau_{\text{mix}} = 0.15\epsilon^{-0.45}.$$

The mixing time in the liquid-sheet jet of this study was calculated to be 30.3  $\mu\text{s}$ , which was in great agreement with the experimental value of 36(3)  $\mu\text{s}$ . Thus, the mixing mechanism in the liquid-sheet jet can be explained by turbulent mixing rather than laminar mixing, and no clear interface between  $\text{H}_2\text{O}$  solutions was formed for the present experimental conditions.

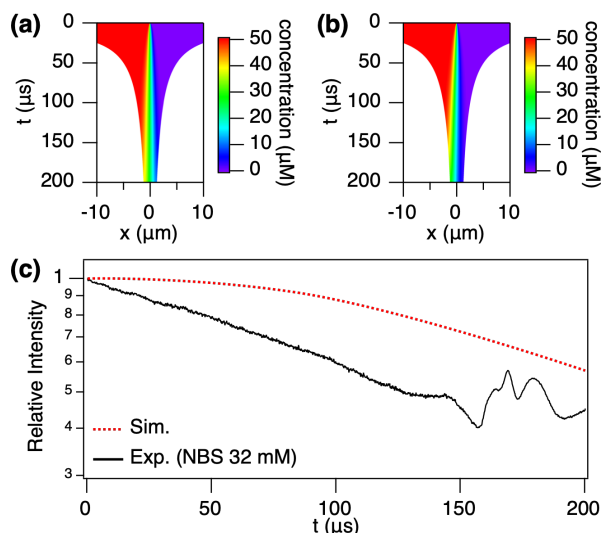


Figure 3. Simulated NATA concentration in the liquid-sheet jet (a) without NBS (b) with NBS concentration of 32 mM. (c) Relative fluorescent intensity as a function of the time. Black solid and red dotted lines correspond to the experimental and simulated results, respectively.

In summary, the mixing time in the liquid-sheet jet was measured, and the potential of the liquid-sheet jet as a micro-mixer was demonstrated. The mixing time of 36  $\mu\text{s}$  was achieved for  $\text{H}_2\text{O}$  solutions and the result was in great agreement with the mixing time based on the dissipation energy in turbulent flow. The free-impinging liquid-sheet jet technique provides an ultrathin liquid target even in a vacuum suitable for absorption spectroscopy in a soft X-ray region, opening up a new way for investigating ultrafast electron dynamics in mixing-driven chemical reactions using ultrashort laser pulses such as high-order harmonics with attosecond time resolution.

## Acknowledgments

The author thanks Dr. Ryuji Itakura for his contributions, Prof. Toshinori Suzuki (Kyoto Univ.), and Dr. Masaaki Tsubouchi for their support in the measurement with the ICCD camera. This research was supported by QST President's Strategic Grant (Exploratory Research).

## References

1. H. Hartridge, and F. J. W. Roughton, *Proc. R. Soc. London. Ser. A* **104**, 376-394 (1923).
2. B. Chance, *Journal of the Franklin Institute* **229**, 455-476 (1940).
3. S. A. Pabit, and S. J. Hagen, *Biophysical Journal* **93**, 2872-2878 (2002).
4. H. Song, and R. F. Ismagilov, *Journal of the American Chemical Society* **125**, 14613-14619 (2003).
5. S. Mitić et al., *PLoS ONE* **12**, e0185888 (2017).
6. S. Mitić et al., *Analytical Biochemistry* **469**, 19-26 (2015).
7. B. K. Johnson, and R. K. Prud'homme, *Physical Review Letters* **91**, 118302 (2003).
8. R. S. Abiev, and A. A. Sirotkin, *Fluids* **5**, 179 (2020).
9. T. Endo, and R. Itakura, *Bulletin of the Chemical Society of Japan* accepted [doi: 10.1093/bulscj/uoad021]
10. O. Bilsel, C. Kayatekin, L. A. Wallace, and C. R. Matthews, *Review of Scientific Instruments* **76**, 014302 (2005).
11. M. R. Shastry, S. D. Luck, and H. Roder, *Biophysical Journal* **74**, 2714-2721 (1998).
12. L. Falk, and J.-M. Commenge, *Chemical Engineering Science* **65**, 405-411 (2010).

# Theoretical and numerical analysis of the damage threshold of silicon

OTOBE Tomohito



Ultrafast Electronic Dynamics Project, Department of Quantum Applied Photonics

Laser processing studies of semiconductors including silicon are crucial for practical applications in the field of nanofabrication. The interaction of intense, femtosecond pulses with a target provides a high-resolution energy transfer with minimum damage to the surrounding area. Laser excitation of semiconductors involves complex physics of photo-absorption, impact ionization, recombination, and re-distribution of energy. The excitation includes the dynamics of interactions that lead to permanent structural changes through thermal and non-thermal effects. Various processes causing damage in silicon film have been explored by experimental studies [1-4]. Additionally, the effect of laser parameters such as wavelength and pulse duration can affect threshold fluence by causing damage to silicon [4,5].

Generally, theoretical modeling of laser excitation in silicon involves the use of a two-temperature model (TTM) that is widely implemented to study the evolution of electron and lattice dynamics during laser excitation. In our previous work, we developed a modified nTTM, treating the evolution of three quasi-temperatures in the conduction band (CB), valence band (VB), and lattice. We found that the three-temperature model (3TM) shows reasonable agreement for various experimental results [6,7].

The electron and hole densities ( $n_{e(h)}$ ) are calculated as

$$\begin{aligned} \frac{\partial n_{e(h)}}{\partial t} = & \frac{\alpha I}{\hbar\omega_0} + \frac{\beta I^2}{2\hbar\omega_0} - \gamma_e n_e n_e n_h - \gamma_h n_h n_h n_e \\ & + \frac{1}{2}(\theta_e n_e + \theta_h n_h) + \nabla D_{e(h)} \cdot \vec{j}_{e(h)} + D_{e(h)} \nabla \cdot \vec{j}_{e(h)} \\ & - (+)n_{e(h)} \nabla \mu_{e(h)} \cdot \vec{F} - (+)\mu_{e(h)} \nabla n_{e(h)} \cdot \vec{F} \\ & - (+)\mu_{e(h)} n_{e(h)} \nabla \cdot \vec{F} \end{aligned} \quad (1)$$

where  $\omega_0$  is the laser frequency and  $\alpha$  is the single photon absorption coefficient for a transition from VB to CB.  $\beta$  is the two-photon absorption coefficient obtained from density functional theory (DFT) calculations, when  $2\hbar\omega_0 > E_g$ , where  $E_g$  is the optical gap. The time-evolution of the temperatures is calculated as

$$\begin{aligned} C_{e(h)} \frac{\partial T_{e(h)}}{\partial t} = & m_{r,e(h)} (\alpha_f I + \beta I^2) \\ & + E_g \gamma_{e(h)} n_{e(h)} n_{e(h)} n_{h(e)} - \frac{C_{e(h)}}{\tau} (T_{e(h)} - T_l) - \nabla \cdot \vec{w}_{e(h)} \\ & - \frac{\partial n_{e(h)}}{\partial t} \left( m_{r,e(h)} E_g + \frac{3}{2} k_B T_e H_{\frac{1}{2}}^{\frac{1}{2}}(n_{e(h)}) \right) \\ & - m_{r,e(h)} n_{e(h)} \left( \frac{\partial E_g}{\partial T_l} \frac{\partial T_l}{\partial t} + \frac{\partial E_g}{\partial n_{e(h)}} \frac{\partial n_{e(h)}}{\partial t} \right) \end{aligned} \quad (2)$$

$$C_l \frac{\partial T_l}{\partial t} = -\nabla \cdot (\kappa_l \nabla T_l) + \frac{C_e}{\tau} (T_e - T_l) + \frac{C_h}{\tau} (T_h - T_l) \quad (3)$$

The third and fourth terms in Eq. (2) account for energy loss due to electron-lattice interaction and energy current ( $\vec{w}_{e(h)}$ ). The last two terms on the right-hand side include the carrier density changes and band gap energy. Here,  $H_{\frac{1}{2}}^{\frac{1}{2}}(\eta) = F_{\frac{1}{2}}(\eta)/F_{\frac{1}{2}}(\eta)$  and  $F_{\frac{1}{2}}(\eta)$  is the Fermi integral. The heat capacities  $C_{e(h)}$  are calculated from the carrier densities and temperatures.  $\alpha_f$  is the absorption coefficient for one-photon absorption, including the free carrier absorption, calculated using the Drude model.  $T_l$  is calculated following an empirical model, where the term for carrier temperature is replaced by terms for electron and hole temperatures, as expressed in Eq. (2). Herein,  $\kappa_l$  is the thermal conductivity. Further details on theory and definitions are provided in previous studies [6,7].

The effect of target structure on dynamics during laser processing can be significant, depending on the applications. In the case of a silicon film of thickness less than the penetration depth of the pulse, reflection from the rear surface of the film can interfere with the field within the film, altering the effective pulse intensity and thus, the dynamics. In the case of silicon films with nano-scale thickness, a lower damage threshold can be observed in the film and on the rear surface as compared to the front surface of the film. In this study, the thickness dependence of the laser damage threshold of silicon thin films is examined by employing 3TM with Maxwell's equations.

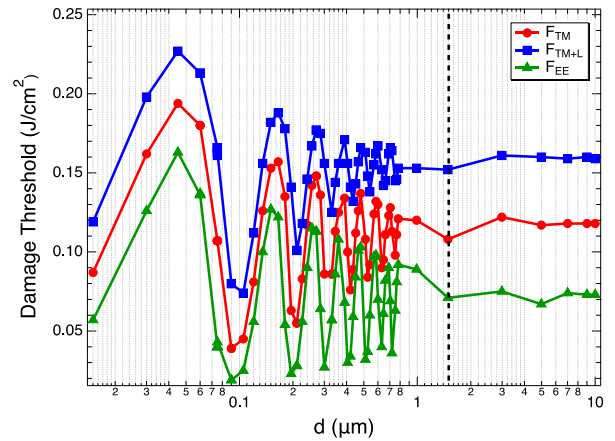


Fig. 1: Calculated thresholds for electron emission (e-emission) ( $F_{EE}$ ), partial thermal melting ( $F_{TM}$ ), and complete thermal melting ( $F_{TM+L}$ ) for  $d$  varying from 0.01-10  $\mu\text{m}$ . Reproduced with permission from Japan Laser Processing Society [8].

In previous our studies, we found that the physical processes for the damage threshold depend on the definition of the threshold. In usual experiments, two definitions are used. One is the threshold defined by the damage probability 0 %, while the second is the threshold from the damage area. The first definition corresponds to the definition of the damage threshold of optical

devices, while the second involves the estimation of 100 % damage probability. The 0 % probability can be explained by the thermal melting threshold ( $F_{TM}$ ) and electron emission ( $F_{ee}$ ). Although the chemical bonds between Si atoms become weak at the melting threshold, the crystal structure is maintained because of its high symmetry. Sometimes, overheating can act as another external force that enhances melting. Electron emission induces the Coulomb force to distort the symmetry. Therefore, the damage is onset when  $F_{TM}$  and  $F_{ee}$  are satisfied. Additionally, the damage occurs in 100 % probability when the energy absorption reaches the bond-breaking threshold ( $F_{BB}$ ). Thus, the chemical reaction by the electron excitation to the anti-bonding state induces the damage process.

Figure 1 shows the calculated threshold  $F_{TM}$ ,  $F_{TM+L}$ , and  $F_{EE}$  values as a function of  $d$  at the front surface. Herein,  $F_{TM+L}$  is the threshold for thermal melting, including latent heat.  $F_{EE}$  is calculated as the incident fluence when the average kinetic energy of the electron reaches the work function of silicon (4.65 eV).  $F_{TM}$  and  $F_{TM+L}$  are calculated as the incident fluences when the melting of the lattice starts and when total latent heat is transferred to the lattice, respectively. According to our previous study,  $F_{TM}$  and  $F_{TM+L}$  coincide with the damage thresholds reported by Allenspacher *et al.* [4] below the pulse duration of 1 ps. The relation of each threshold is always  $F_{TM+L} > F_{TM} > F_{EE}$ , which is consistent with our previous results for bulk silicon with a pulse duration of 70 fs.

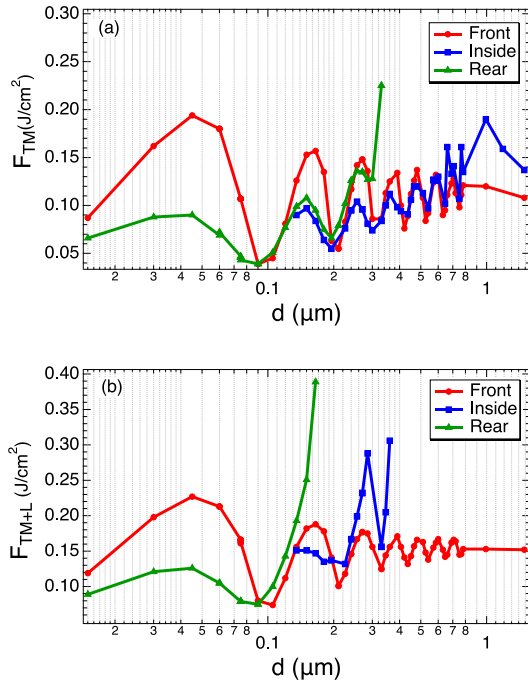


Fig. 2: Comparison of the calculated threshold with varying film thickness on the front surface, inside the film, and rear surface for (a) partial melting ( $F_{TM}$ ) and (b) complete thermal melting ( $F_{TM+L}$ ). Reproduced with permission from Japan Laser Processing Society [8].

All thresholds show oscillation with a period of  $\sim 100$  nm, which indicates that constructive and destructive interference at the front surface affects the damage threshold significantly. The oscillation of thresholds appears to be  $d = \sim 1.5$  μm, which is much smaller than the penetration depth of 775 nm ( $\sim 10$  μm). Since two-photon absorption is the dominant process, the effective penetration depth is significantly reduced in the case of the intense laser pulse. All thresholds are independent of  $d$  above

1.5 μm, thus a silicon film thicker than 1.5 μm can be treated as a bulk system.

The thresholds at the rear surface show oscillation in Fig. 2. Since constructive interference is observed on the rear surface, the results are controversial at first glance. The oscillation at the rear surface can be a result of interference between three components: transmitted field, field reflected from the rear surface, and field reflected from the front of the film. Since the reflected field from the front surface is small, the oscillation of thresholds at the rear surface is weaker than that of the front.

In this study, the film thickness dependence of laser excitation of silicon thin films was examined using 3TM. The interference of the laser field inside the film is found to play an important role at relatively lower fluence, which induces only thermal processes. The constructive interference at the front- and rear surfaces reduces the damage threshold. When the destructive interference occurs at the front surface, thermal damage inside the thin film with a thickness of 0.2–0.5 μm is dominant. The damage threshold with the photo-chemical process by bond-breaking at the rear surface is lower than that for the front surface when the thickness is smaller than 0.1 μm. Thus, the damaged area can change drastically due to interference of the laser field in the material. The interference effect can be seen to be  $\sim 1.5$  μm, which is much smaller than the penetration depth of silicon at 775 nm,  $\sim 10$  μm because of the two-photon absorption on the surface.

## Acknowledgments

The author thanks Dr. Prachi Venkat for her contribution. This research is supported by the MEXT Quantum Leap Flagship Program (MEXT Q-LEAP) under Grant No. JPMXS0118067246. This research is also partially supported by JST-CREST under Grant No. JP-MJCR16N5. The numerical calculations are carried out using the computer facilities of the SGI8600 at the Japan Atomic Energy Agency (JAEA).

## References

1. P. P. Pronko, P. A. VanRompay, C. Horvath, F. Loesel, T. Juhasz, X. Liu, and G. Mourou: “Avalanche ionization and dielectric breakdown in silicon with ultrafast laser pulses”, *Phys. Rev. B* **58**, 2387–2390 (1998).
2. J. Bonse, S. Baudach, J. Krüger, W. Kautek, and M. Lenzner: “Femtosecond laser ablation of silicon—modification thresholds and morphology”, *Appl. Phys. A* **74**(1), 19–25, (2002).
3. Yusaku Izawa, Yuichi Setuhara, Masaki Hashida, Masayuki Fujita, and Yasukazu Izawa: “Ablation and amorphization of crystalline Si by femtosecond and picosecond laser irradiation”, *Jpn. J. Appl. Phys.*, **45**(7), 5791–5794, (2006).
4. Paul Allenspacher, Bernd Huettner, and Wolfgang Riede: “Ultrashort pulse damage of Si and Ge semiconductors”, *International Society for Optics and Photonics, SPIE*, **4932**, 358 – 365, (2003).
5. L. Gallais, D.-B. Douti, M. Commandré, G. Batavičičūtė, E. Pupka, M. Ščiuka, L. Smalakys, V. Sirutkaitis, and A. Melninkaitis: “Wavelength dependence of femtosecond laser-induced damage threshold of optical materials”, *J. Appl. Phys.*, **117**(22), 223103 (2015).
6. P. Venkat and T. Otobe: “Three-temperature modeling of laser-induced damage process in silicon”, *Appl. Phys. Express*, **15**, 041008 (2022).
7. P. Venkat and T. Otobe: “Wavelength dependence of laser-induced excitation dynamics in silicon”, *Appl. Phys. A*, **128**(9), 810, (2022).
8. P. Venkat and T. Otobe: “Thickness Dependence of Laser Damage in silicon Thin Films”, *J. Laser Micro/Nano engineering* **18**, 196 (2023).

# Medical Applications of Composite Optical Fiberscopes

OKA Kiyoshi



Medical Laser Applications Project, Department of Quantum Applied Photonics

National Institutes for Quantum Science and Technology (QST) has developed a composite optical fiber that transmits high-energy laser light and images of the irradiated target on the same axis, allowing observation and welding in parallel to research on the maintenance and preservation of nuclear power and fusion reactors. Based on this technology, two types of the composite optical fiberscopes (COF) have been developed in this study, as shown in Fig.1, where a lens is attached to the tip of a composite optical fiber. A large-diameter optical fiber for transmitting high-energy lasers is at the center for heat treatment of the affected area, while optical fibers for image transmission are coaxially integrated around it for visual confirmation of the laser irradiation target. A “coaxial type” is defined as a structure in which the outer periphery of a transmission optical fiber is surrounded by several optical fibers that transmit illumination light. Conversely, a “two-axis type” is defined as one in which an optical fiber for image transmission and an optical fiber for laser transmission for irradiating a wide range of laser beams are arranged in parallel.

Currently, a minimally invasive laser treatment device based on this technology is under development, and plans are underway to expand its applications into the medical field.

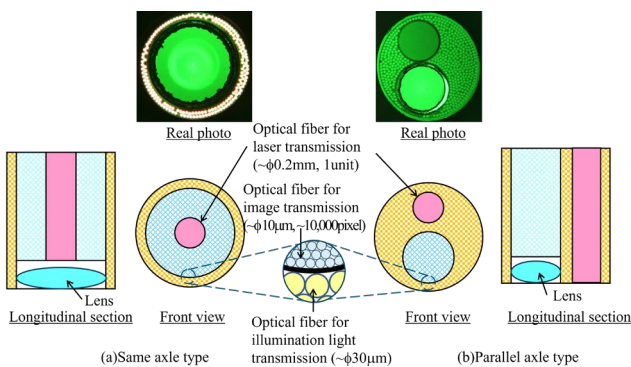


**Fig.1. Structure of the composite optical fiberscope (two types) capable of transmitting laser light and images in parallel**

The most active medical application currently under study involves the construction of testing and treatment equipment for peripheral lung cancer. The number of lung cancer patients around the world is increasing each year, and the number of patients in Japan including both men and women has exceeded 120,000 by 2021. The first choice of treatment for early-stage lung cancer is surgical resection, but photodynamic therapy (PDT), which is minimally invasive, safe, and highly effective, has become one of the standard treatment options. Additionally, PDT is an effective treatment for patients with decreased cardiopulmonary function, various high-risk patients, and the elderly. PDT is a treatment method that combines a tumor-loving photosensitizer and low-power laser irradiation. The intravenously administered photosensitizer accumulates in tumor

tissue and is excited by irradiating the tumor tissue with laser light. By utilizing the strong cell-destroying effect of singlet oxygen generated at that time, selective treatment of diseased areas with low-energy laser irradiation is possible without causing major damage to normal tissue. Currently, PDT performed via transbronchoscopy for early-stage central lung cancer is covered by insurance, and further demand is expected in the future. Conversely, PDT cannot be performed in the case of early-stage peripheral lung cancer due to the lack of endoscopes that can be inserted into the peripheral lung fields. Currently, no options for lung function-preserving treatment are available.

Therefore, a small peripheral lung cancer PDT device has been constructed by adopting a “two-axis type” design that parallels optical fibers for image and laser transmissions (Fig. 2). The device comprises an image observation device (camera), an image processor for fiber image improvement, an LED illumination light source, a semiconductor laser (wavelength:  $664 \pm 2$  nm, maximum output: 500 mW, CW), and a composite optical fiber scope (outer diameter: 1.02 mm, The number of pixels: 10,000, laser light guide diameter: 0.4 mm). Clinical research has been conducted using the designed device to obtain regulatory approval. The device has been applied to seven patients, and good results have been obtained [1].

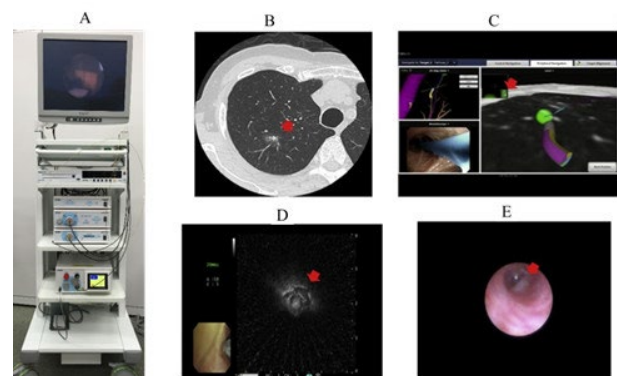


**Fig.2. A) Photodynamic therapy device, B) Chest computed tomography (CT) image showing the cancer lesion in rt S2. The tumor is visualized as a ground-glass opacity (GGO) with a solid component and measured 20 mm in diameter. C) Navigational bronchoscopy image using superDimension. The green ball represents the right upper nodule at rt S2 in the apical segment. The red arrow shows the alignment of the guide sheath with the target at a 2.8 cm distance. D) R-EBUS image of the tumor. The red arrow shows the tumor lesion. E) Image of the peripheral-type lung cancer lesion as visualized by the COF. The red arrow shows the tumor.**

During testing, when the fiberscope was inserted into the peripheral lung, the fiberscope was somewhat stiff and had issues with flexibility. Therefore, not all peripheral lung areas could be accessed. Particularly, the access to B1, B1+2 (pulmonary

branches), and B6 (upper and lower lobe branches) was difficult. Thus, the establishment of a COF that is flexible and easy to insert has become a new challenge.

Currently, the developed fiberscope uses quartz glass as the main material, which has excellent transparency but poor flexibility. Additionally, although the fiberscope coating can be made thinner, it is hard and can buckle when bent. Therefore, by reconsidering the material and structure of the fiberscope, a fiberscope that is easy to insert is developed in this study.

Specifically, flexibility can be achieved by using multi-component glass instead of quartz as the material for the optical fiber, although the transparency is poor. Similarly, for the laser transmission fiber, flexibility can be ensured and the laser irradiation range can be expanded, although the transmission efficiency gets reduced. Additionally, polyimide is commonly used as a material of the outer tube for fiberscopes, but on using Teflon, the durability reduces during long-term use; however, the flexibility of fiberscopes is enabled. Existing issues have been mitigated in this study by developing a new fiberscope.

Based on the aforementioned considerations, the newly developed fiberscope is shown in Fig. 3. The fiberscope (Laser-eYe ultra-thin fiberscope; LYU) has a total length of 1750 mm and an insertion length of 1400 mm. The maximum outer diameter of the insertable part is 0.97 mm. The LYU bundles 9,000 optical fibers for image transmission, one fiber of diameter 120  $\mu\text{m}$  for laser transmission, and  $\sim 300$  fibers of diameter 30  $\mu\text{m}$  for illumination. The aperture of the laser transmission fiber and illumination fiber is  $120^\circ$  (design value). Notably, the transmission efficiency of the laser is  $\sim 83\%$ . The material of the outer tube is an originally designed Teflon tube with a hydrophilic coating. The material is expected to offer ease of force for escape (slip) in the opposite direction when the tip of the fiberscope comes into contact with the lung wall. In addition, the base (hand) part of the covering is made harder to maintain flexibility and improve operability. The closer the fiber is to the tip, the softer the material. Thus, when the base portion of the fiberscope is rotated, force is easily transmitted to the distal end portion, which can be rotated in the same way as the base portion.

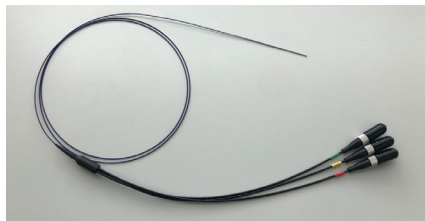


**Fig.3.** Newly developed composite optical fiberscope

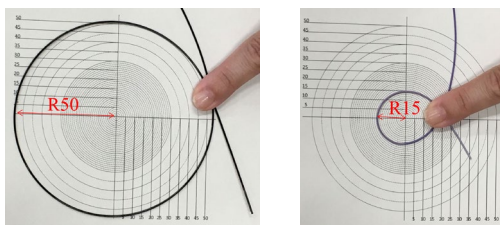


**Fig.4.** Flexibility evaluation of existing fiberscope (left) and newly developed LYU (right)

Figure 4 shows an image of flexibility comparison between the existing fiberscope and the newly developed LYU. The minimum bending radius for the conventional fiberscope is  $\sim 50$  mm, while that for the LYU is  $\sim 15$  mm.

To evaluate the applicability of LYU to PDD and PDT, fluorescence observation was performed using multi-functional porphyrin-phospholipid nanoparticles (Porphysomes) as photosensitizers that enabled fluorescence-induced photothermal therapy. Additionally, preclinical studies were conducted using rabbit and pig lungs. In a rabbit lung tumor model, fluorescence was detected in the peripheral lung region by combining an ultra-thin bronchoscope (BF type XP160F, Olympus Medical Systems) with LYU (Fig. 5).

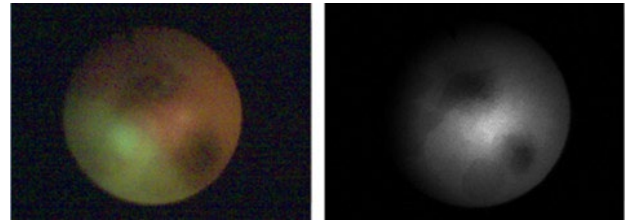


**Fig.5.** Normal light observation (left) and fluorescence observation with porphysome (right) by using LYU

Additionally, by combining a conventional bronchoscope (BF type MP160F, Olympus Medical Systems) with LYU and inserting it into the pig lung, the lumen of the 8th and 9th bronchus in the distal right lower lobe was accessed and observed, which is normally difficult. (Fig. 6). LYU passed through the working channels of both types of bronchoscopes without any difficulties. Thus, the observation of peripheral lung fields using normal light and fluorescence observation using laser light is possible using LYU, suggesting its effectiveness [2].

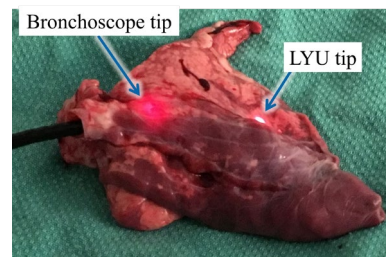


**Fig.6.** Access to the peripheral area of pig lung by combining bronchoscope and LYU

### Acknowledgments

Dr. T. Kinoshita and Dr. K. Yasufuku from UHN are thanked for the animal tests. Ms. S. Minakawa from OK Fiber Technology Co., Ltd. is thanked for manufacturing of experimental equipment.

### References

1. J. Usuda, T. Inoue, T. Tsuchida, K. Ohtani, S. Machara, N. Ikeda, Y. Ohsaki, T. Sasaki, K. Oka, *Photodiagnosis and Photodynamic Therapy*, 30 (2020) 101698.
2. T. Kinoshita, A. Effat, A. Gregor, T. Inage, T. Ishiwata, Y. Motooka, H. Ujiie, B. C. Wilson, G. Zheng, R. Weersink, H. Asamura, K. Yasufuku, *Chest*, 156 (2019), 571-578

# Advanced Photon Research Activities

HAJIMA Ryoichi

Department of Advanced Photon Research



The Department of Advanced Photon Research promotes the development of laser-driven quantum beam sources using high-intensity lasers and their applicational research to diverse fields. The organization of the department is shown in Fig. 1.

Laser Facility Operation Office provides operation and technical support for large laser equipment: a vehicle-mounted mobile laser system for non-destructive tunnel inspection, the 10-TW-class JLITE-X laser, and the petawatt-class J-KAREN-P laser.

The J-KAREN-P laser has world-class performance in terms of temporal (contrast performance) and spatial (focusing performance) qualities, which are important properties for user experiments. In the Advanced Laser Science Group, further improvements to the performance of the J-KAREN-P laser are under development. Focusing an ultra-intense laser can create high-density, high-temperature conditions and extremely high electromagnetic fields that cannot be achieved by other methods. Thus, the J-KAREN-P laser is being applied to extreme field science such as laser ion acceleration.

The High-field Science Research Group focuses on conducting research aimed at the cutting edge of high-intensity physics, including studies on laser wake-field acceleration for a compact free-electron laser, a plasma-based X-ray source to generate attosecond coherent X-ray pulses. The high-intensity field created by an ultra-intense laser is expected to destroy the vacuum. Through such phenomena, the mysteries of the universe are aimed for exploration.

In the LCS Gamma-ray Group, generation and applications of laser Compton scattered (LCS) gamma-ray beams are studied, which have unique properties of energy-tunable quasi-monoenergetic arbitrary polarization. The applications include studies of nuclear structure and non-destructive measurement of nuclides. The interaction of gamma rays with a nucleus in the universe to reveal the origin of elements in the solar system is another subject researched by the group. Additionally, advanced photon sources such as an attosecond X-ray source are being developed based on an infrared free-electron laser (FEL) oscillator.



Figure 1: Organization of the Department of Advanced Photon Research.

Research highlights for FY2023 are presented independently in this annual report. This section briefly describes results that are not included in the highlights.

Upgrade works continue on the J-KAREN-P petawatt laser facility to improve output performance and temporal quality. After wavefront correction using a deformable mirror, focusing with an f/1.3 off-axis parabolic mirror has delivered a peak intensity of  $10^{22}$  W/cm<sup>2</sup> at 0.3 PW power levels. For better temporal contrast, the origins of pre-pulses generated by post-pulses have been identified, and wedged optics have been applied to remove the post-pulses. For the complete elimination of the remaining pre-pulses, a cascaded femtosecond optical parametric amplifier based on the utilization of an idler pulse in place of a signal pulse has been developed. The order of magnitude enhancement of the pedestal before the main pulse has been obtained by using a higher surface quality convex mirror in the Öffner stretcher. With the help of a single plasma mirror, the contrast can be as high as  $\sim 10^{15}$  up to 40 ps before the main pulse [1].

The digital transformation (DX) for remote and automated operation of the J-KAREN-P laser facility is under development. In the laser room, a remote control and visualization system is being developed for the measurement of laser parameters such as laser profile images, the automatic start-up of the pump laser, and the automatic adjustment of the optical path of the main laser. In the target chamber room, a remote-control system is under development for the measurement of laser energy and laser spectrum delivered to the target chamber. The system supports an automated construction of a database comprising data for experimental users. Automatic inspection of large mirror damage and integrated monitoring of laser parameters by artificial intelligence (AI) image analysis is another important function implemented in the system. At the end of FY2023, a remote-control system to automatically start up the pumping lasers used in the J-KAREN-P has been fully developed. The system can automatically start all pumping lasers at specified daily schedules, increasing the J-KAREN-P laser supply time by 60 min/day. Thus, an increase of 36,000 shots at 10 Hz and 360 shots at 0.1 Hz has been recorded.

The interaction of high-intensity, ultrashort PW-class laser pulses with dense matter produces non-equilibrium plasma, where highly charged ions are generated via both collisional and tunnel ionization processes when the laser intensity exceeds  $10^{20}$  W/cm<sup>2</sup>. A clear distinction between the two ionization processes for the evolution of the charge state of the non-equilibrium plasma poses a challenge. The ionization processes can be distinguished in some cases by observing the X-ray spectral lines caused by the transition of an electron into the K-shell of highly charged ions. The time-dependent calculations of plasma kinetics have confirmed the possibility; for example, when sufficiently small cluster targets with low-density background gas are irradiated. The calculation results for Ar ions have been compared with those from the experiment at the J-KAREN-P laser facility [2].

The complex non-linear nature of the process of interaction between the laser and induced plasma remains an obstacle to the

widespread laser wakefield acceleration (LWFA) use as a stable and reliable particle sources. Generally, the best wavefront is a perfect Gaussian distribution. However, the consideration is not true experimentally, and more complicated distributions can potentially provide better results. An experimental study on the effects of tuning the laser wavefront via the controlled introduction of aberrations using the shock injection configuration has been conducted. The experiments by our department suggested a clear unique correlation between the generated beam transverse characteristics and the different input wavefronts. The electron beam stability during acceleration and injection is observed to be significantly different. In our case, the best beams were generated with a specific complex wavefront. A greater understanding of electron generation as a function of the laser input was achieved due to the aforementioned method and a higher level of control on electron beams by LWFA is foreseen [3].

Supersonic gas jets generated via a conical nozzle are widely applied in the laser wakefield acceleration of electrons. The stability of the gas jet is critical to the electron injection and the reproducibility of the wakefield acceleration. We investigated the role of the stilling chamber in a modified converging–diverging nozzle to dissipate the turbulence and stabilize the gas jets. By fluid dynamics simulations and the Mach–Zehnder interferometer measurements, the instability originating from the non-linear turbulence was studied, and the mechanism to suppress instability was proposed. Both the numerical and experimental results proved that the carefully designed nozzle with a stilling chamber can reduce the perturbation by more than 10 % compared with a simple-conical nozzle [4].

Special relativity can predict the frequency upshift of an electromagnetic wave reflected by a mirror approaching at a relativistic speed. We analyzed the reflection of an electromagnetic wave by a luminal mirror, “luminal plasma–vacuum interface or plasma slab” produced by an intense laser. When the mirror velocity gets closer to the speed of light in vacuum, the reflected wave frequency tends to infinity, and the mirror reflectivity vanishes, because in its proper reference frame, the incident electromagnetic wave frequency also tends to infinity, rendering any matter transparent. Conversely, the refractive index modulation in the mirror’s bulk can be independent of the mirror–vacuum interface position, at least during some time interval. Our analysis revealed that when a refractive index modulation of dispersive medium moves at the speed of light in vacuum, an incident electromagnetic wave, depending on its frequency, is either transmitted totally with a modified phase, forms a standing wave, or is reflected totally with an upshifted frequency. The luminal mirror converts a short incident pulse into a wave packet with an infinitely growing in-time local frequency near the interface and with an energy spectral density that asymptotically is the inverse square of the frequency. If the modulation disappears, the high-frequency radiation is released [5].

The study of nuclear structure utilizing nuclear resonance fluorescence (NRF) is one of the applications of laser Compton scattering, which enables the production of energy-tunable quasi-monoenergetic linearly-polarized gamma-ray beams at MeV energy regions. We conducted an NRF measurement to reveal the structure of low-lying dipole states in the singly closed-shell nucleus  $^{58}\text{Ni}$ . The experiment was conducted at the NewSUBARU synchrotron radiation facility at the University of Hyogo. The parity quantum numbers of the dipole states were determined by the intensity asymmetry of resonantly scattered gamma rays relative to the polarization plane of the incident photon beam. The electric and magnetic dipole ( $E1$  and  $M1$ ) strengths at excitation energies between 5.9 and 9.8 MeV were obtained based on dipole strengths taken from the literature. The  $E1$  and  $M1$  strength distributions were compared with large-scale

shell-model predictions [6].

The generation of optical vortices is an interesting research subject not only in the field of lasers but also in the universe. We formulated a theoretical approach to describe photon vortex production in synchrotron/cyclotron radiation from a helical moving electron under a uniform magnetic field in the relativistic quantum framework. The wave function of photons generated from synchrotron radiation was found to be the eigenstate of the  $z$  component of the total angular momentum ( $z\text{TAM}$ ) when the magnetic field was parallel to the  $z$ -axis. The approximation is applicable for photon vortex production of several tens  $\hbar$  of  $z\text{TAM}$ . Furthermore, we numerically calculated the energy spectra and spatial distribution of photon vortices in magnetic field strengths of 10 and 20 T using electrons with energies of 150 MeV and 8 GeV and Larmor radii of 10 and 100  $\mu\text{m}$  for the helical motion. The results indicate the production possibility of predominant photon vortices with a fixed  $z\text{TAM}$  when the energy and entrance trajectory of electrons and the structure of a magnetic field are controlled [7].

Notably, a free-electron laser (FEL) can be operated in the superradiant regime, where the radiation power is proportional to the square of the number of electrons, and the pulse width is inversely proportional to the number of electrons. In our study, the detailed structure of superradiant pulses generated from an FEL oscillator is experimentally revealed for the first time. The temporal waveform of an FEL pulse including its phase variation is reconstructed with a combination of linear and non-linear autocorrelation measurements. The waveform exhibits the features of a superradiant pulse, the main pulse is followed by a train of sub-pulses with  $\pi$ -phase jumps, reflecting the physics of light-matter resonant interaction. From numerical simulations, the train of sub-pulses is found to originate from repeated formation and deformation of electron micro-bunches accompanied by a temporal slippage of the electrons and light field, a process quite different from coherent many-body Rabi oscillations observed in superradiance from atomic systems. The revealed feature of the superradiant pulse generation in FEL oscillators provides useful information for the development of attosecond X-ray sources based on infrared FEL oscillators [8].

## References

1. H. Kiriya, Y. Miyasaka, A. Kon, M. Nishiuchi, A. Sagisaka, H. Sasao, A.S. Pirozhkov, Y. Fukuda, K. Ogura, K. Kondo, et al., “Laser Output Performance and Temporal Quality Enhancement at the J-KAREN-P Petawatt Laser Facility”, *Photonics* **10**, 997 (2023).
2. I.Y. Skobelev, S.N. Ryazantsev, R.K. Kulikov, et al., “The Role of Collision Ionization of K-Shell Ions in Nonequilibrium Plasmas Produced by the Action of Super Strong, Ultrashort PW-Class Laser Pulses on Micron-Scale Argon Clusters with Intensity up to  $5 \times 10^{21} \text{ W/cm}^2$ ”, *Photonics* **10**, 1250 (2023).
3. E.D. Oumbarek, A. Rondepierre, A. Zhidkov, et al. “Notable improvements on LWFA through precise laser wavefront tuning”, *Sci. Rep.* **13**, 18466 (2023).
4. Z.-Z. Lei, Y.-J. Gu, Z. Jin, et al. “Supersonic gas jet stabilization in laser–plasma acceleration”, *High Power Laser Sci. Eng.* **2023**, 11, e91 (2023).
5. T.Z. Esirkepov and S.V. Bulanov, “Luminal mirror”, *Phys. Rev. E* **109**, L023202 (2024).
6. T. Shizuma, M. Omer, T. Hayakawa, et al., “Parity assignment for low-lying dipole states in  $^{58}\text{Ni}$ ”, *Phys. Rev. C* **109**, 014302 (2024).
7. T. Maruyama, T. Hayakawa, R. Hajima, T. Kajino, and M.-K. Cheoun, *Phys. Rev. Research* **5**, 043289 (2023).
8. H. Zen, R. Hajima, and H. Ohgaki, “Full characterization of superradiant pulses generated from a free-electron laser oscillator”, *Sci. Rep.* **13**, 6350 (2023).

# Development of an X-ray Diagnostic Method for High-Density Plasmas for Optimizing Laser-Driven Heavy Ion Acceleration



Chang LIU

Advanced Laser Science Group, Department of Advanced Photon Research

Laser-driven heavy ion acceleration has emerged as a rapidly advancing field with the potential to revolutionize cancer treatment applications including nuclear physics and particle physics [1-5]. The scheme can provide an extraordinarily high acceleration field gradient [6]. Due to its unique characteristics, the laser-driven acceleration field can generate highly charged ions, even for high-Z elements, which is generally challenging for ion sources in conventional accelerators. The laser-driven ion acceleration scheme in principle can achieve higher energy and charge states within a very compact space than traditional accelerators, provided it is optimized and matured.

Using short-pulse high-contrast laser pulses interacting with solid-density heavy ion targets is a promising method to achieve high charge states and high energy heavy ions. The target material can be heated to a high temperature while maintaining a high density. To efficiently deposit the laser energy into the plasma, heating needs to be faster than radiative cooling; thus, short-pulse high-contrast lasers are required. Collisional ionization in target bulk contributes to the generation of highly charged heavy ions through return currents, and simultaneously, the produced highly charged heavy ions can be accelerated to high energies by the strong sheath field produced at the back side of the target. In our previous experiment, highly charged (up to  $Z = 45$ ) high energy ( $>20$  MeV/u) silver ions with atomic number 47 have been generated [7], indicating the existence of  $\sim 10$  keV temperature plasma. However, the temperature cannot be directly measured experimentally, and direct measurement can help improve our understanding and future optimization of the plasma and generated beams.

To diagnose gold plasma in laser-ion acceleration experiments, we focus on the gold M-shell spectral range (2500-3000 eV), to enable the diagnosis of plasma properties based on the characteristic lines. The X-ray spectrometer is designed with an elliptical configuration. A germanium (Ge,  $2d = 0.653$  nm, where  $d$  is the interplanar distance) reflective-type crystal produced by Saint-Gobain, having high X-ray reflectivity ( $R \approx 95\%$ , measured in 2000–4000 eV), with a central Bragg angle ( $\theta$ ) of  $45^\circ$  is selected. The germanium crystal is an arc segment of  $\sim 130$  mm in length along the ellipse, allowing observation of light within the Bragg angles of  $30^\circ$ – $60^\circ$ . The ellipse has an eccentricity of  $e = 0.96$ , with major and minor axes of  $a = 832$  mm and  $b = 237$  mm, respectively. The target is positioned at one of the foci of the ellipse, with a distance  $p = 1680(\pm 20)$  mm away from the crystal. The other focus is  $q = 120(\pm 2)$  mm away from the crystal and  $r = 80(\pm 2)$  mm away from the CCD surface (Fig.1(a)). Combined with an Andor DX440 CCD (512 $\times$ 2048 pixels, pixel size =  $13.5 \mu\text{m}$ ), the actual observable range is  $\sim 2500$ – $3000$  eV.

A calibration experiment was performed using the J-KAREN-P laser with a  $\approx 10$  J,  $\approx 45$  femtosecond (fs) full width at half maximum (FWHM), and a central wavelength of 800 nm. The laser pulses were focused using an  $f/1.4$  off-axis parabola (OAP) to a spot size of  $\approx 1.5 \mu\text{m}$  diameter (FWHM), resulting in

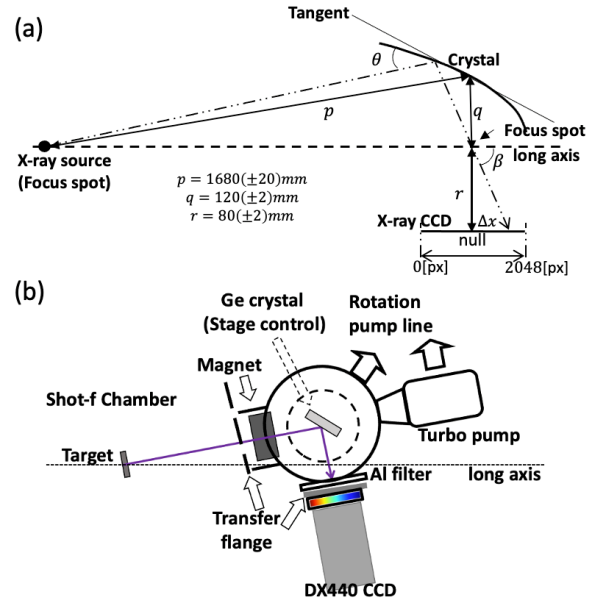


Figure 1: Schematic of the elliptical X-ray crystal spectrometer.

a maximum peak intensity of  $\sim 10^{21}$  W/cm $^2$ . The spectrometer setup is shown in Fig.1(b).

A polyvinylidene chloride (PVDC,  $(\text{C}_2\text{H}_2\text{Cl}_2)_n$ ) target (Saran manufactured by Mitsubishi Plastics) of thickness  $\sim 10 \mu\text{m}$  was used. All observable lines in the spectrometer observation window are shown in Fig. 2 [8], wherein the typical data obtained with the PVDC targets, including the raw CCD image (Fig.2(a)) and the lineout of the whole region after background subtraction (Fig.2(b)) are shown. The background is taken from a blank shot. The horizontal axis represents the pixel (px) number, while the vertical axis represents the raw CCD counts [cnt] before deconvolution. The characteristic lines of chlorine of  $K\alpha$  (2622 eV) and  $K\beta$  (2812 eV) were selected for the energy-to-pixel calibration of the spectrometer owing to its definite wavelength and relatively high intensity [9,10]. Each line was fitted with a Gaussian model for the determination of center pixel position (peak) and width (FWHM), as shown in the table of Fig.2, where the error corresponded to the  $1-\sigma$  fitting error.

When X-rays are reflected by an elliptical diffraction crystal, they follow Bragg's law of diffraction [11]  $n\lambda = 2d\sin\theta$ , where  $n$  represents the diffraction order and  $\lambda$  is the wavelength of the incident beam (where the relation between the spectral energy ( $E$ );  $\lambda$  can be connected with  $E[\text{eV}] \approx 1240/\lambda[\text{nm}]$ ) [12]. According to the geometrical relationship, the detecting angle  $\beta$  is introduced as shown in Fig. 1(a), such that  $\beta = \theta +$

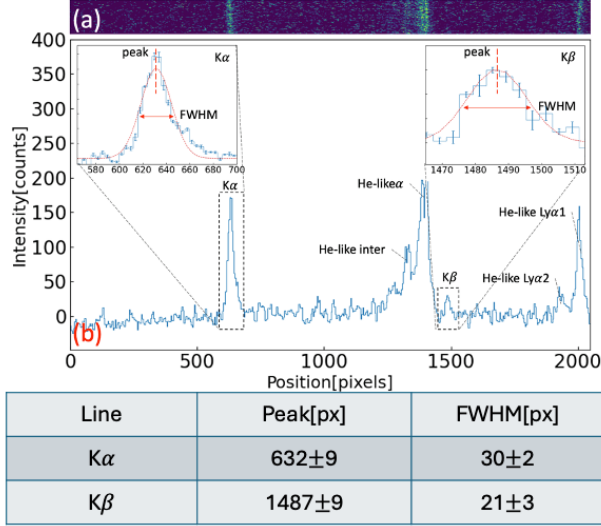


Figure 2: Raw X-ray data and profile line out for the PVDC target.

$\arccos\left(\frac{\cos\theta}{e}\right)$ . For first-order diffraction, we have  $\lambda/2d = (1 - e\cos\beta)/\sqrt{1 - 2e\cos\beta + e^2}$ . As shown in Fig. 1(a), the central null point on the CCD plane is defined as the point where a photon reflected at the geometrical center of the crystal reaches  $\Delta x$  [px], which is the distance from the null point in a horizontal plane. Due to the error caused by the relative position of the crystal and CCD, the null point has a slight offset  $\Delta s$  [px]. The value of  $\Delta s$  is determined by the least square fit with the peak value given in the table of Fig. 2.

$$\lambda = 2d\left(1 - e \frac{\Delta x}{\sqrt{r^2 + (\Delta x + \Delta s)^2}}\right) / \sqrt{1 - 2e \frac{\Delta x}{\sqrt{r^2 + (\Delta x + \Delta s)^2}} + e^2}$$

The value of  $\Delta s$  is obtained as  $\Delta s = -347 \pm 2$  [px].

The resolution power of the spectrometer is defined as [10]  $R = \lambda/\Delta\lambda$  (Eq.6), where  $\Delta\lambda$  represents the spectral line width. In principle, the line width can be expressed as [13-15]  $\Delta\lambda = \omega_d/rD$  (Eq.7), where  $\omega_d$  represents the finite resolution caused by the system, including imperfection of the crystal, finite size of the CCD pixels, and geometric errors.  $D$  represents the angular dispersion of  $d\beta/d\lambda$ . For the elliptical geometry,  $D$  is defined as [14]

$$D = (1 - 2e\cos\beta + e^2)^{3/2}/2de^2(e - \cos\beta)\sin\beta$$

To calculate the resolution power of the detector at any given wavelength, Eqs. (6-8) are combined and a least-squares fitting is performed. During the fitting,  $\omega_d$  is set as a free parameter and the FWHM values of the Kα and Kβ lines are utilized as  $\Delta\lambda$ , as shown in Fig. 2 table, giving a best-fit value of  $\omega_d = 0.29 \pm 0.01$  [nm]. The best fit curve for the resolution power  $R$  of the spectrometer is obtained as  $R = 275.96(\pm 7)\lambda D$ . The resolution powers of Kα and Kβ are  $524 \pm 9$  and  $562 \pm 26$ , respectively. Considering the CCD parameters, the true spectral line intensities  $I$  [photons/px/s] are deconvoluted as [17]:

$$I = CK/\eta\tau T_\lambda Q_\lambda \Gamma$$

where  $C$  is the CCD counts,  $K$  is the gain constant (0.7 [e/cnts]),

$\eta$  is quantum yield ( $E[\text{eV}]/3.66[\text{eV}]$ )[17],  $\tau$  is the exposure time (0.1 seconds),  $T_\lambda$  is the Al filter transmission,  $Q_\lambda$  is the CCD quantum efficiency (QE), and  $\Gamma$  is the crystal reflectivity.

In summary, we successfully developed and calibrated a high-resolution elliptical-geometry reflective crystal X-ray spectrometer. In our spectral observation range of 2500–3000 eV, the resolution power of the spectrometer lies between 500 and 600, corresponding to a spectral line width of  $\sim 5$  eV in photon energy. The range mainly covers the 3p-4d and 3d-4f transitions of cobalt, nickel, copper, and zinc-like Au ions [18]. Consequently, the spectrometer has the capability of measuring and resolving the Au Ni-like 3d-4f, and Co-like 3p-4d spectral lines at 2515–2877 eV [19-23]. Therefore, the spectrometer is highly suitable for diagnosing high-temperature high-density heavy ion plasmas in conditions amenable to the generation of highly charged high-energy heavy ions. Combining these measurements with comprehensive X-ray multi-band observations can enhance the reliability of measured plasma parameters in the future.

## Acknowledgments

We gratefully acknowledge the J-KAREN-P operation team for their experiment support. This work was partially supported by KAKENHI Grant No. 20H00140, Grant No. 21KK0049, Grant No. 22H00121, QST President's Strategic Grant (QST International Research Initiative (AAA98) and Creative Research (ABACS)).

## References

1. Daido H, et al. Reports on progress in physics 75.5 (2012).
2. Macchi A, et al. Reviews of Modern Physics 85.2 (2013).
3. Borghesi M, et al. Physics of Plasmas 9.5 (2002).
4. Barberio M, et al. Nature communications 9.1 (2018).
5. Kroll F, et al. Nature Physics, 18.3(2022).
6. Dover N P, et al. Light: Science & Applications, 12.1(2023).
7. Nishiuchi M, et al. Physical Review Research, 2.3(2020).
8. Spectr-w3 database on spectroscopic properties of atoms and ions, 2023.
9. Cowan R D. Univ of California Press, 1981.
10. Agarwal B K. Springer, 2013.
11. Bragg W H, et al. Proceedings of the Royal Society of London. Series A, 88.605(1913).
12. Planck M. Ann. Physik, 1900, 1: 719-721.
13. Shvyd'ko Y, et al. Physical Review A, 87.4(2013).
14. Amboage M, et al. Nuclear Instruments and Methods in Physics Research Section A, 621.1-3 (2010).
15. Inubushi Y, et al. Physical Review Letters, 109.14(2012).
16. Henke B L, et al. Atomic data and nuclear data tables, 54.2(1993).
17. Haugh M, et al. Lawrence Livermore National Lab. (LLNL), Livermore, CA (United States), (2008).
18. Busquet M, et al. Physica Scripta, 31.2(1985).
19. Matthews D L, et al. Journal of applied physics, 54.8(1983).
20. Bauche-Arnoult C, et al. Physical Review A, 33.1(1986).
21. Tragin N, et al. Physica Scripta, 37.1(1988).
22. Elliott S, et al. Physical Review A, 47.2(1993).
23. Honda K, et al. Physical Review E, 55.4(1997).

# Energetic ion acceleration by irradiating large-area suspended graphene with J-KAREN-P laser for the realization of over 200 MeV protons



MINAMI Takumi

Advanced Laser Science Group, Department of Advanced Photon Research

Irradiating an intense laser on a matter can excite a quasistatic electric field to accelerate energetic ions. The strength of the acceleration field reaches  $10^{12} \text{ Vm}^{-1}$ , which is several orders of magnitude larger than that in conventional accelerators [1]. Therefore, laser ion acceleration is expected to act as a compact ion source suitable for several applications including cancer therapy, nuclear physics, and laboratory astrophysics. Generating over 200 MeV protons is pivotal to such applications; however, no experimental result has demonstrated such high energies [2]. In experiments, thin foils are often used as a target because it is easy to control thickness, materials, and surface structures. Target normal sheath acceleration (TNSA) is one of the well-investigated acceleration mechanisms, where acceleration occurs at a sheath field excited between the laser-accelerated electrons and the rear surface of the charged-up target. In another mechanism, radiation pressure acceleration (RPA), ion acceleration occurs at the front of the propagating laser pulse inside and behind the target, resulting in higher acceleration efficiency than TNSA [3]. However, RPA requires nanometer-scale thin targets. Such targets are easily broken or perturbed by the heating of laser pre-pulses, which disturb the efficient energy transfer to ions. A plasma mirror (PM) is a method to decrease the fluence of the pre-pulses. However, the installation of PM requires a large change in experimental setups and is preferably avoided, especially in small facilities with no spaces for installation.

Graphene is an extremely strong material, although its thickness is as thin as an atom [4]. Additionally, it is transparent and has high electrical and thermal conductivities [5]. In this study, a technique to suspend single to multi-layer graphene on a large hole is developed to irradiate free-standing graphene surface with intense lasers, as shown in Fig. 1 (a). The graphene is named large-area suspended graphene (LSG) [6]. Figure 1 (b) shows the thickness measurement result of single-layer LSG obtained using atomic force microscopy (AFM). As single-layer LSG has a thickness of 1 nm, the target thickness can be controlled at the order of 1 nm.

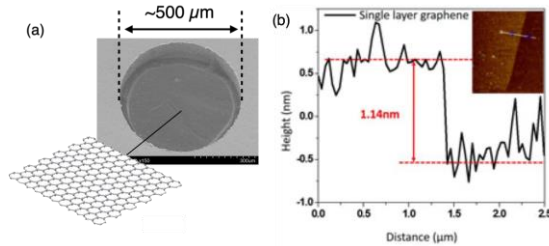


Figure 1. (a) Microscopic image of single-layer large-area suspended graphene (LSG) on a 500  $\mu\text{m}$  diameter hole. (b) Thickness measurement of single-layer LSG using an atomic force microscope, resulting in 1 nm thickness per layer [6].

Figure 2 (a) shows the estimation of the optimum number of LSG layers to the laser intensity. The estimation is based on the condition for RPA to dominate the acceleration over TNSA [7]. The lower limit of the number of layers (blue line) is derived from the pressure balance between the plasma space charge and the laser to satisfy the requirement for avoiding completely blowing out electrons. Above the upper limit (orange line), the expected energy of ions from the TNSA model is larger than the one from the RPA. For a laser intensity of  $5 \times 10^{21} \text{ Wcm}^{-2}$ , the optimum thickness is estimated from 40 to 150 layers.

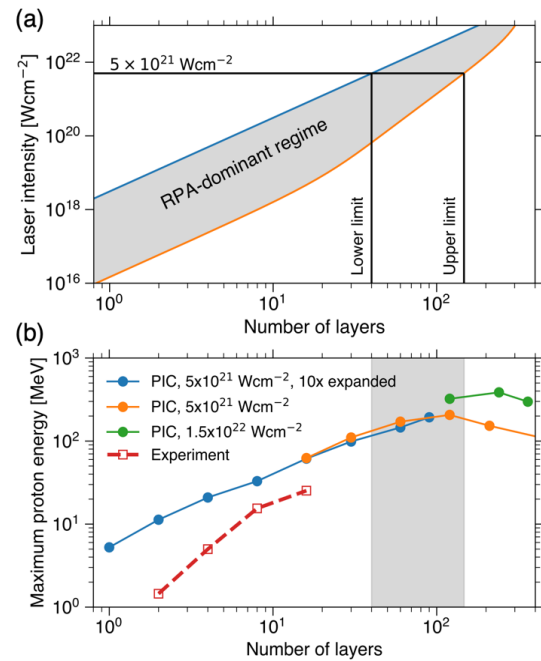


Figure 2. (a) Relation of the number of LSG layers and laser intensity for RPA to dominate the acceleration [5]. (b) Maximum proton energy dependences on the number of LSG layers in the PIC with expanded targets and the laser intensity of  $5 \times 10^{21} \text{ Wcm}^{-2}$  (blue), PIC with  $5 \times 10^{21} \text{ Wcm}^{-2}$  (orange), PIC with  $1.5 \times 10^{22} \text{ Wcm}^{-2}$  (green), and the experiment shown in Fig.3 (red-dashed) [9, 10]. The shaded region indicates the optimum thickness for  $5 \times 10^{21} \text{ Wcm}^{-2}$ .

Based on the estimation, simulations are performed with a two-dimensional particle-in-cell (PIC) code, EPOCH-2D. Figure 2 (b) shows the maximum proton energies in terms of the number of layers of LSG. The laser parameters are set to be the same as the main pulse of the J-KAREN-P laser [8], namely the wavelength of  $0.81 \mu\text{m}$ , the pulse duration of 40 fs, the spot diameter of  $2 \mu\text{m}$ , and the peak intensity of  $5 \times 10^{21} \text{ Wcm}^{-2}$ . In the simulations, an ionized plasma with the same composition ratio

of proton and full-stripped carbon ions as that in a previous study [9] is set initially; therefore, no graphene structures are considered. To simulate the few-nm thick LSG targets, the nm-scale structures are divided into grids, whereas several tens of  $\mu\text{m}$  regions are required to calculate the ion acceleration. Such a consideration is impractical; therefore, ten times thicker targets with ten times lower densities are set, corresponding to the assumed pre-expansion of the targets because of heating by laser pre-pulse for the extremely thin target regime, represented by the blue line. For the moderately thin LSG regime, the LSG targets are simulated without assuming the pre-expansion, represented by the orange line. No discrepancies between the blue and orange lines are observed; therefore, the pre-expansion is confirmed to not affect the maximum proton energies. The proton energies show a peak energy of 206 MeV at the 120-layer, consistent with the prediction in Fig.2 (a). Furthermore, cases with a higher intensity laser of  $1.5 \times 10^{22} \text{ Wcm}^{-2}$  are simulated by assuming the upgrade of the J-KAREN-P laser, represented by the green line. As expected from Fig.2 (a), a higher energy of protons is expected with higher intensity. In this condition, the PIC simulations predict the maximum proton energy of  $\sim 400$  MeV with 240-layer LSG [10].

As aforementioned, thinner targets are easily broken by the laser pre-pulses, and no experimental report shows energetic ion accelerations without a PM in the extremely thin target regime. To demonstrate the durability of graphene, a series of experiments is conducted by irradiating the thinnest targets with the J-KAREN-P laser without a PM [9, 10]. Figure 3 (a) shows the experimental setup.

The J-KAREN-P laser with a wavelength of  $\sim 0.81 \mu\text{m}$  and a pulse duration of  $\sim 40$  fs was focused in a  $\sim 2 \mu\text{m}$  diameter spot with an  $f/1.3$  off-axis PM. The transferred energy on the target was  $\sim 10$  J, resulting in an intensity of  $\sim 5 \times 10^{21} \text{ Wcm}^{-2}$  [8]. The incident angle on the target was  $10^\circ$  from the optical axis. To diagnose the accelerated ions, the Thomson parabola spectrometer (TPS) was placed on the optical axis  $\sim 1$  m away from the target. Figure 3 (b) shows the observed energy distribution functions for protons in the laser shots with 2, 4, 8, and 16-layer LSG targets, corresponding 2, 4, 8, and 16 nm thicknesses. MeV-scale proton accelerations were realized without a PM by irradiating the thinnest target ever [9]. Using other types of nm-scale targets than LSG, MeV-scale protons have been observed only with PMs in experiments [13]. Thus, the high thermal conductivity and transparency of graphene are considered important factors in understanding its pre-pulse resistance; experiments for confirmation are for a future study.

As shown in Fig. 2 (a), 2-16 layer LSG targets are too thin to efficiently accelerate ions by RPA. In Fig. 2 (b), the maximum proton energies for each LSG layer in the experiment are shown with the red dashed line. The simulation and experimental results show higher proton energies with thicker LSG at the thickness regime. Since the PIC simulations are performed with ideal conditions without pre-pulse, PIC simulations overestimate the proton energy compared to the experimental results. The deviations between the PIC and experimental results are larger for thinner targets. The results tend to approach a factor two discrepancy as the target becomes thicker. Thus, extremely high-energy protons are expected to be generated without a PM by optimizing the LSG targets to the laser conditions. In addition, even when factor two from the numerical results is considered, the proton acceleration is expected at  $\sim 200$  MeV even without a PM with three times more intense J-KAREN-P laser. Notably, even LSG is assumed to be ionized by pre-pulse heating. Using a PM is expected to improve the situation and increase the accelerated ion energies, especially in the extremely thin regime with only a few layers of LSG.

To realize such high-energy proton accelerations, the

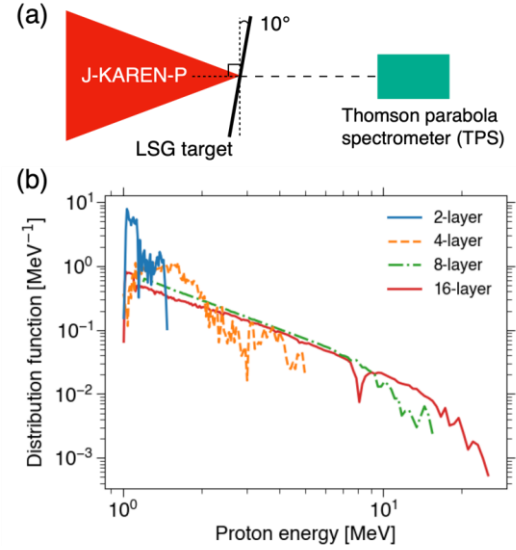


Figure 3. (a) Experimental setup for laser ion acceleration with J-KAREN-P laser and large-area suspended graphene (LSG) targets. (b) Proton distribution functions obtained with Thomson parabola spectrometer (TPS) for 2, 4, 8, and 16-layered LSG target shots [9, 10].

optimization of ion diagnostics is important. TPS is not enough to diagnose the expected high-energy protons owing to its low resolutions for such high-energy protons. In this situation, the two types of diagnostic methods developed are expected to play important roles: one involves machine-learning-implemented analyses of solid-state nuclear track detectors [11], while the other includes a multi-stage scintillation detector [12].

In summary, laser ion acceleration is investigated with large-area suspended graphene (LSG) targets. The experiment realizes MeV-scale proton accelerations without PM using the thinnest target ever. Optimization of LSG to the laser predicts the generation of  $\sim 200$  MeV protons without a PM with conditions assuming the upgrade of J-KAREN-P.

## Acknowledgments

The author would like to thank the technical support provided by the staff of J-KAREN-P at QST-KPSI. The author also would like to thank H. Kiriyama, Y. Fukuda, W.Y. Woon, and Y. Kuramitsu for the project management. The author also would like to thank C.M. Chu and Y.T. Liao for the LSG fabrications. The author also would like to thank the co-authors of the reference [9-13].

## References

1. H. Daido et al., Rep. Prog. Phys. **75**, 056401 (2012)
2. Y. Takagi et al., Phys. Rev. Res. **3**, 043140 (2021)
3. S. Kar et al., Phys. Rev. Lett. **109**, 18 (2012)
4. Y. Liao et al., Nanoscale **14**, 1, 42 (2022)
5. A. Geim, Rev. Mod. Phys. **83**, 3, 851 (2011), A. Balandin, Nat. Mater. **10**, 8, 569 (2011)
6. N. Khasanah et al., High Power Laser Sci. Eng. **5**, e18 (2021)
7. B. Qiao et al., Phys. Rev. Lett. **108**, 115002 (2012)
8. H. Kiriyama et al., High Power Laser Sci. Eng. **9**, e62 (2021)
9. Y. Kuramitsu, T. Minami et al., Sci. Rep. **12**, 1, 2346 (2022)
10. T. Minami et al., submitted to High Energy Density Phys.
11. T. Taguchi et al., Rev. Sci. Instrum. **95**, 033301 (2024).
12. T. Minami et al., Rev. Sci. Instrum. **93**, 113530 (2022), Y. Abe et al., Rev. Sci. Instrum. **93**, 063502 (2022)
13. Flacco et al., Phys. Rev. E **81**, 036405 (2010)

# Numerical study on electro-optical sampling of transition radiation from laser wake-field electrons

Kai HUANG



High Field Science Research Group, Department of Advanced Photon Research

Laser wake-field acceleration (LWFA) [1], with the inherent ultrashort timescale and ultrahigh acceleration gradient, has attracted great interest globally. Electron plasma waves with a wavelength of a few tens of micrometers ( $\mu\text{m}$ ) can be generated via the incidence of a high-power femtosecond (fs) laser beam on an under-dense plasma. Trapped electrons achieve energies of over GeV within a centimeter [2].

In the study of LWFA, the generation and application of secondary X-ray sources are of significant importance. The timing and duration of the electron bunches affect the temporal resolutions of pump-probe applications. The three-dimensional (3D) density of the electron bunch partially determines the peak fluence of the X-rays. For the investigation and optimization of high-brightness electron bunches from LWFA, the development of a single-shot monitor capable of measuring the transverse and longitudinal profile of a high-energy electron bunch is important.

Electro-optic (EO) sampling has been applied to accelerator studies for the measurement of temporal information of high-energy electron bunches [3]. Pioneering numerical studies have been reviewed in a previous study [4]. For monitoring of the electron emission timing, “EO spatial decoding technique” has been introduced into LWFA in our previous studies [5-8].

EO sampling of transition radiation (TR) from an electron bunch has been conducted to measure the relative electron longitudinal profile or the field strength of a terahertz pulse [9-11]. However, simultaneous measurement of absolute current and transverse profiles has not been attempted. By performing EO spatial decoding on the TR field, the electron bunch profiles can be measured both temporally and spatially. The detection method has been named as “TR-EO” method in this study.

The numerical investigations concentrate on EO spatial decoding of TR generated by a relativistic electron bunch traversing a metal foil [12]. The computations involve the imaging of polychromatic transition radiation emitted by the electron bunch and EO spatial decoding process. From an experimental standpoint, a meticulous examination of the calculation methodology for data analysis is crucial. Thus, to comprehensively grasp the signal generation process and explore the feasibility of employing a less time-intensive approach, comparative analyses on detailed and simplified models are conducted in this study for both transition radiation imaging and EO signal generation.

Regarding TR imaging, the findings indicate that the simplified analytical model is adequate for conducting polychromatic calculations with significant accuracy. Concerning EO spatial decoding, the EO signal generation process is investigated using one and two-dimensional (1D and 2D) models. The observations of this study reveal that the 1D model suffices for swift data analysis. Moreover, temporal energy chirp is demonstrated to minimally affect the shapes of EO signals. A part of the results is reported in this paper.

The concept of the numerical study is depicted in Fig. 1. For LWFA, a drive laser beam is directed onto a gas target to generate an electron beam. However, the outgoing drive laser can cause

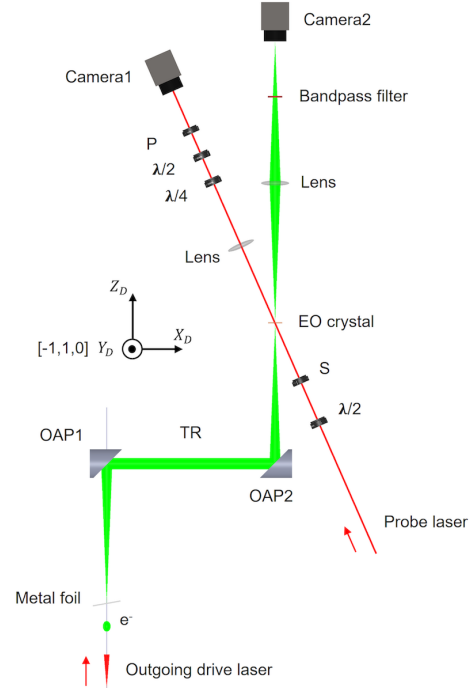


Fig. 1 Conceptual scenario of the TR-EO spatial decoding set-up for LWFA. e<sup>-</sup>: electron bunch; OAP: Off-axis-parabolic gold mirror; S: polarizer before EO crystal; P: polarizer after EO crystal;  $\lambda/2$ : half waveplate;  $\lambda/4$ : quarter waveplate; and BP: bandpass filter. The inset shows the coordinates of the imaging plate. The  $[-1, 1, 0]$  axis of the crystal is along the  $Y_D$  direction. The polarization of the incident probe laser is also parallel to the  $Y_D$  direction. ( $X_D$ ,  $Y_D$ ) denote the coordinates in the detection plane (EO crystal).

damage and produce noise during particle parameter detection. Thus, a metal foil (such as aluminum or stainless steel) is positioned in the path of the electron beam to mitigate noise generated by the drive laser beam and TR, as illustrated in Fig. 1. Subsequently, the emitted TR is imaged using two off-axis parabolic (OAP) mirrors and directed onto an EO crystal, typically one with a zinc-blende structure. Spatial decoding is performed using an ultrashort probe laser beam with a small incident angle  $\theta_p$  to the EO crystal. The  $[-1, 1, 0]$  axis of the crystal aligns with the polarization direction of the probe laser and is orthogonal to the plane formed by the probe laser beam and the TR propagation direction. Half-wave and quarter-wave plates are inserted to enable near-cross-polarization detection [4]. Then, the TR passing through the crystal is imaged again to measure the optical transition radiation (OTR). Since the TR field covers a wavelength range from visible to infrared, it is advisable to place

the EO crystal inside a vacuum chamber to prevent unwanted absorption from the vacuum window and air. Similarly, a gold-coated OAP is utilized instead of a lens to transmit TR for the aforementioned reason.

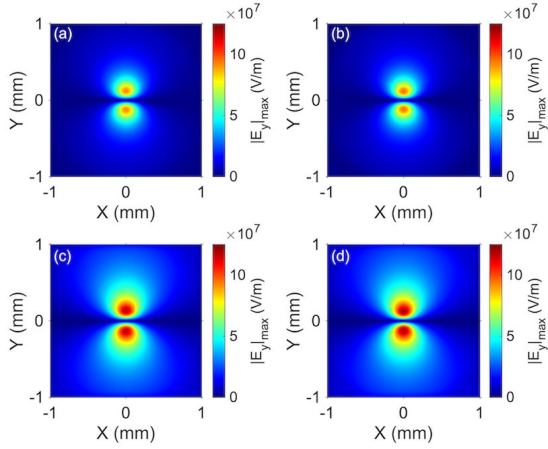


Fig. 2 Comparison of 3D calculated results of  $|E_y|_{max}$  obtained using the two approaches with different electron energies. All figures share the same colormap limit. (a) and (c) Calculation results of Huygens-Fresnel diffractions. (b) and (d) Calculation results obtained using an analytic model based on Fraunhofer's assumption. (a) and (b) show the results with an electron energy of 20 MeV, while (c) and (d) show the results with an electron energy of 200 MeV.

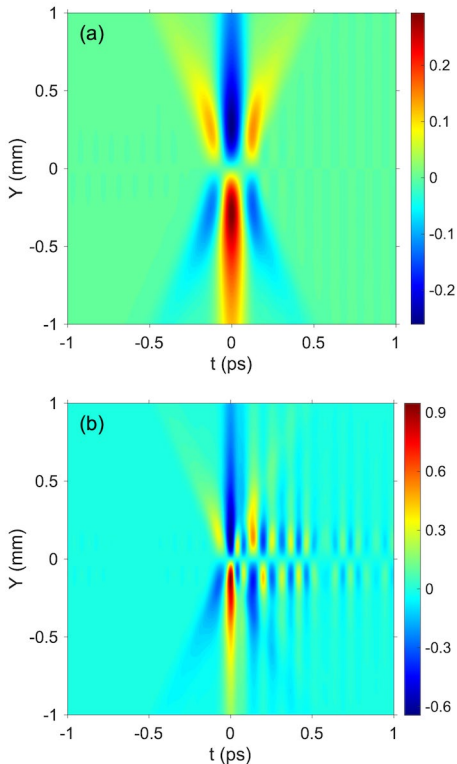


Fig. 3 2D spatial-temporal signals in dimensions (T, Y) obtained using a GaP crystal with thickness of 30  $\mu\text{m}$ . The electron bunches have charges of 32 pC and transverse sizes of 50  $\mu\text{m}$ . (a) and (b) 2D EO signals from electron bunches with temporal durations of 50 and 20 fs, respectively.

3D TR imaging is conducted using two approaches: one involving calculation based on Huygens–Fresnel diffractions, while the other utilizes an analytic model grounded on the Fraunhofer assumption. The computed results from both methods vary with electron energies, as illustrated in Fig. 2. The electron bunch parameters include charge = 32 pC, transverse beam size = (50, 50)  $\mu\text{m}$ , and bunch duration = 20 fs (root mean square, Gaussian). Remarkably, the TR field distributions obtained from both approaches are nearly identical. For electron energies of 20 and 200 MeV, the peak values of  $|E_y|_{max}$  from the detailed calculations are only 3 % lower than those derived from the simplified analytic model. The slight variance demonstrates the suitability of employing an analytical model for parameter fitting purposes.

The generation of “spatial-temporal” 2D EO signals is achieved through calculations of EO spatial decoding, as depicted in Fig. 3. Notably, the signals exhibit opposite signs relative to the horizontal line “Y = 0”, in correspondence with the radial-polarization characteristic of the TR field. As the bunch duration decreases from 50 to 20 fs, oscillations emerge due to phase-mismatch and absorption effects, as illustrated in Fig. 3(b). Moreover, the temporal profile varies with different vertical distances “Y”, showing the spatial-frequency distribution of the TR field.

In summary, a systematic numerical investigation is conducted on EO spatial decoding of TR emitted by relativistic electron bunches. This study offers valuable insights into investigations on the 3D charge–density profiles of ultrafast electron bunches in both laser wakefield acceleration and conventional accelerators. For further details, please refer to the recently published article, “K. Huang et al., *Physical Review Accelerators and Beams* 26, 112801 (2023).”

## Acknowledgments

We are grateful for the encouragement provided by Dr. Y. Sano, and Dr. N. Kumagai. We thank Dr. J. K. Koga for providing valuable insights into the current research topic. We thank Dr. Yiwen. E from the University of Rochester for fruitful discussions. This work was funded by the JST-Mirai Program, Japan (Grant No. JPMJMI17A1); the Grant-in-Aid for Early-Career Scientists (Grant Nos. JP21K17998 and JP23K17152); Grant-in-Aid for Scientific Research (C) from JSPS KAKENHI, Japan (Grant No. JP22K12665); and the QST President's Strategic Grant (Exploratory Research), Japan.

## References

1. T. Tajima and J. M. Dawson, *Phys. Rev. Lett.* 43, 267 (1979).
2. W. P. Leemans et al., *Nat. Phys.* 2, 696 (2006).
3. X. Yan et al., *Phys. Rev. Lett.* 85, 3404 (2000).
4. B. Stefen. No. DESY-THESIS-2007-020. DESY, (2007).
5. K. Huang et al., *Appl. Phys. Express* 15, 036001 (2022).
6. K. Huang et al., *Crystals*, 10, 640 (2020).
7. K. Huang et al., *Phys. Rev. Accel. Beams* 22, 121301 (2019).
8. K. Huang et al., *Scientific Reports* 8, 2938 (2018).
9. J. van Tilborg et al., *Phys. Rev. Lett.* 96, 014801 (2006).
10. A. D. Debus et al., *Phys. Rev. Lett.* 104, 084802 (2010).
11. Q. Tian et al., *Phys. Rev. Accel. Beams* 23, 102802 (2020).
12. K. Huang et al., *Phys. Rev. Accel. Beams* 26, 112801 (2023).

# Pointing stable low-divergence 100 keV-class electron beam generation driven by near-critical-density LWFA formed by microcapillary target



MORI Michiaki

High-field Science Research Group, Department of Advanced Photon Research

## 1. Introduction

Laser-driven electron acceleration can generate a GeV-class electron beam with an acceleration length of several centimeters owing to its high acceleration gradient, and it can be downsized by 1/1000 compared to conventional RF electron accelerators [1]. Such a drastically downscaled electron accelerator will be expected as the next generation X-FEL [2]. On the other hand, many applications, such as electron microscopy and sterilization, use electrons with energies below 1 MeV (i.e., soft electrons [3]), and social demand is higher than GeV electrons. Tajima et al. proposed generating a low-energy laser-driven electron beam and its applications as a high-dose-radiation cancer therapy [4,5]. This technique uses a plasma density near the critical density produced by a solid carbon nanotube target to generate low-energy electrons via laser-plasma interaction at an acceleration length of a few microns. In such an approach, the design and fabrication of carbon nanotube configurations are necessary, and additional research and development are required. On the other hand, since the hollow fiber (microcapillary plate (MCP)) utilizes the plasma generated by laser ablation inside the hollow fiber, the generated plasma density profile inside the capillary can be controlled by the inner diameter of the capillary. Furthermore, MCP is a fundamental technology for electron multiplier tubes, so it is possible to supply precise and high-quality targets. In this work, the soft electron beam generation using a MCP target was demonstrated. The energy distribution and the spatial distribution of electrons were measured [6].

## 2. Experimental setup and results

The experimental setup is shown in Fig. 1(a). The experiment was conducted using a terawatt Ti:Sapphire laser, JLITE-X, at the KPSI QST. The terawatt laser pulse from JLITE-X was focused with a 30  $\mu\text{m}$  spot diameter at 13.5 % of the peak intensity into a MCP target (Fig. 1(b)) by an  $f/22$  off-axis parabola mirror. The MCP target has a two-dimensional microcapillary array (an effective diameter of 27 mm attached to a 30-mm-diameter glass plate). The microcapillary hole's diameter and capillary length of the MCP were 10  $\mu\text{m}$  and 410  $\mu\text{m}$ , respectively. The microcapillary hole of the target was set parallel to the laser beam axis. Here, the direction of the capillary hole of MCP was tilted at  $12^\circ$  from the normal of the plate to avoid optical damage by back reflection from the target.

Figure 2 shows the typical energy spectra of generated electrons. The pump laser intensity was changed from  $4 \times 10^{16}$   $\text{W}/\text{cm}^2$  to  $1 \times 10^{18}$   $\text{W}/\text{cm}^2$  by changing the pump laser pulse duration from 1 ps to 40 fs at a laser energy of 160 mJ constant. Here, the effective laser energy coupled to a single capillary was estimated to be 27 mJ by considering the geometrical configuration. To measure these spectra, an electromagnet and an imaging plate (IP) were used. The electron yield and the slope of

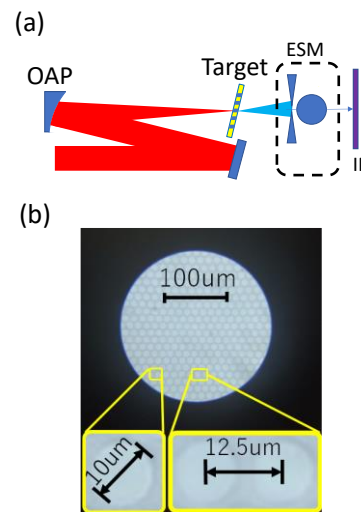


**Figure 1 (a) Experimental Setup. (b) Microscopy image of the MCP target surface [6].**

the spectra below 100 keV showed a weak dependence on the pump laser pulse duration except at a pump laser pulse duration of 1 ps. The electron yield was markedly decreased at the pump pulse duration of 1 ps. The hot tail profile that contained a little humped structure at around 200-400 keV significantly changed with increasing laser intensity. Below  $2.5 \times 10^{17}$   $\text{W}/\text{cm}^2$ , the hot tail above 200 keV showed a Maxwell-Boltzmann-like profile. It became a humped structure with peaks at around 300 keV at the highest intensity of  $1 \times 10^{18}$   $\text{W}/\text{cm}^2$ . On the other hand, these electron beams were highly collimated. Figure 3 shows the divergence of the generated electrons with energies above 40 keV as a function of pump laser intensity. In the measurement, the electromagnet was removed. The spatial distribution of electrons was measured by using an IP (Fujifilm BAS-SR) with an Al 12  $\mu\text{m}$  filter. These results were taken by a single shot. The beam divergence of  $\sim 30$  mrad at half-angle in the form included in a weak background electron energy of a few tens keV was observed. This electron beam has a very weak dependence on the pump laser intensity and is close to the field of view angle at the capillary tube ( $\alpha \sim 25$  mrad, where  $\alpha$  is half-angle). In a former work, collimated X-ray generation from an X-ray tube coupled with a MCP has been demonstrated. A 2mm thick MCP plate consisting of the diameter of a 12  $\mu\text{m}$  microcapillary hole was used in the experiment. The beam divergence of 4.5 keV X-rays passing through the microcapillary plate was measured to be 5.6

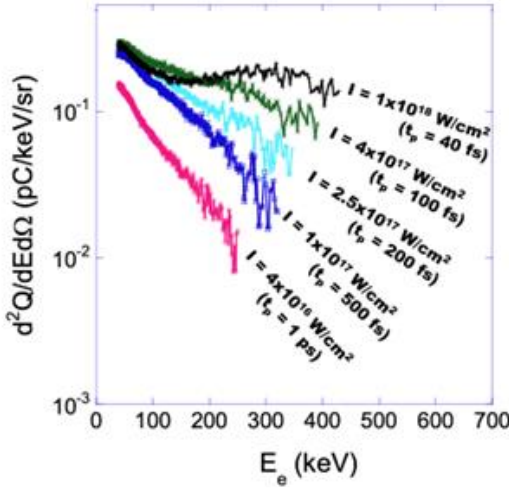


Figure 2 Experimentally obtained electron energy spectra for various laser pump intensities and laser pulse durations. The effective laser energy incident into the microcapillary was constant ( $E = 27$  mJ) [6].

mrاد in half angle which agrees with the field of view angle at the capillary tube ( $\alpha = 6$  mrad). A similar mechanism is thought to have happened in our experiment. Here, the yield of energetic electrons at  $>40$  keV was estimated to be  $10^6$  order or sub-pC electron charge from the electron.

This value is evaluated to be 1% order of the number of electrons contained in the volume by the product of the microcapillary diameter and the acceleration length when the average density is assumed to be the critical density. This collimated electron beam has highly pointing stabilized. Shot-to-shot pointing fluctuations in root-mean-square deviation (RMSD) were 1.7 mrad in horizontal and 1.9 mrad in vertical for ten shots at the maximum laser intensity. These values were more than ten times smaller than the beam divergence. This result indicates microcapillaries have not only beam collimating but also contribute to the beam pointing stabilization.

In summary, the first definitive near-critical-density LWFA experiment using a microcapillary target that shows a strong coupling of the laser to electrons at near-critical density has been performed. A pointing stable low-divergence 100-keV-class

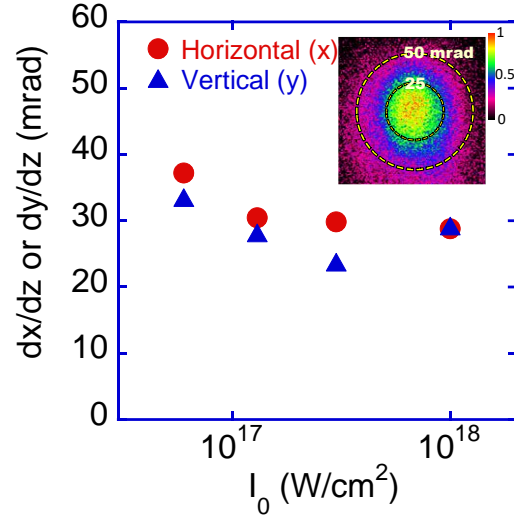


Figure 3 FWHM divergence of electrons at  $>40$  keV as a function of laser intensity. The inset shows a typical single-shot electron image at the laser intensity of  $1 \times 10^{18}$  W/cm<sup>2</sup> [6].

electron beam was generated by using a MCP target. This new regime of LWFA may be very suitable for future extremely compact keV electron accelerators such as endoscopic radiotherapy equipment.

#### Acknowledgments

This research was partially supported by the JST-Mirai Program (Grant number JPMJMI17A1) and by the Japanese Ministry of Education, Culture, Sports, Science and Technology (MEXT) through the JSPS KAKENHI Program (Grant number 20K12505 and 23K11716).

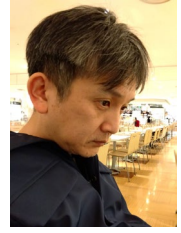
#### References

1. T. Tajima and J.M. Dawson, Phys. Rev. Lett. **43**, 267 (1979).
2. K. Nakajima, Nature Phys. **4**, 93 (2008).
3. T. Hayashi, Nip. Kag. Kai. **49**, 559 (2002).
4. B. S. Nicks *et al.*, Photonics **8**, 216 (2021).
5. D. Roa *et al.*, Photonics **9**, 403 (2022).
6. M. Mori *et al.*, AIP Advances (in press).

# Single-pulse extraction using a laser-activated GaAs reflective switch for a terahertz free-electron laser

KAWASE Keigo

LCS Gamma-ray Group, Department of Advanced Photon Research



The terahertz free-electron laser (THz FEL) at SANKEN, Osaka University, generates an intense pulse train of terahertz radiation. A typical radiation frequency range covers 3 to 7 THz. The number of pulses in a train is  $\sim 200$  with a pulse interval of 37 ns and the radiation energy of the train exceeds 45 mJ. The maximum pulse energy exceeds 200  $\mu\text{J}$ , which is one of the highest pulse-energy class terahertz radiation sources in the world. When a train of terahertz pulses is irradiated on a sample, it is difficult to judge whether the result is due to a high field or total energy. Therefore, extracting a single pulse from a terahertz pulse train is useful for various experiments studying high-field effects in the terahertz range.

The extraction method adopted in this study is a technique of semiconductor reflective switching. Normally most semiconductors are highly transmitting materials for terahertz radiations. By irradiating an intense laser pulse with photon energy exceeding the bandgap energy of the semiconductor, the electron-hole plasma is excited on the surface, which turns highly reflective for terahertz radiation. Then, the excited surface can be brought back to the normal state after a specific relaxation time depending on the material species. Compared to indirect bandgap semiconductors such as Si and Ge, GaAs is a typical direct bandgap semiconductor that is expected to have a faster response of switching to extract a single pulse from a train. Therefore, the GaAs reflective switching to extract a single terahertz pulse is thoroughly investigated in this study.

The schematic of the experimental setup is shown in Fig. 1. The THz FEL is transported from the accelerator room through the vacuum duct, and extracted from the vacuum chamber through the diamond window. Two wire grid polarizers are used. The first polarizer is used for changing the FEL intensity, while the second one is used to ensure a definite polarization direction in the horizontal plane. Two off-axis parabola reflectors are used to down-collimate the FEL. The FEL is injected into the GaAs wafer with Brewster's angle of  $\sim 74^\circ$  for radiation with a wavelength of 70  $\mu\text{m}$ . The GaAs wafer is undoped and has a thickness of 0.5 mm. The laser pulse to activate the electron-hole

plasma on the GaAs surface is generated by a regenerative Ti:sapphire laser system (Spitfire, SpectraPhysics, Inc.), which generates an output power of 700 mW, nominal pulse duration of 100 fs, and repetition frequency of 960 Hz. Irradiation energy on the GaAs can be varied with a half-wavelength plate and polarizing beamsplitter. The maximum irradiation energy on the GaAs is 0.56 mJ. An optical delay line is inserted in the laser transport line with a motorized linear stage to match the timing between the laser pulse and terahertz pulse. The reflected terahertz pulse is detected by an energy sensor (J10MB-LE, Coherent Inc.) or a fast pyroelectric detector (P5-00, Moletron Detector Inc.). The transmitted terahertz pulse train is detected by an energy sensor with a larger aperture (J50MB-LE, Coherent Inc.) or also by the P5-00 detector.

The spatial beam profile of the terahertz pulse is directly measured by a two-dimensional pyroelectric sensor array (IR/V-T0831 THz Imager, NEC Corp.). The beam sizes of the terahertz pulse of wavelength 70  $\mu\text{m}$  at the wafer position in the standard deviation are evaluated to be 0.38 and 0.33 mm in the horizontal and vertical directions, respectively. The beam profile of the laser pulse is observed through the irradiation image by putting a paper sheet at the wafer position with Brewster's angle to the terahertz beam axis by a CMOS camera (DMK21BUC03, The Imaging Source, LLC). The beam sizes of the laser pulse on GaAs in the standard deviation are evaluated to be 3.2 and 2.3 mm in the horizontal and vertical direction, respectively. Notably, the spatial profile of the terahertz pulse is horizontally enlarged to 1.43 mm due to Brewster's angle injection, while the laser profile shows the actual beam sizes on the GaAs surface. Therefore, the spatial overlapping of the terahertz pulse on the laser irradiation area is enough for this experiment considering Brewster's angle injection.

A typical waveform of the transmitted terahertz pulse train detected by P5-00 without switching is shown in Fig. 2(a) and its enlarged image is shown in Fig. 2(b). The train structure confirms that the laser-activated reflective switching technique with GaAs can extract a single terahertz pulse, as shown in Fig. 2(c). The reflected pulse energy with laser activation is  $180 \pm 25 \mu\text{J}$ , while without activation is  $104 \pm 14 \mu\text{J}$ . Thus, the maximum extracted pulse energy is calculated as  $76 \pm 28 \mu\text{J}$ , where the incident pulse energy is estimated as  $161 \pm 23 \mu\text{J}$ . Therefore, the reflectivity of the switch is evaluated to be 0.47. One of the possible reasons for the reduction of reflectivity from unity involves the intervalley scattering of a part of terahertz pulse due to its high intensity. The issue is for future studies to investigate in further detail.

The dependence of the extracted pulse energy on the irradiated laser fluence is shown in Fig. 3. The reflected pulse energy saturates at  $0.6 \text{ mJ}/\text{cm}^2$  of laser irradiation. The value is half the possible fluence in this experiment. Thus, the acceptable spatial mismatching between the terahertz pulse and the laser pulse can be calculated. The 1-standard deviation beam size of the terahertz pulse in Brewster's angle injection is 1.43 mm, as

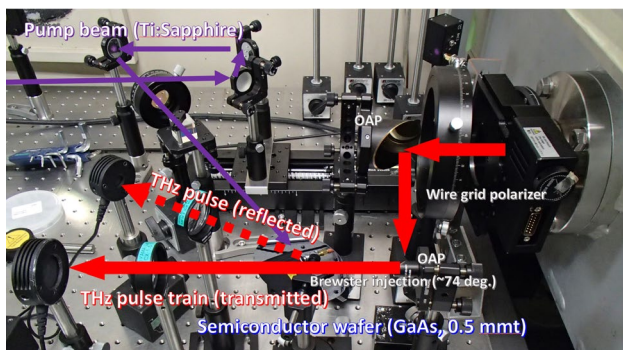


Figure 1: Experimental setup.

mentioned. Conversely, the full-width half maximum (FWHM) beam size of the laser is 7.5 mm. The ratio is 5.3; thus, 99 % of the terahertz pulse is contained in the FWHM of the laser spot. Therefore, misalignment does not cause such a large reduction in reflectivity.

The switching technique can be used for a wide wavelength range. Figure 4 shows the result for the whole range of the THz FEL at SANKEN with fixed electron beam energy. The wavelength dependence of the reflected energy shows similar behavior to the total energy of the pulse train, implying the switching action has no clear dependence on the wavelength. Thus, the technique can be used for the entire wavelength range of THz FEL at SANKEN.

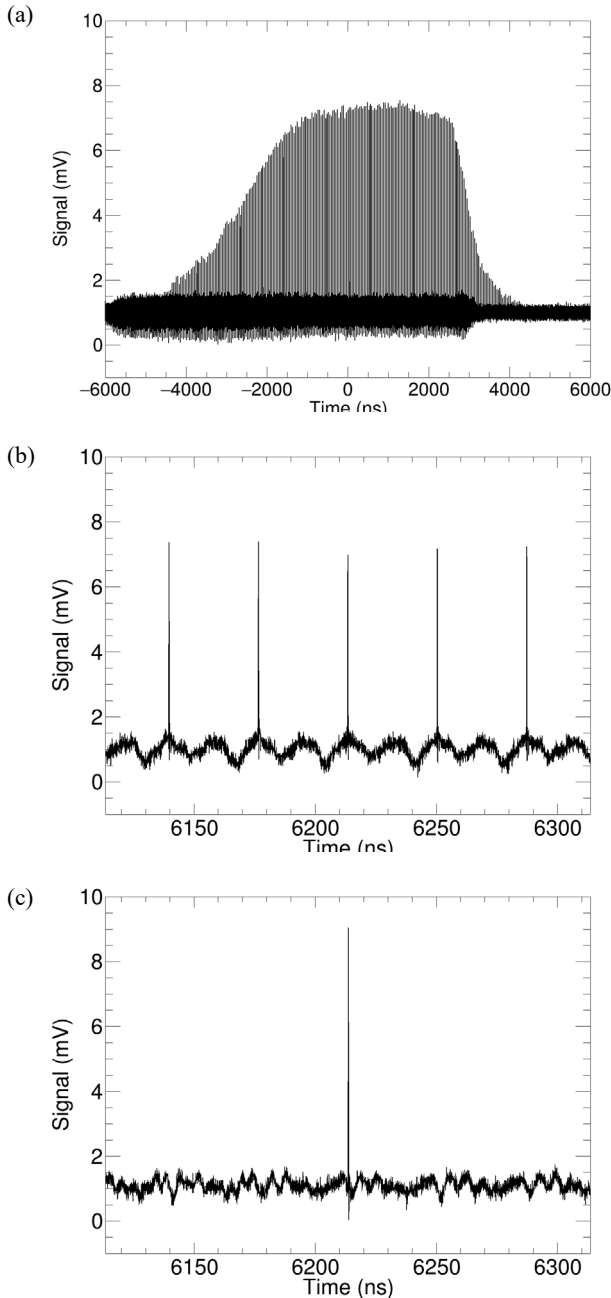


Figure 2: (a) Typical waveform of the transmitted terahertz pulse train and (b) the enlarged waveform. The energy of the terahertz pulse gradually increases in a few microseconds, and then attains saturation. The length of the train is  $\sim 6\text{--}7\ \mu\text{s}$ . (c) Reflected pulse waveform by laser-activated switching. No satellite pulses are available in the linear scale.

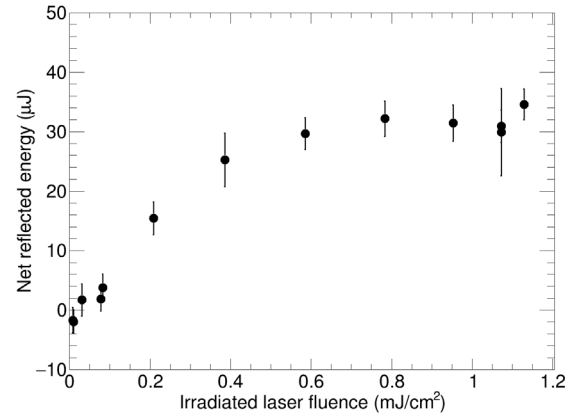


Figure 3: Dependence of extracted pulse energy on the irradiated laser fluence.

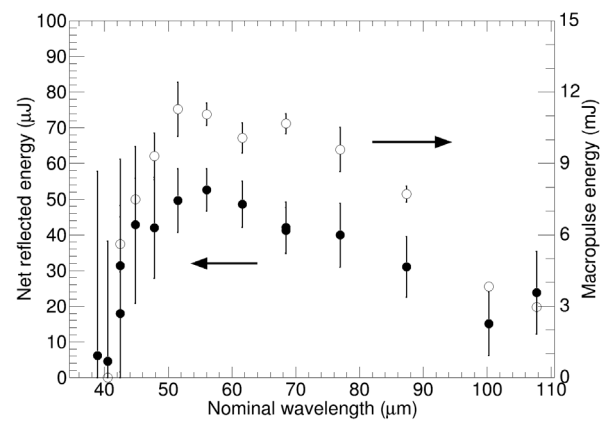


Figure 4: Wavelength dependence of the reflected energy and total energy of the terahertz pulse train in the entire range of THz FEL.

In summary, the single-pulse extraction of an intense terahertz pulse of FEL is investigated by using a laser-activated semiconductor reflective switching technique. The maximum extracted pulse energy is 76  $\mu\text{J}$ , and the technique applies to the whole wavelength range of the SANKEN THz FEL.

Detailed descriptions of this report have already been published [1].

## Acknowledgments

The author thanks the Japan Society for the Promotion of Science, Japan under the Grants-in-Aid for Scientific Research (Contract no. 20K12491, 15K13407, and 24310069) and the Ministry of Education, Culture, Sports, Science and Technology, Japan, Japan under the Quantum Leap Flagship Program (Grant no. JPMXS0118070271) and performed under the Cooperative Research Program of “Network Joint Research Center for Materials and Devices”, Japan (Subject no. 20222007 and 20202008).

## References

1. K. Kawase and G. Isoyama, Nucl. Instrum. and Methods in Phys. Res., A 1056 (2023) 16818 (doi:10.1016/j.nima.2023.168618).

# Half-life measurement of a long-lived radioisotope $^{176}\text{Lu}$

HAYAKAWA Takehito

LCS Gamma-ray Group, Department of Advanced Photon Research



A meta-stable isotope  $^{176}\text{Lu}$  exists in the present solar system with an isotopic fraction of  $2.59874 \pm 0.00012\%$ . It decays to its daughter nucleus  $^{176}\text{Hf}$  with a half-life of approximately  $4 \times 10^{10}$  y, where the  $6^+$  state in  $^{176}\text{Hf}$  is predominantly produced and gamma-rays with energies of 88, 202, 307, and 401 keV are radiated (Fig. 1). The  $^{176}\text{Lu}$ - $^{176}\text{Hf}$  system has the potential as a nuclear chronometer for evaluation of an age from a stellar nucleosynthesis event to the present [1, 2] and an age of formation and evolution of planets and moon [3, 4]. However, the half-life of  $^{176}\text{Lu}$  is yet to be established.

The values of the half-life have been reported using various nuclear experiment techniques but the results are not consistent. Such techniques can be classified into the following three groups. First is the gamma-ray measurement using a single detector. Second is the gamma-gamma (beta-gamma) coincidence measurement including the sum peak method. Third is beta-ray measurement using a liquid scintillation detector. In these methods, the half-lives were reported by measuring the 202 or 307 keV gamma-ray with a scintillation detector or a high-energy resolution germanium detector. The results depend on the emission probability of the gamma-ray in the decay of  $^{176}\text{Lu}$  and the detection efficiency. The emission probabilities of the gamma-rays have uncertainties. The detection efficiency is generally evaluated using standard radioactive sources but they have typically uncertainties of a few percent. The gamma (beta)-gamma coincidence method depends on the angular correlation between two radiations and the shape of the target. They are typically evaluated with simulation calculation. Liquid scintillation detectors are also calibrated using a standard

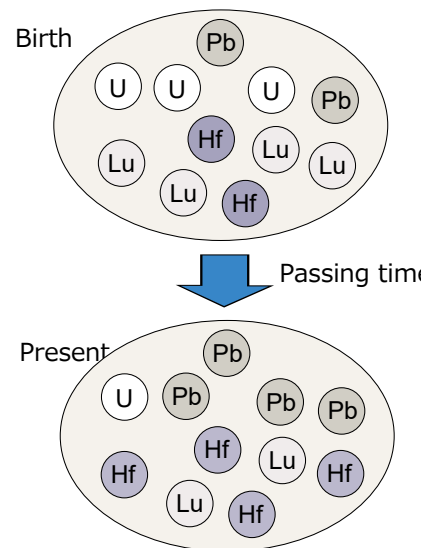


Figure 2 Schematic picture of nuclear chronometer.

radioisotope such as  $^3\text{H}$ , and they exhibit uncertainties of a few percent.

Furthermore, the half-life of  $^{176}\text{Lu}$  was evaluated from the Lu-Hf isochron methods of meteorites and terrestrial materials. First, the ages of the samples were evaluated and then the half-life of  $^{176}\text{Lu}$  is evaluated from the isotopic abundances of Lu and Hf (Fig. 2). A half-life of approximately  $3.72 \times 10^{10}$  y was reported for terrestrial rocks and meteorite phosphates [5, 6]. However, different half-lives of approximately  $3.51 \times 10^{10}$  y were provided through the analyses of several meteorites [4]. The discrepancy has been an unresolved problem. To understand the discrepancy, the true half-life of  $^{176}\text{Lu}$  should be known.

The inconsistency in the half-lives measured by the nuclear experiments does not depend on measurement methods. Thus, even when a half-life value of  $^{176}\text{Lu}$  is precisely measured using one of the known methods, it is difficult to know whether it is close to the true value. As aforementioned, the previous values may be affected by the uncertainties of detection efficiency, radioactivity of standard radioisotope source, and nuclear structure in the experiments. Thus, we explore the half-life using a new method that is not sensitive to such uncertainties.

In the present study [7], we use a windowless  $4\pi$ -type large volume BGO detector to measure gamma-rays, x-rays and electrons radiated from a natural Lu sample located inside the detector (Fig 3). The BGO materials exhibit the remarkable features of non-deliquescent and large stopping power originating from the large atomic number element bismuth. Owing to the non-deliquescent it is possible to make a windowless detector. The detector consists of two BGO crystals and a photomultiplier tube (PMT) (Hamamatsu Photonics K.K., R1307-07). The size of

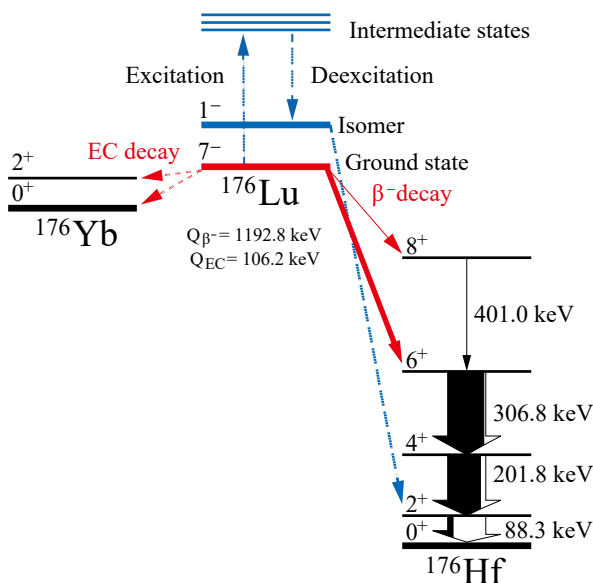


Figure 1 Partial decay scheme of  $^{176}\text{Lu}$

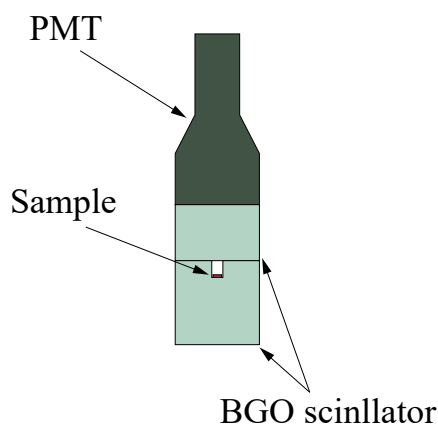


Figure 3 Experimental setup.

the first BGO crystal is  $\phi 3$  inch.  $\times$  2 inch, whereas the second is a well-type crystal with a size of  $\phi 3$  inch.  $\times$  3 inch, which has a hole of  $\phi 10$  mm  $\times$  15 mm. The thickness of the BGO crystals is selected to detect almost all gamma-rays from  $^{176}\text{Lu}$ . A sample is located inside the BGO crystals (Fig. 3) for measuring almost all decays. The detection probabilities of photons and electrons from the natural Lu sample can be calculated using the PHITS particle and heavy ion transport code system, where detection implies that the energy deposited in the BGO crystals by an incident particle is higher than or equal to 30 keV. The lower limit is verified by the measurement of the Cs x-ray at approximately 31 keV from a  $^{133}\text{Ba}$  radioisotope source located inside the detector. The detection probabilities of photons with energies of 200–350 keV are higher than 99.5%. We conservatively evaluate the total detection probability for  $^{176}\text{Lu}$  decay of approximately  $99.9 \pm 0.01\%$ .

Background radiations exist in the laboratory. Thus, the detector is shielded using lead blocks with a typical thickness of 150 mm and copper plates with a thickness of 15 mm. The signals from the PMT are amplified using an ortec 113 scintillation preamplifier and an ortec 672 spectroscopy amplifier. The signals from the amplifier are recorded using a multi-channel analyzer (K. K. TechnoAP, APG7400A). The background counting rate is approximately 4 count per second (cps) and the counting rate with a Lu sample is approximately 12 cps. The weights of two Lu foils are  $125.26 \pm 0.05$  and  $121.43 \pm 0.05$  mg. Because the evaluated isotopic abundance of  $^{176}\text{Lu}$  is as precise as  $2.5987 \pm 0.0012\%$ , we use natural Lu samples. The decay from each Lu sample and the background without the samples are measured for 48 h, respectively. The half-life can be obtained from the total number of beta decay. We finally obtain the half-life of  $(3.719 \pm 0.007) \times 10^{10}$  y.

The present method has the following three advantages. First, the obtained value is almost insensitive to nuclear structure such as gamma-ray emission probability and electron capture branching ratio. Second, the presently obtained half-life is not sensitive to the calculated result of detection efficiency, because the detection efficiency is almost 100%. Third, the detection efficiency is free from the uncertainties of calibration sources because they have not been used in the present study. Thus, we conclude that the presently measured half-life is more accurate than those measured by the previous nuclear and geochemical experiments. In addition, the present method is the most precise among all the methods (Fig. 4). Thus, it is expected that the present result contributes to the study of formation and evolution

of our solar system and ages of stellar events before the solar system formation.

The presently measured half-life is consistent with that obtained by the age comparison with the U-Pb method in terrestrial rocks and meteorite phosphates [5, 6]. This indicates the following three facts. First, the present half-life is consistent with the precisely measured half-lives of  $^{235,238}\text{U}$ , and thus the Lu-Hf system could be used for dating a sample consistent with the U-Pb method even if the latter cannot be used. Second, the longer half-life measured in meteorites is close to the true value, and a mechanism that explains the shorter half-life obtained from other meteorites is required [4]. One of the possible mechanisms involves decay acceleration by cosmic gamma-ray irradiation in the early solar system. As shown in Fig. 1, an isomer with a short half-life of approximately 3.7 h exists in  $^{176}\text{Lu}$ . When  $^{176}\text{Lu}$  is irradiated with gamma rays of energies higher than MeV, intermediate states in  $^{176}\text{Lu}$  are excited with the absorption of gamma rays and partly decay to the isomer, subsequently decaying to  $^{176}\text{Hf}$ . Thus, the possibility that high energy cosmic-ray irradiation has occurred in the early solar system exists. To study this phenomenon, details on the isotopic abundances of Hf and Lu in various samples are required. In near future, the isotopic data of the samples obtained from an asteroid Ryugu by Hasabusa2 project [8] are expected to provide hints for understanding decay acceleration.

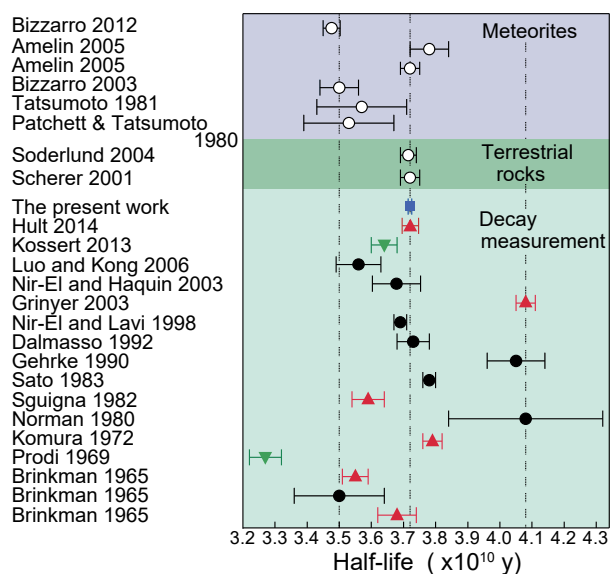


Figure 4 Measured half-life values of  $^{176}\text{Lu}$

## Acknowledgments

This work was supported by JSPS KAKENHI Grant Numbers JP22H00170 and JP22H01239.

## References

1. H. Beer, et al. *Astrophys. J. Supp.* **46**, 295 (1981).
2. T. Hayakawa, et al. *Phys. Rev. Lett.* **93**, 161102 (2004).
3. P. J. Patchett, *Geochim. Cosmochim. Acta* **46**, 81 (1983).
4. M. Bizzarro, et al. *Nature* **421**, 931 (2003).
5. E. Scherer, et al. *Science* **293**, 683 (2001).
6. Y. Amelin, et al. *Science* **310**, 839 (2005).
7. T. Hayakawa, et al. *Comm. Phys.* **6**, 299 (2023)
8. T. Yokoyama, et al. *Science*, **379**, eabn7850 (2022).

# Research Activities at the Synchrotron Radiation Research Center

WATANUKI Tetsu

Synchrotron Radiation Research Center



A wide range of X-ray techniques are being developed at the Synchrotron Radiation Research Center (SRRC) to investigate the structural, electronic, and magnetic properties of matter, primarily using two QST beamlines, BL11XU and BL14B1, at the large synchrotron radiation facility, SPring-8. Hard X-ray non-destructive *in-situ* techniques have been investigated to enable ground-breaking measurements using techniques including single atomic-layer magnetic microscopy, element/orbital-specific excited-state analysis, coherent X-ray nanoscale imaging, and time-resolved studies of samples under extreme conditions such as extremely high pressures of hydrogen gas.

The SRRC has been partially reorganized this year and consists of the Coherent X-ray Research Group, Hydrogen Materials Research Group, Magnetism Research Group, Advanced Spectroscopy Research Group, and a beamline operation office (Table 1).

During 2023FY, Dr. T. Mitsui received the Minister of Education, Culture, Sports, Science, and Technology's commendation for developing an innovative single atomic layer resolved magnetic probing method and applying it to the study of the unique magnetic properties of iron surfaces. Furthermore, the Hydrogen Materials Research Group started participating in the Green Technologies for Excellence (GteX) program. Other research activities of each group are summarized as follows.

The equipment developed at SRRC is available for public use, and we accepted 46 research proposals in FY2023, as a project member institute of the Advanced Research Infrastructure for Materials and Nanotechnology, Japan (ARIM) [1].

Synchrotron and free-electron laser (FEL) X-ray facilities are being rapidly constructed worldwide. The **Coherent X-ray Research Group** is researching to ensure state-of-the-art synchrotron/FEL research. Advanced measurement and analysis techniques are being developed for the effective utilization of novel advanced light sources. The application of spatially coherent X-rays has facilitated the visualization of inhomogeneity inside matter.

An apparatus for Bragg coherent X-ray diffraction imaging (Bragg-CDI) is being developed for applications to the study of inhomogeneous structures of submicrometer-sized crystalline fine particles in functional materials. The technique has been upgraded for application to a BaTiO<sub>3</sub> single particle in ceramics [2] and negative thermal expansion materials [3].

Ultrafast and intense pulses from a soft X-ray FEL source such as SACLA (BL1) facilitate the investigation of processes such as vibration, dissociation, and charge transfer within single molecules. The ultrafast charge rearrangement during the dissociation of 2-iodopropane has been revealed using site-selective ionization of an iodine atom and tracking electron transfer between the resulting multiple-charged iodine ions and propyl fragments [4].

A surface X-ray diffractometer coupled with a molecular-beam-epitaxy chamber is used for the *in-situ* measurements of GaN crystal growth on several types of substrates under the approval of the QST-ARIM project.

The research objectives of the **Hydrogen Materials Research Group** include (i) fundamental and applied studies of hydrogen materials using synchrotron radiation X-rays, high-pressure apparatus, magnetron sputter apparatus, and theoretical calculations; (ii) the development of experimental techniques for *in-situ* measurements under extreme conditions, including high-hydrogen pressure and in compressed hydrogen gas environments; and (iii) studies on the effects of synchrotron X-ray irradiation on tumors. The research group members focus on the syntheses of novel hydrogen-rich compounds and theoretical calculations considering the quantum effect of hydrogen.

Metal-hydrogen systems under high pressure are the main research target of the group. Structural phase transformations and microstructure evolutions during hydrogenation and dehydrogenation of Fe-based alloy around 10 GPa have been investigated using *in situ* synchrotron radiation X-ray diffraction technique along with scanning electron microscope (SEM) analysis of a recovered sample at ambient pressure [5]. High-pressure hydrogenation of typical hydrogen storage alloy, LaNi<sub>5</sub> has been investigated. Hydrogenation reaction around 10 GPa has been observed to form hydrogen-rich hydride, LaNi<sub>5</sub>H<sub>x</sub> ( $x < 9$ ) [6]. Proton disorder in the C' phase of H<sub>2</sub> hydrate around 1 GPa has been investigated based on first principles molecular dynamics, where the quantum nature of nuclei is considered [7].

Additionally, studies have investigated the effects of irradiation on tumors, using nanoparticles containing high-Z elements. The effect of X-ray irradiation on tumor spheroids, in which iodine is introduced to enhance the radiation effect, has been investigated using synchrotron radiation X-rays ( $E = 33.2$  keV) above the iodine K-absorption edge.

The **Magnetism Research Group** investigates the electronic and magnetic properties of condensed matters to unveil the key properties of functional materials and devices using advanced X-ray spectroscopies, such as nuclear resonant scattering (NRS) and X-ray emission spectroscopy (XES), and theoretical calculations. For NRS, the magnetic phases of Mn<sub>2</sub>Fe<sub>x</sub>Ga thin films, which are candidate materials for high-speed memory, have been evaluated using conversion electron synchrotron radiation Mössbauer spectroscopy, which enables non-destructive analysis of magnetic structure. From spectral analysis, it was found that Mn<sub>2</sub>Fe<sub>x</sub>Ga thin films consisting only of magnetic phase suitable for high-speed memory were formed in the  $x = 1$  to 1.3 region [8].

This study successfully demonstrates that synchrotron Mössbauer spectroscopy is an effective tool for developing high-speed memory materials, which opens the door to future smart societies. X-ray magnetic circularly polarized emission (XMCPPE) is a variant of the XES techniques, which is novel magnetic spectroscopy operated in the hard X-ray regime with the distinctive feature of a large flipping ratio (25 %) for  $K\alpha$  emission of 3d transition metal elements. We developed an XMCPPE microscope and applied it for the observation of buried magnetic domains in grain-oriented electrical steel. Transverse domains, which are hidden internal magnetic domains, were successfully visualized for the first time owing to the large

penetration length of hard X-rays [9]. Additionally, theoretical frameworks and computational program codes to analyze the electronic and magnetic properties of strongly correlated electron systems probed by modern X-ray spectroscopies such as X-ray absorption and emission (XAS and XES), X-ray photoemission (XPS), resonant inelastic x-ray scattering (RIXS), and their magnetic dichroic spectroscopies, X-ray magnetic circular dichroism (XMCD), XMCPE, XPS-MCD have been developed. Our theoretical studies aim to provide insights and predictions for experimental observations from microscopic theoretical perspectives.

The *Advanced Spectroscopy Research Group* develops both hard and soft X-ray spectroscopic techniques for the synergistic use of SPring-8 and NanoTerasu to investigate the electronic and spin states of materials. Research that investigates the electronic states of materials using resonant inelastic X-ray scattering (RIXS) and X-ray emission spectroscopy (XES) is conducted by this group. The target materials range from strongly correlated electron systems including cuprate superconductors to functional materials such as battery electrodes and catalysts. Additionally, the group has developed various angle-resolved photoelectron spectroscopy (ARPES) instruments that enable the observation of electronic states of materials, with a particular focus on quantum materials. Building upon this expertise, the group is currently developing a novel “Nano-Spin ARPES instrument” at NanoTerasu, which enables the microscopic observation of electron and spin states at micro or nano-scales.

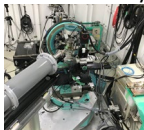
In today's era of data-driven research, the ability to efficiently collect and analyze large volumes of experimental data is a critical factor for success. Thus, cutting-edge measurement informatics methodologies that leverage machine learning and artificial intelligence technologies to streamline and automate the measurement and analysis of diverse synchrotron radiation experimental techniques, including X-ray absorption

spectroscopy and XMCD spectroscopy are under investigation. Furthermore, an innovative analytical approach based on machine learning has been developed to enable a higher level of evaluation of several-body interactions through a large amount of data from a single material using spatially resolved ARPES [10]. Various physical parameters, including the coupling strengths of electron-electron and electron-boson interactions, have been statistically evaluated, and the correlation between several-body interactions has been accessed. Interpretations of state-of-the-art experiments are often difficult and theoretical studies are indispensable. Therefore, the electronic states of transition metal oxides such as high-temperature superconducting cuprates are examined using numerically exact diagonalization techniques, and spectra such as RIXS and PES are discussed. In addition, the excitation spectra for the photoexcited state excited by the pump light are obtained by numerical calculations, and their characteristics are clarified theoretically. Recently, exciton-assisted low-energy magnetic excitations in a photoexcited Mott insulator on a square lattice have been reported [11].

## References

1. <https://www.qst.go.jp/site/arim/>
2. N. Oshime *et al.*, Jpn. J. Appl. Phys. **62**, SM1022 (2023).
3. T. Nishikubo *et al.*, Chem. Mater. **35**, 870–878 (2023).
4. F Allum *et al.*, Phys. Rev. A **108**, 043113 (2023).
5. R. S. Varanasi *et al.*, Int. J. Hydrogen Energy, **48**, 10081 (2023).
6. T. Sato *et al.*, Molecules, **28**, 1256 (2023).
7. T. Ikeda, Chem. Phys. Lett. **119**, 6784 (2023).
8. P. D. Bentley *et al.*, Phys. Rev. Materials **7**, 064404 (2023).
9. T. Inami *et al.*, IEEE Trans. Mag. **59**, 6000406 (2023).
10. H. Iwasawa, *et al.*, Phys. Rev. Research. **5**, 043266 (2023).
11. K. Tsutsui, *et al.*, Commun. Phys., **6**, 41 (2023).

Table 1. Groups at the Synchrotron Radiation Research Center.

Group	Coherent X-ray Research Group	Hydrogen Materials Research Group	Magnetism Research Group	Advanced Spectroscopy Research Group
<b>Members</b>	K. Ohwada (GL), J. Harries, T. Sasaki, N. Oshime	H. Saitoh (GL), T. Ikeda, A. Shiro, Y. Nakahira, (A. Machida)	T. Inami (GL), T. Mitsui, T. Nomura, K. Fujiwara	(Y. Katayama (GL)), K. Tsutsui, K. Ishii, T. Ueno, (H. Iwasawa)
<b>Typical techniques &amp; apparatuses</b>	Coherent X-ray scattering  Surface X-ray diffraction  Quantum optics in EUV region	High-pressure and high-temperature X-ray diffraction  Pair distribution function analysis  First-principles molecular dynamics simulations	Mössbauer spectroscopy  X-ray magnetic circularly polarized emission 	Resonant inelastic X-ray scattering  Numerical calculations 
<b>Research objective</b>	Ferroelectrics, nitride semiconductors, superfluorescence	Hydrogen materials, negative-thermal-expansion materials, irradiation effects on tumor	Magnetism, spintronics, X-ray spectroscopies	High- $T_c$ superconductivity, catalysis, magnets, measurement informatics
Beamline Operation Office / Y. Katayama (Section Manager), K. Sugawara, Y. Teraoka, T. Senou, A. Shimada, Y. Asai				

# Phase transition of a BaTiO<sub>3</sub> single particle in ceramics studied by Bragg-CDI techniques

OHWADA Kenji, OSHIME Norihiro



Coherent X-ray Research Group, Synchrotron Radiation Research Center

This study focuses on size effect [1-5] observed in dielectric materials. The size effect refers to the sample size dependence of physical properties that should be constant under the same environment. The size dependence of dielectric properties in BaTiO<sub>3</sub> nanocrystals is well-known; furthermore, a variation in the properties of the sample exists depending on the sample growth method [4, 5]. To approach the subject from the perspective of structure, the average atomic positions and temperature factors obtained by conventional X-ray structural analysis are not sufficient. To know the nm-to- $\mu\text{m}$  structure of a single particle, such as the size, shape, internal structure (including strain, domains, and defects), and the effects of grain boundaries in the case of sintered particles, understanding the size-dependent physical properties is crucial.

As a technique to visualize single crystalline particles, we focus on the Bragg-CDI method [6, 7], which uses Bragg diffraction sensitive to strain inside the crystal. The Bragg-CDI method was developed at the Advanced Photon Source (APS) and the European Synchrotron Radiation Facility (ESRF) and has been used mainly in the fields of catalysts and semiconductors [6, 7]. However, no facility in Japan has been able to perform the method thus far. Therefore, we introduced the technique into our research and have achieved public use from FY2022 under the Advanced Research Infrastructure for Materials and Nanotechnology in Japan (ARIM) project by the Ministry of Education, Culture, Sports, Science and Technology (MEXT) of Japan. In this report, we present the applications of the Bragg-CDI method to investigate the phase transition of BaTiO<sub>3</sub> nanocrystals [8-12].

The apparatus for the Bragg-CDI method has been installed at BL22XU of SPring-8, Hyogo, Japan [8]. CDI is a method to obtain real images by precisely collecting coherent X-ray diffraction patterns, called speckle, obtained by irradiating a sample with coherent X-rays and performing phase retrieval calculations. The Bragg-CDI method provides not only scattering amplitude corresponding to the electron density but also phase corresponding to the deviation (strain) of the atomic positions from the average position, allowing us to discuss the non-uniformity of crystals. The Bragg-CDI method focuses on the Bragg diffraction to easily obtain three-dimensional (3D) information by rotating the crystal angle by a few degrees, while the transmission-based method requires the sample to be rotated 180° to obtain a 3D image. The former is greatly advantageous for in-situ measurement where the measurement window is limited and sample movement is severely restricted.

The following is the experimental flow to obtaining the 3D image. (1) Dispersed crystals are supported on a thin silicon nitride substrate that does not modulate the coherence of X-rays and mounted on the experimental apparatus. Coherent X-rays (8 keV, wavelength 0.1549 nm) obtained from a synchrotron radiation source are focused to  $\sim 2 \times 2 \mu\text{m}^2$  and irradiated to the crystal. (2) Diffraction from the crystal is acquired by oscillating the crystal to  $\sim \pm 1^\circ$  using a photon-counting 2-dimensional X-ray detector, Eiger500k (Paul Scherrer Institut). The obtained data are

assembled into 3D voxel data. (3) Phase retrieval calculations are performed to obtain a 3D real image of the crystal. The scattering amplitude (corresponding to electron density) and phase (corresponding to strain) are obtained by analysis.

For Bragg-CDI method in QST, a focused X-ray beam of 2  $\mu\text{m}$  is irradiated to a crystal at the 100 nm level. Therefore, the drift, however tiny, occurring when the sample environment changes, is fatal because it can cause the signal from the sample to be lost. Since the heating stages typically used in the synchrotron radiation X-ray measurement are not sufficient, a MEMS heating system used in electron microscopy for synchrotron radiation X-ray diffraction experiments (NHB-5100, NORCADA Inc.) has been modified [10]. A heater patterned on a silicon nitride substrate locally heats an area of  $\sim 200 \mu\text{m}$  at the center and can be controlled from room temperature to 1100 °C in a vacuum environment. The response is very good, reaching the desired temperature quickly (within 1 s). The heater is controlled from a dedicated PC via GUI, which can be remotely operated via TCP/IP. Therefore, the temperature can be controlled from the diffractometer control program, and automatic measurement of temperature variation of diffraction patterns is possible. For this study, the experiments with BaTiO<sub>3</sub> nanoparticles enable the tracking of samples without losing sight during measurements from room temperature to  $\sim 300^\circ\text{C}$  across a phase transition of 120 °C. Although the drift is specified to be less than 10 nm/hr, the crystal is only placed on the substrate, and the crystal itself moves due to the phase transitions and thermal expansion, such that the exact amount of drift under the Bragg-CDI measurement environment cannot be estimated.

In 2021, our previous study reported the results of imaging isolated particles supported on a substrate at room temperature [9]. In the experiment of 40 nm crystal, the sample was supported on the substrate and gold was deposited on the entire substrate to suppress the drift of the sample [9]. However, physical fixation added unnecessary stress to the sample and was not desirable. Currently, experiments can be performed without the fixation materials for particles of any size [13].

This paper reports the results of imaging a single nanocrystal in a fine piece of ceramics obtained from sintered BaTiO<sub>3</sub> particles of 300–400 nm in size down to  $\sim 5 \mu\text{m}$ . The experiment was performed using the aforementioned MEMS heating system. The ferroelectric-paraelectric phase transition ( $T_c \sim 120^\circ\text{C}$ ), which is a characteristic of BaTiO<sub>3</sub>, was observed. The grain shape recovered at 300 °C (paraelectric phase), which was free from domain-derived strain before and above the phase transition, shows a grain boundary structure reflecting the stone-wall-like stacking characteristics of ceramics, as in Fig. 1. The cross-sectional view shows several stress distributions that can be influenced by the grain boundaries even at 300 °C. The strain is represented by the intensity of color from red to blue, indicating the amount of atom displacement from the average atomic position. A phase of  $2\pi$  corresponds to the amount of deviation by a lattice constant ( $a$ ), from  $-\pi$  displacement (red) to  $+\pi$  displacement (blue).

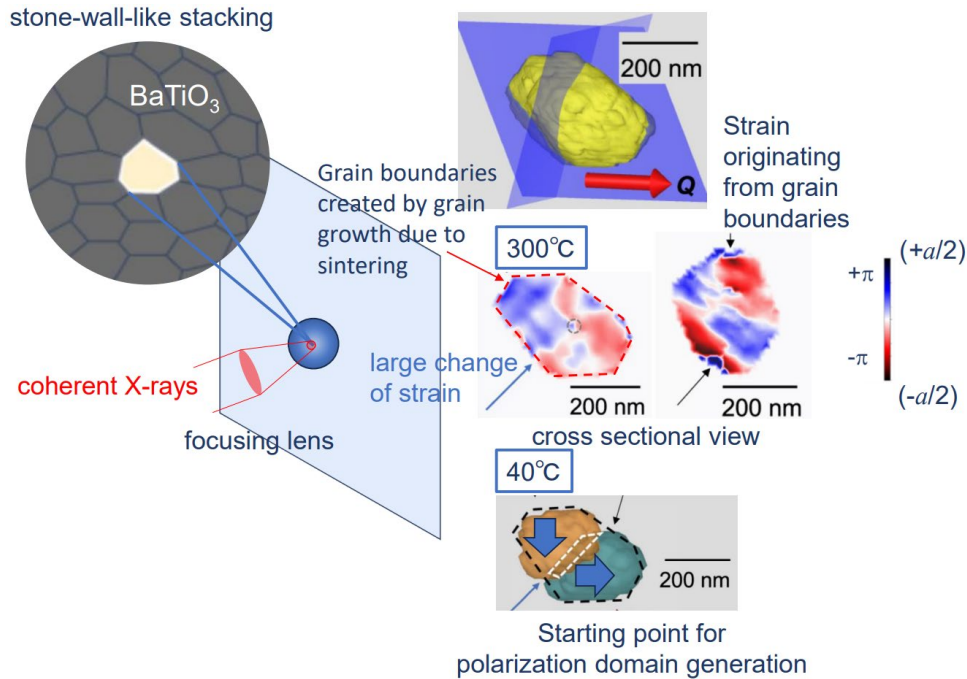


Fig. 1 3D image of 400 nm sized particles in ceramics.

BaTiO<sub>3</sub> forms domains during phase transition, and the starting point of the connection between the domains analyzed at 40 °C is the region where a large change from the red to blue regions is observed at 300 °C (slip surface). This study shows the possibility of imaging a single particle in a solid mass of several particles, including its temperature change. Additionally, the effect of grain boundaries in ceramics can be examined from the perspective of structural strain. The findings of this study are expected to provide important knowledge of the ceramics' properties, such as the ability to store more electricity and to distort greatly at low voltages.

ImageJ [14] and VESTA [15] were used in part to draw Figure 1.

### Acknowledgments

The author thanks to Dr. H. Kono (QST), Mr. T. Abe, Mr. R. Yamauchi, Prof. Y. Kuroiwa (Hiroshima Univ.), Prof. S. Ueno, Prof. I. Fujii, Prof. S. Wada (Yamanashi Univ.), Prof. R. Sato, Prof. T. Teranishi (Kyoto Univ.), Prof. M. Yamauchi (Kyushu Univ.), Dr. H. Toyokawa (JASRI) and Dr. K. Momma (NMNS) for collaboration, discussion and comments. This work was partly supported by JSPS Grant-in-Aid for Scientific Research (Grant No. JP19H05819, JP19H05625, JP22H01976, JP23H01868, JP23H04860) and the ARIM Project (Grant No. JPMXP1222

QS0017). The synchrotron X-ray scattering experiment was performed at SPring-8 with the approval of JASRI (Proposal Nos. 2021A1100, 2021B1252, 2022A1172, 2022A3761, 2022A3762, 2022A3763, 2022A3763, 2022A3784, 2022B1834, 2022B 3761, 2022B3763, 2022B3784).

### References

1. G. Arlt *et al.*, *J. Appl. Phys.* **58**, 1619 (1985).
2. K. Ishikawa *et al.*, *Phys. Rev. B* **37**, 5852 (1988).
3. T. Yamamoto *et al.*, *Jpn. J. Appl. Phys.* **32**, 4272 (1993).
4. S. Wada *et al.*, *Jpn. J. Appl. Phys.* **42**, 6188 (2003).
5. T. Hoshina, *J. Ceram. Soc. Jpn.* **121**, 156-161 (2013).
6. I. Robinson *et al.*, *Rev. Lett.* **87**, 195505 (2001).
7. I. Robinson *et al.*, *Nat. Mater.* **8**, 291 (2009).
8. K. Ohwada *et al.*, *Jpn. J. Appl. Phys.* **58**, SLLA05 (2019).
9. N. Oshime *et al.*, *Jpn. J. Appl. Phys.* **60**, SFFA07 (2021), KPSI Annual Report 2021.
10. N. Oshime *et al.*, *Jpn. J. Appl. Phys.* **61**, SN1008 (2022).
11. N. Oshime *et al.*, *Jpn. J. Appl. Phys.* **62**, SM1022 (2023).
12. T. Nishikubo *et al.*, *Chem. Mater.* **35**, 870–878 (2023).
13. K. Ohwada *et al.*, Patent application number JP,2022-125870 "Method and apparatus for X-ray diffraction measurement".
14. M. Abramoff *et al.*, *Biophotonics Int.* **11**, 36 (2004).
15. K. Momma *et al.*, *J. Appl. Crystallogr.* **44**, 1272 (2011).

# Elucidating proton disorder in the $C_1'$ phase of $H_2$ hydrate using first principles molecular dynamics

IKEDA Takashi



Hydrogen Materials Research Group, Synchrotron Radiation Research Center

First principles (FP) simulations based on density functional theory (DFT) are in principle applicable at a reasonable computational cost to any material and do not require a precise *a priori* knowledge of its structure at a given temperature and pressure, thus serving potentially as a tool to perform virtual experiments to complement the actual experimental methods. In this respect,  $H_2$  hydrate is a well-suited system for benchmarking advanced computational techniques including quantum treatment of the nuclear degrees of freedom because it can provide crystalline polymorphism at moderate pressures in the gigapascal range, while the structures of the resulting crystals are yet relatively simple. Recently, Wang *et al.* [1] suggested the presence of a new phase  $C_1'$  at a pressure of  $\sim 1.2$  GPa and temperature of  $\sim 298$  K based on Raman spectroscopy measurements. According to Wang *et al.*, proton disordering occurs in the framework of  $C_1'$  phase while maintaining the ice II-like structure, as in the well-known proton-ordered  $C_1$  phase. Thus, the  $C_1'$  phase can be viewed as a proton-disordered analog of the  $C_1$  phase. However, experimental single-crystal X-ray diffraction patterns are reportedly fitted almost equally well with the two structures within the space groups  $R\bar{3}c$  and  $R3c$  including ordered and disordered protons, respectively. Therefore, careful theoretical examinations of available experimental data, especially Raman spectra, are required to unravel the actual arrangement of protons in the  $C_1'$  phase.

To clarify the arrangement of protons in the  $C_1'$   $H_2$  hydrate, the lattice parameters and the Raman spectra of the two candidate structures for  $C_1'$   $H_2$  hydrate at 1.3 GPa and 300 K (Figs. 1(a) and (b)) are obtained using FP path-integral ring-polymer molecular dynamics (FP-RPMD) and conventional FP molecular dynamics (FP-MD). Then, the computational results of this study are compared in detail with the corresponding experimental data. For the proton-disordered  $R\bar{3}c$  system the initial configuration is prepared by selecting the orientation of each  $H_2O$  molecule constituting the framework of the  $C_1'$   $H_2$  hydrate using pseudo-

random numbers while respecting the ice rules. The cell parameters of both the proton-disordered  $R\bar{3}c$  and proton-ordered  $R3c$  systems are estimated by performing *NPT* FP-RPMD and -MD simulations and are well comparable to the experimental results when the appropriate van der Waals (vdW) corrections are employed. As shown in Fig. 2, the cell volume  $\Omega$  is largely overestimated by  $\sim 9\%$  relative to the experimental one using the conventional GGA functional of DFT (specifically revPBE in this case). By complementing the GGA functional with FP-based vdW correction (denoted as vdW-WF [3]) formulated in terms of maximally localized Wannier functions, the absolute error in the estimated value of  $\Omega$  is remarkably reduced to 0.6%.

Figure 3 shows the simulated Raman spectra of the two systems considered for this study, along with the experimental ones in the OH and  $H_2$  stretching regions taken at 1.3 GPa by Wang *et al.* [1]. Generally, the presence/absence of the inversion symmetry in the structures of a material directly affects its Raman-active vibrational modes, leading to the difference in the Raman spectra measured for different structures. However, no noticeable changes are observed in the peak frequencies of OH and  $H_2$  stretching Raman spectra computed from the FP-RPMD (-MD) trajectory for the  $R\bar{3}c$  and  $R3c$  structures as shown in Figs. 3(a) and (c) [Figs. 3(b) and (d)], respectively. Instead, the peak frequencies are significantly dependent on whether the quantum nature of nuclei is considered in generating the trajectories. Thus, the discrimination of structures leading to better agreement between the simulated Raman spectra in the stretching regions and the corresponding measured ones is difficult.

A magnified view of the lattice vibrational region in the simulated Raman spectra of the two systems considered for this study, along with the corresponding experimental results, is shown in Fig. 4. The simulated spectra well-reproduce the spectral features in the lattice mode region, located at 75, 105, and  $\sim 200$   $cm^{-1}$  in the observed spectra when the vdW corrections

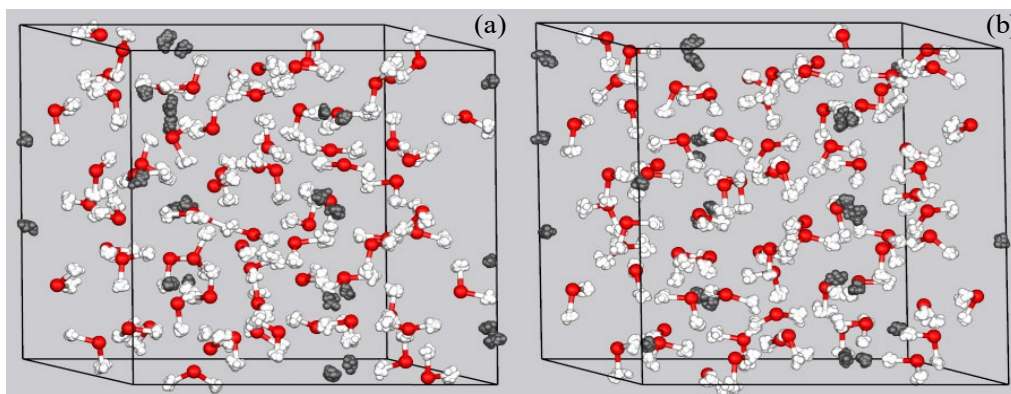


Fig. 1. Snapshots of the proton-disordered (a) and -ordered (b) systems for  $C_1'$   $H_2$  hydrate taken from our *NPT* FP-RPMD simulations performed at 1.3 GPa and 300 K [2]. The instantaneous simulation cell is shown as black solid lines. For clarity, H of  $H_2$ , H of  $H_2O$  and O of  $H_2O$  are represented by gray, white, and red balls, respectively.

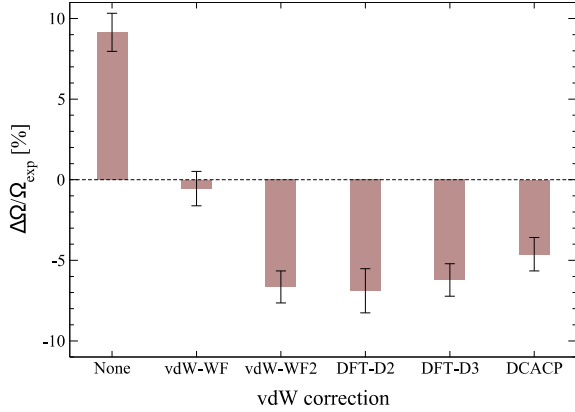


Fig. 2. Fraction (percentage) of the cell-volume difference  $\Delta\Omega$  of the proton disordered system with respect to the experimental volume  $\Omega_{\text{exp}}$  for  $C_1'$   $H_2$  hydrate obtained from *NPT* FP-MD [2] using several vdW corrections denoted as vdW-WF [3], vdW-WF2 [4], DFT-D2 [5], DFT-D3 [6], and DCACP [7].

are considered. Otherwise the frequency of the broad peak at  $\sim 200 \text{ cm}^{-1}$  is lowered by  $\sim 30 \text{ cm}^{-1}$  (plus signs in Fig. 4) compared to the experimental result. The observation is in line with the significant overestimate of the cell volume  $\Omega$  shown in Fig. 2. Furthermore, the spectra of the proton-ordered system considered in this study show a sharp peak at  $200 \text{ cm}^{-1}$  and a tiny feature at  $75 \text{ cm}^{-1}$ , contrary to the experimental results. Thus, the protons of water molecules in the  $C_1'$  phase are not ordered as in the  $R3c$  system.

### Acknowledgments

This work used the computational resources of the supercomputer Fugaku provided by RIKEN through the HPCI System Research project (Project ID: hp210223). Part of the work was conducted using the supercomputer HPE SGI8600 in the Japan Atomic Energy Agency.

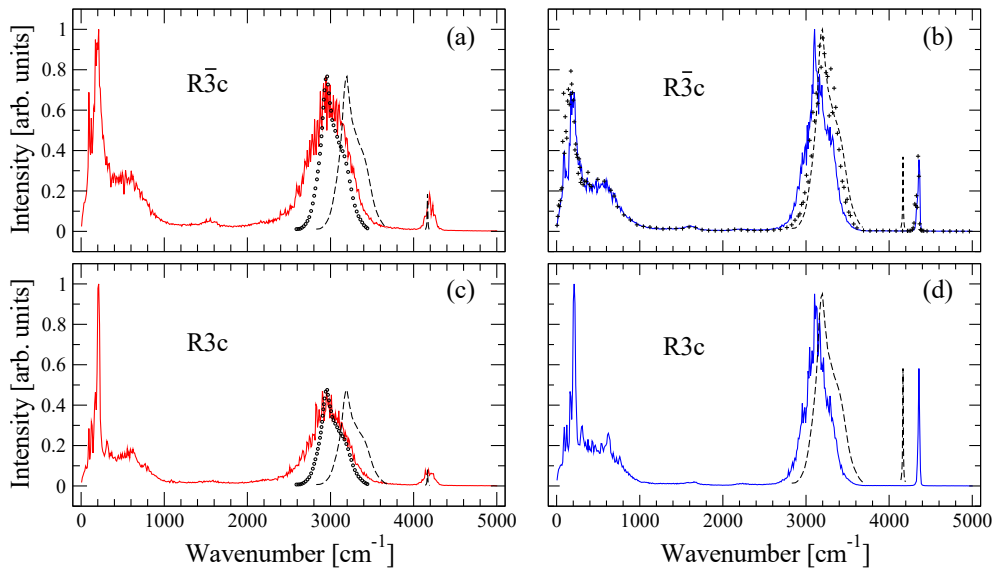


Fig. 3. Simulated Raman spectra of the proton-disordered  $R\bar{3}c$  (upper) and proton-ordered  $R3c$  (lower) systems for the  $C_1'$   $H_2$  hydrate obtained using the trajectories generated in the FP-RPMD (red lines in left) and -MD (blue lines in right) simulations of this study [2]. For comparison, the experimental Raman spectra [1] in the OH and  $H_2$  stretching regions are shown as dashed lines. Small circles in (a) and (c) represent the experimental spectrum in the OH stretching region uniformly shifted by  $-238 \text{ cm}^{-1}$ .

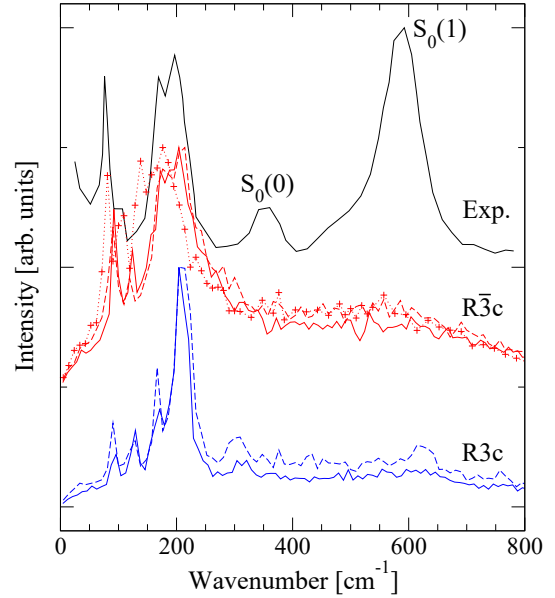


Fig. 4. Lattice vibrational region of the simulated Raman spectra obtained using the trajectories of the proton-disordered  $R\bar{3}c$  (red) and proton-ordered  $R3c$  (blue) systems generated in the considered FP-RPMD (solid) and FP-MD (dashed) simulations [2], along with the corresponding measurements for the  $C_1'$  phase by Wang *et al.* [1]. The computational result of this study obtained for the  $R\bar{3}c$  system without considering the vdW corrections in FP-MD is shown as dotted lines with plus signs.

### References

1. Y. Wang *et al.*, Phys. Rev. Lett. **125**, 255702 (2020).
2. T. Ikeda, Chem. Phys. Lett. **811**, 140252 (2023).
3. P. L. Silvestrelli, Phys. Rev. Lett. **100**, 053002 (2008).
4. A. Ambrosetti and P. L. Silvestrelli, Phys. Rev. B **85**, 073101 (2012).
5. S. Grimme, J. Comput. Chem. **27**, 1787 (2006).
6. S. Grimme *et al.*, J. Chem. Phys. **132**, 154104 (2010).
7. O. A. von Lilienfeld *et al.*, Phys. Rev. Lett. **93**, 153004 (2004).

# Observation of buried magnetic domains in grain-oriented electrical steel



INAMI Toshiya

Magnetism Research Group, Synchrotron Radiation Research Center

Grain-oriented (GO) electrical steel is a soft magnetic material characterized by high permeability and low energy loss, which is primarily used to fabricate the laminated cores of transformers. GO electrical steel is manufactured by rolling to obtain sheets of thickness ranging from 0.23 to 0.35 mm. From a crystallographic perspective, the sheets consist of highly oriented single crystals, where the sheet surface and rolling direction are parallel to the (110) plane and the [001] direction of  $\alpha$ -Fe, respectively. The crystallographic character affords an anisotropic magnetic domain structure. The basic magnetic domains in the demagnetized state are bar domains alternatingly magnetized along the [001] direction, as depicted in Fig. 1(a). In principle, the magnetization process, and thus the major magnetic properties including permeability and coercive force, are governed by the motion of  $180^\circ$  domain walls [1,2].

However, some degree of misorientation of the crystal axes relative to the sheet surface and rolling direction always exists. According to convention,  $\beta$  is defined as the angle between the [001] direction and the closest surface of the steel sheet. When  $\beta$  is sufficiently large, supplementary domains are generated to reduce the stray field energy [4], as shown in Fig. 1(a). For a slightly misoriented (110) surface, the supplementary domain is expected to consist of a pair of lancet domains connected by a transverse domain (Figs. 1(b) and (c)). The lancet domains can be observed on the surface of an electrical steel sheet and are magnetized along the [001] direction, whereas the transverse domains are expected to be magnetized along the [100] or [010] direction [1, 3, 4].

From a practical perspective, the transverse domains in GO electrical steel play a significant role. For example, transverse domains give rise to considerable magnetostriction in electrical steel sheets [3,4] because their magnetization directions are perpendicular to those of basic bar domains. Magnetostrictive deformation induced by an alternating magnetic field generates acoustic noise in transformers. Hence, reducing magnetostriction is essential for industrial applications. Additionally, the transverse domains can contribute to hysteresis loss [1,3].

However, details of transverse domains remain ambiguous because they are internal magnetic domains that have not been directly observed. Major techniques for the observation of magnetic domains, such as soft X-ray magnetic circular dichroism (MCD) microscopy and magneto-optical Kerr effect microscopy, are surface sensitive or measure magnetic domains close to the surface.

Recently, the group performing this study developed a new bulk-sensitive magnetic microscopy technique that utilizes a new magneto-optical effect in the X-ray region, referred to as X-ray magnetic circularly polarized emission (XMCPE) [5]. Currently, a lateral resolution down to 10  $\mu\text{m}$  has been achieved and a probing depth of  $\sim 40 \mu\text{m}$  is expected. In this study, XMCPE microscope is applied to visualize the buried magnetic domains in a GO electrical steel sheet [6].

XMCPE is a phenomenon in which the characteristic X-rays emitted from a magnetized specimen are circularly polarized [7]. The degree of circular polarization in the energy-resolved

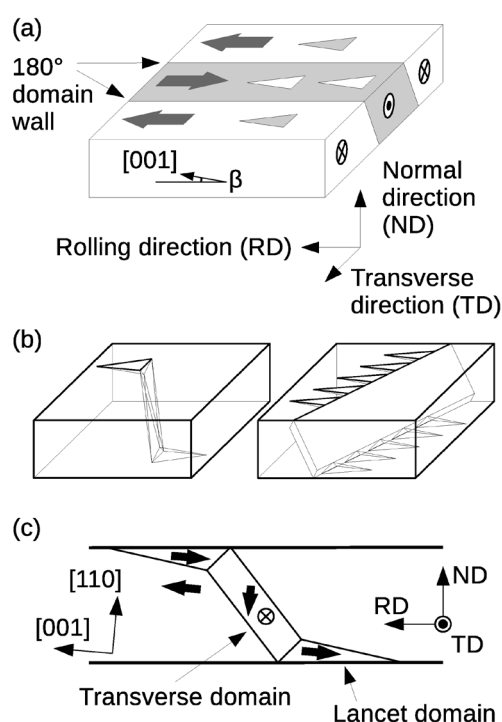


Fig.1 (a) Schematic of a GO electrical steel sheet. The large arrows indicate the direction of magnetization and the triangles on the surface represent lancet domains. (b) Perspective views of an isolated supplementary domain (left) and successively connected supplementary domains (right). (c) Side view of a supplementary domain. The lancet domains are connected by a transverse domain.

characteristic X-rays of a magnetic element is proportional to the element-selective magnetization in the emitting region parallel to the emission direction. Therefore, by measuring the degree of circular polarization of the emitted X-rays, the magnetization of the emitting position projected onto the emission direction can be estimated. A key advantage of XMCPE involves the large dichroic effect for  $K\alpha$  emissions of  $3d$  transition metals in hard X-ray regions (25 % for Fe  $K\alpha_1$  emission). Furthermore, as the energy of the excitation photons is arbitrary, high-energy incident X-rays having a long penetration length can be used.

The experiments for this study were conducted at beamline BL11XU of SPring-8. The incident X-ray energy was set to 26 keV using a Si(111) double-crystal monochromator. The incident polarization was linear and horizontal. The monochromatized X-rays were focused onto the sample using a compound refractive lens. The focal spot size was  $6 \times 8 \mu\text{m}^2$  (vertical  $\times$  horizontal). The sample was a commercial GO electrical steel sheet of 300  $\mu\text{m}$

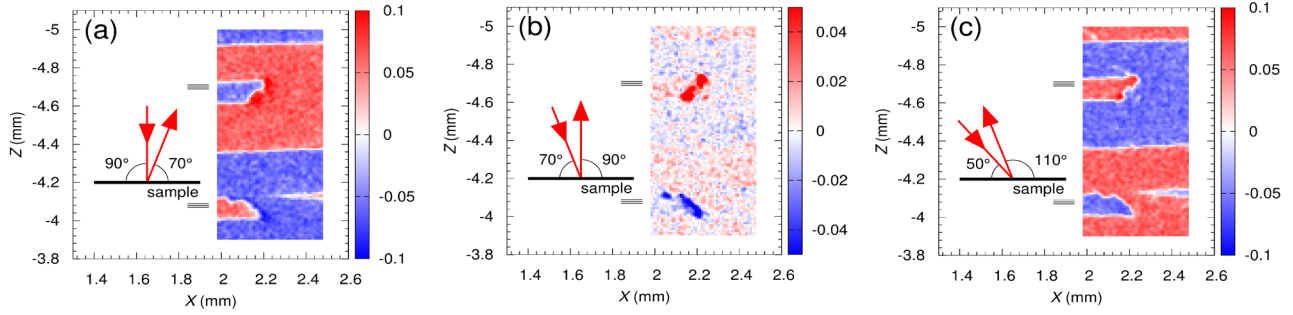


Fig. 2 Magnetic domain images measured at an incident energy of 26 keV. The color scales indicate the observed flipping ratio. The measurement geometries are also shown as insets. (a)  $\theta_{\text{in}} = 90^\circ$  and  $\theta_{\text{ex}} = 70^\circ$ . (b)  $\theta_{\text{in}} = 70^\circ$  and  $\theta_{\text{ex}} = 90^\circ$ . (c)  $\theta_{\text{in}} = 50^\circ$  and  $\theta_{\text{ex}} = 110^\circ$ .

thickness coated with a 3  $\mu\text{m}$  insulating layer, which was mounted on an XZ stage to perform a raster scan. The only magnetic element in the sample was Fe. Hence, the Fe  $K\alpha$  emission was measured. The incident angle  $\theta_{\text{in}}$  and exit angle  $\theta_{\text{ex}}$  were measured relative to the sample surface.

The characteristic X-rays divergently emitted from the sample were converted into a well-collimated beam by a Montel mirror, the center of which was positioned 200 mm downstream of the sample, followed by a phase plate and a linear polarization analyzer to evaluate the degree of circular polarization. The phase plate was a 0.5-mm-thick single-crystal diamond plate and operated near the 220 reflection, thereby functioning as a quarter-wave plate to convert the right- and left-handed circularly polarized X-rays into vertically linearly polarized X-rays by introducing phase shifts of  $+\pi/2$  and  $-\pi/2$ , respectively. The linear polarization analyzer was a Ge (400) single crystal, which was operated near the scattering angle of  $2\theta_A \approx 90^\circ$  such that the vertically linear component of the X-rays was mainly reflected. The X-ray detector was a silicon drift detector. Furthermore, the linear polarization analyzer played the role of an energy analyzer. The measurement energy was selected as 6.405 keV, corresponding to the region of maximum circular polarization in the emission spectrum.

The degree of circular polarization is equal to the flipping ratio  $(I^- - I^+) / (I^- + I^+)$  [7], where  $I^-$  and  $I^+$  denote the detected intensities for phase shifts of  $+\pi/2$  and  $-\pi/2$ , respectively. Hence, the magnetization of the emitting position projected onto the emission direction was obtained by measuring the flipping ratio. The flipping ratio was calculated at each sample position and two-dimensional magnetization images were acquired by scanning the sample with a 10  $\mu\text{m}$  step using the XZ stage.

Magnetic domain images measured at an incident energy of 26 keV are shown in Fig. 2. The exit angles are  $70^\circ$ ,  $90^\circ$ , and  $110^\circ$  for Figs. 2(a), (b), and (c), respectively. Initially, Fig. 2(a) appears to show only the bar and lancet domains. However, careful examination of the domain image reveals that the regions adjacent to the rightmost side of the lancet domains possess a deeper color, indicating enhanced contrast for the magnetization component perpendicular to the sheet plane. This tendency is readily apparent in Fig. 2(b), where only the magnetization component perpendicular to the sheet plane is observed. Therefore, the spot-like domains observed in Fig. 2(b) should

possess substantial magnetization perpendicular to the sheet plane. Hence, the domains can be concluded as transverse domains. Upon further increasing  $\theta_{\text{ex}}$  to  $110^\circ$  to obtain Fig. 2(c), the red and blue contrast is reversed relative to that in Fig. 2(a), while the color of the transverse domains remains unchanged.

Notably, the observed supplementary domains are neither isolated supplementary domains, as shown on the left side of Fig. 1(b), nor successively connected supplementary domains, referred to as lancet combs, as shown on the right side of Fig. 1(b). A single lancet domain is evidently connected to several transverse domains. The lancet domain at  $Z \approx -4.06$  is connected to a small transverse domain at  $Z = -4.1$  and a large transverse domain at  $Z \approx -4.06$ . In addition, the large domain appears to consist of two mutually connected transverse domains. Similarly, the transverse domain at  $Z \approx -4.68$  comprises two transverse domains ( $Z = -4.64$  and  $-4.72$ ). Thus, two or more supplementary domains appear joined to afford the observed complicated supplementary domain. Furthermore, the transverse domain at  $Z \approx -4.06$  is elongated along one direction. The lancets join to form combs when  $\beta$  is relatively large. Simultaneously, the transverse domains are assumed to connect with each other in a line to afford a plate. The observed elongated domain may be a short variation of such a transverse plate.

In this study, the buried magnetic domains in a GO electrical steel sheet are successfully visualized by XMCPPE microscopy using high-energy incident X-rays to enhance the bulk sensitivity. The internal transverse domains are unambiguously and directly observed. The shapes of the transverse domains are considerably different from those expected, thus demonstrating the importance of direct experimental observations.

## References

1. D. Küppers et al., J. Appl. Phys. **39**, 608 (1968).
2. T. Nozawa et al., IEEE Trans. Mag. **32**, 572 (1996).
3. A. Hubert and R Schäfer, "Magnetic Domains. The Analysis of Magnetic Microstructures", Berlin, Springer-Verlag, (1998).
4. M. Imamura et al., IEEE Trans. Mag. **17**, 2479 (1981).
5. K. Sugawara et al., J. Appl. Phys. **130**, 113901, (2021).
6. T. Inami et al., IEEE Trans. Mag. **59**, 6000406 (2023).
7. T. Inami. Phys. Rev. Lett. **119**, 137203 (2017).

# Theoretical study of the time-resolved magnetic excitation in a photoexcited Mott insulator

TSUTSUI Kenji



Advanced Spectroscopy Research Group, Synchrotron Radiation Research Center

The ultrafast dynamics of strongly correlated electron systems by photoirradiation are attracting significant attention. The femtosecond pump-probe spectroscopy to correlated electron systems can observe exotic photo-induced phase transitions including a photo-induced insulator-to-metal transition. The suppression of absorption spectral weights across the Mott gap and the appearance of the weights inside the Mott gap in optical conductivity are indications of a photo-induced insulator-to-metal transition. In addition to the charge channel, the spin channel can also produce characteristic changes. A decrease in spectral weights in single-magnon dispersion by photoirradiation has been observed in time-resolved resonant inelastic X-ray scattering (trRIXS) on iridate antiferromagnetic Mott insulators [1,2]. Time-resolved two-magnon Raman scattering (trTMR) on an antiferromagnetic Mott insulator  $\text{YBa}_2\text{Cu}_3\text{O}_{6.1}$  has shown a decrease in spectral weight during the two-magnon excitation [3]. Such decreases are understood as an emergence of photoexcited electronic states, which reduce the antiferromagnetic spin correlation [4]. An arising question is whether low-energy magnetic excitations below the magnon energy appear in the spin channel. Moreover, trTMR experiments have reported an increase in low-energy spectral weights below the two-magnon energy for photo-irradiated  $\text{YBa}_2\text{Cu}_3\text{O}_{6.1}$  [3]. As photo-irradiation of Mott insulators drastically changes the electronic states observed in the charge channel, the spin channel is expected to induce low-energy excitations below magnon energies.

In this study, photo-induced low-energy magnetic excitations below the single- and two-magnon energies in a photoexcited Mott insulator on a square lattice are theoretically examined [5,6]. Using a numerically exact-diagonalization technique for a photoexcited half-filled Hubbard model on a square lattice, low-energy magnetic excitations are found to be induced by a pump pulse, whose intensity is maximized when the frequency of the pulse is tuned to the absorption edge. By analyzing low-energy magnetic excitation using point-group symmetry for the square lattice, the photo-induced low-energy signals are known to be predominantly created by photoexcited states with  $E$  presentation of the  $C_{4v}$  point group at the absorption edge. The proposed photo-induced magnetic excitations provide one of the possible origins of low-energy weight in the trTMR spectrum.

To describe Mott insulating states on a square lattice, a single-band Hubbard Hamiltonian  $H_0$  is considered on a square lattice at half filling including the nearest-neighbor ( $t_h$ ) and on-site Coulomb interaction ( $U$ ) term. Furthermore,  $U/t_h = 10$  with  $t_h \sim 0.35$  eV are considered typical parameter values in cuprates. Herein,  $t_h = 1$  is used as an energy unit and  $1/t_h$  as a time unit. An external spatially homogeneous electric field, applied along the  $x$  direction with the Peierls phase substitution in the hopping terms leading to the time-dependent Hamiltonian  $H(t)$ , is incorporated. The vector potential  $A(t) = A_0 \exp[-(t-t_0)/(2t_d^2)] \cos[\omega_p(t-t_0)]$  is introduced in the phase, where a Gaussian-like envelop centered at  $t_0$  has a temporal width  $t_d$  and a central

frequency  $\omega_p$ . Additionally,  $A_0 = 0.5$ ,  $t_0 = 0$ , and  $t_d = 0.5$  are set.

For calculations of time-resolved spin excitation after pumping, it is convenient to use the spectral representation of dynamical correlation functions regarding  $|\psi(t)\rangle$  as an initial state, which is easily formulated for the system without time-dependent terms in the Hamiltonian. Applying this formalism to a time region after turning off the pump pulse,  $t > t_{\text{off}}$ , where the Hamiltonian is time independent, the time-resolved dynamical spin susceptibility  $S(\mathbf{q}, \omega; t)$  with momentum  $\mathbf{q}$  and frequency  $\omega$ , and the trTMR susceptibility  $M(\omega; t)$  are obtained [6,8].

First, the results of dynamical spin susceptibility,  $S(\mathbf{q}, \omega; t)$ , which can describe the photoinduced low energy magnetic excitations below the single-magnon dispersion energy, are discussed [5,6]. For a  $4 \times 4$  lattice,  $\mathbf{q} = (\pi, 0)$  and  $(0, \pi)$ , where the energy of a single magnon is maximized. Figures 1a and b show the pumping frequency  $\omega_p$  dependence of  $S(\mathbf{q}, \omega; t = 4)$  at  $\mathbf{q} = (\pi, 0)$  and  $(0, \pi)$ , respectively. At a high pumping frequency  $\omega_p = 20 > U$ , the peak intensity is larger and smaller than that before pumping (dotted lines), as shown in Fig. 1a and b, respectively. The  $\mathbf{q}$ -dependent intensity at a given  $t$  is a consequence of the antiphase oscillation of time-dependent spin structure factors in a photoexcited Mott insulator on a square lattice [5,7,8]. With decreasing  $\omega_p$ , the peak intensity decreases and reaches a minimum at  $\omega_p = 10$ , where the energy absorbed by pumping in the system is the largest, leading to a reduction of the antiferromagnetic spin correlation. With a further decrease in  $\omega_p$ , the peak intensity increases.

At  $\omega_p = 6$ , which corresponds to the absorption peak energy at the Mott-gap edge, a hump structure is observed at  $\omega \sim 0.2$  below the peak energy for  $\mathbf{q} = (\pi, 0)$  in Fig. 1a. The observation is attributed to a photoinduced low-energy magnetic excitation. Notably, the hump structure loses its weight away from  $\omega_p = 6$ . Moreover, no hump structure is observed at  $\mathbf{q} = (0, \pi)$  in Fig. 1b. Thus, the anisotropic hump structure is expected in the trRIXS of

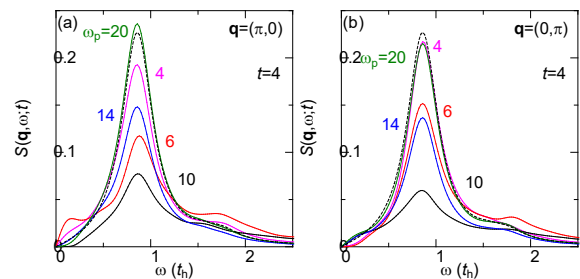


Fig. 1 Pumping frequency dependence of time-resolved dynamical spin susceptibility after pumping for the half-filled  $4 \times 4$  Hubbard model. (a) Momentum  $\mathbf{q} = (\pi, 0)$  and (b)  $(0, \pi)$  at  $t = 4$ . The dashed black lines represent the results before pumping, whereas the purple, red, black, and green solid lines represent the results at  $\omega_p = 4, 6, 10, 14$ , and  $20$ , respectively.

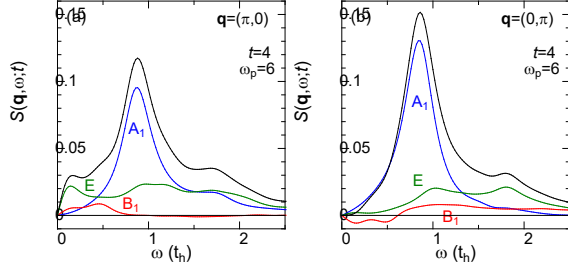


Fig. 2 Symmetry decomposition of the time-resolved dynamical spin susceptibility. (a) Momentum  $\mathbf{q} = (\pi, 0)$  and (b)  $(0, \pi)$  with  $\omega_p = 6$  at  $t = 4$ . The blue, red and green solid lines represent the contributions of  $A_1$ ,  $B_1$ , and  $E$  of the  $C_{4v}$  point group, respectively. The black solid lines represent the sums of these contributions, which are the same as the red lines in Fig. 1, respectively.

insulating cuprates and iridates on square lattices when a pump pulse is tuned to a Mott-gap edge.

To understand the origin of the hump structure at  $\omega_p = 6$ ,  $S(\mathbf{q} = (\pi, 0), \omega; t = 4)$  is decomposed into several contributions [5,8]. The wave function  $|\psi(t)\rangle$  for  $t > t_{\text{off}}$  has three components classified by irreducible representations,  $A_1$ ,  $B_1$ , and  $E$ , of the square lattice with the  $C_{4v}$  point group. Note that the  $A_1$  and  $B_1$  representations correspond to  $s$  and  $d(x^2-y^2)$  waves, respectively. The  $E$  representation corresponds to a  $p_x$  wave and agrees with optically allowed single-photon absorbed states created by an electric field along the  $x$  direction. Figures 2a and b show the three contributions to  $S(\mathbf{q} = (\pi, 0), \omega; t = 4)$  and  $S(\mathbf{q} = (0, \pi), \omega; t = 4)$ , respectively. The magnon peak at  $\omega \sim 0.8$  consists mainly of the  $A_1$  component because of the dominant ground-state contribution in the  $A_1$  state. However, for the hump structure observed at  $\omega \sim 0.2$  in  $S(\mathbf{q} = (\pi, 0), \omega; t)$  in Fig. 2a, the  $E$  component has the largest contribution. Thus, this component corresponds to the excitation from a single-photon absorbed state at the Mott gap edge [6].

Figure 3a shows the  $\omega_p$  dependence of time-resolved two-magnon Raman susceptibility  $M(\omega; t = 4)$ . The peak-intensity variation relative to  $\omega_p$  is similar to that for the single-magnon intensity shown in Fig. 1. When  $\omega_p = 6$ , an enhancement in the low-energy spectral weight, at  $\omega \sim 0.4$  is observed, which is similar to the enhancement of the low-energy weight in  $S(\mathbf{q} = (\pi, 0), \omega; t)$  shown in Fig. 1a, although its energy is nearly half of  $\omega \sim 0.4$ . The similarity suggests the same origin for these enhancements. To identify the symmetry components that contribute to the enhancement in trTMR, the spectral weight is decomposed into several components characterized by irreducible representations, as shown in Fig. 3b. Similar to  $S(\mathbf{q} = (\pi, 0), \omega; t)$ , the low-energy part of  $M(\omega; t)$  originates from the  $E$  component, as shown in Fig. 3b. Then, the  $E$  component and those in  $S(\mathbf{q} = (\pi, 0), \omega; t)$  are found to correspond to the magnetic excitation from a single-photon absorbed state at the Mott-gap edge [6]. Thus, this photo-induced excitation can explain the increase of the low-energy spectral weight in the trTMR experiment.

In summary, low-energy magnetic excitations below single- and two-magnon energies in a photoexcited Mott insulator on a square lattice have been discussed theoretically [5,6]. The intensity of the low-energy magnetic excitations is maximized when the frequency of the pulse is tuned to the absorption edge and optically allowed states with the  $E$  presentation of the  $C_{4v}$

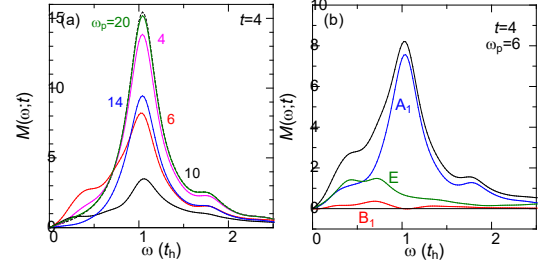


Fig. 3 Pumping frequency dependence of time-resolved two-magnon Raman susceptibility after pumping and the symmetry decomposition. Time  $t = 4$ . (a) Dashed black line represents the results before pumping. The purple, red, black, blue, and green solid lines represent the results with  $\omega_p = 4, 6, 10, 14, 20$ , respectively. (b) Symmetry decomposition of  $M(\omega; t = 4)$  with  $\omega_p = 6$ . The blue, red and green solid lines represent the contributions of  $A_1$ ,  $B_1$ , and  $E$  of the  $C_{4v}$  point group, respectively. The black solid lines represent the sum of these contributions, which is the same as the red line in Fig.3a.

point group are excited. The photo-induced low-energy magnetic excitations agree with the increase in the low-energy spectral weight in the trTMR experiment. Thus, the theoretical prediction can be confirmed when the pumping frequency is varied in the trTMR and trRIXS experiments for insulating cuprates and iridates.

## Collaborators

Takami Tohyama

Department of Applied Physics, Tokyo University of Science

Kazuya Shinjo

Computational Quantum Matter Research Team, RIKEN Center for Emergent Matter Science (CEMS)

Shigetoshi Sota

Computational Materials Science Research Team, RIKEN Center for Computational Science (R-CCS)

## Acknowledgments

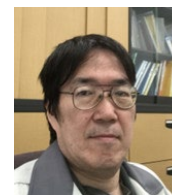
This work was supported by the Japan Science and Technology Agency, by the Japan Society for the Promotion of Science, KAKENHI (21H03455, 22K03500) from Ministry of Education, Culture, Sports, Science, and Technology (MEXT), Japan. Part of the numerical calculation was carried out using the supercomputing facilities in QST.

## References

1. M. P. M. Dean *et al.*, Nat. Mater. **15** 601 (2016).
2. D. G. Mazzone *et al.*, Proc. Nat. Acad. Sci. USA **118** e2103696118 (2021).
3. J.-A. Yang *et al.*, Nat. Commun. **11** 2548 (2020).
4. J. H. Mentink, J. Phys. Condens. Matter **23** 453001 (2017) and references therein.
5. K. Tsutsui, K. Shinjo, and T. Tohyama, JPS Conf. Proc. **38** 011159 (2023).
6. K. Tsutsui, K. Shinjo, S. Sota, and T. Tohyama, Commun. Phys. **6** 41 (2023)
7. T. Tohyama, K. Shinjo, S. Sota, and K. Tsutsui, Journal of Physics: Conf. Series **2207** 012028 (2022).
8. K. Tsutsui, K. Shinjo, and T. Tohyama, Phys. Rev. Lett. **126** 127404 (2021).

# Research Activities at the Institute of Quantum Life Science at KPSI

SHIKAZONO Naoya



Institute for Quantum Life Sciences

Quantum life science has emerged to explore new frontiers in biology from the perspective of dynamics and functions of cellular processes at the quantum level. The Institute for Quantum Life Science at the National Institutes for Quantum Science and Technology (QST) was established in April 2019 to pioneer a new field in life sciences. Investigations at the Institute for Quantum Life Science are expected to follow two approaches. The first approach is to determine whether quantum mechanics plays an essential role in biological systems. The second approach is to apply quantum science and its technologies for measuring physical and chemical parameters (such as temperature, pressure, and pH) inside a cell at an unprecedented minute level to gain information on the structure and dynamics of biomolecules. Using the aforementioned two approaches, the goal of the Institute for Quantum Life Science is to discover the essential principles of life and apply the knowledge attained during investigations to medical sciences and social activities (Fig. 1). The field of quantum life science is envisaged to produce unanticipated discoveries that can expose the existence of quantum phenomena in nature, ultimately leading to their exploitation, which is expected to benefit our society. At the Kansai Institute for Photon Science, three research teams with the Institute of Quantum Life Science are conducting research using experiments and computer simulations (Fig. 1).

The Molecular Modeling and Simulation Team aims to understand the *in-vivo* function of biomolecules at the atomic level. The team uses computer simulations and bioinformatics based on experimental results such as crystallographic and scattering data obtained using various types of radiation (X-rays, neutrons, and electrons) and cryo-electron microscopy. The main objective of their study is to determine how the dynamics of protein/DNA/RNA complexes relate to essential cellular functions including transcription, translation, replication, and repair. Currently, the team is attempting to quantitatively predict the dynamics and stability of supramolecular complexes such as chromosomes. Recently, the research team conducted simulations to elucidate the overall structure of the circadian clock complex, which produces an oscillation that repeats roughly every 24 h and is considered to be the basis of rhythmic cellular activities. The circadian clock in cyanobacteria has been well characterized and is known to be constituted of three proteins, KaiA, KaiB, and KaiC. These proteins undergo an association–dissociation cycle coupled with the phosphorylation–dephosphorylation oscillation of KaiC. During the circadian cycle, the Kai-clock system generates three forms of complex, two binary KaiAC and KaiBC complexes, and one ternary KaiABC complex, at specific phases. The KaiABC complex is known to be critical in switching from positive to negative feedback in both KaiC phosphorylation and complex formation cycles. However, the mechanism of the KaiABC complex regulating the switching process is unknown. To gain insights into this process, the team aimed to solve the overall structure of the KaiABC complex. Previously, a cryo-electron

microscopy (EM) study was conducted to determine the supramolecular architecture of the complex, but it fell short of determining the N-terminal domain of the KaiA protein. Using the overall structural information of the circadian clock complex in the solution provided by small-angle X-ray and neutron scattering, the group attempted to elucidate the overall structure with computational analysis. Computationally built 20 million structural models of the complex were screened out, and subsequently subjected to molecular dynamics simulations to examine their stabilities. From the selected model, it was suggested that, despite the large fluctuation of the KaiA N-terminal domains, their preferential positionings mask the hydrophobic surface of the KaiA C-terminal domains, which hinder additional KaiA-KaiC interactions. The results provide important insights into how the circadian complex proceeds along the phases that generate the circadian rhythm.

The main goal of the DNA Damage Chemistry Team is to clarify the nature of DNA damage induced by various agents, particularly ionizing radiation. The team aims to utilize new experimental techniques that can reveal the structure and/or spatial distribution of DNA damage at the nanometer scale. Currently, the team focuses on “clustered DNA damage,” in which two or more DNA lesions are located within one to two helical turns of DNA (within several nanometers of the DNA). Repair of clustered DNA damage is considered to be challenging; thus, it is potentially a detrimental type of damage induced by ionizing radiation. However, its presence and microstructure remain elusive, as few experimental methods have obtained data on the spatial distribution of DNA lesions. The research team has established a novel approach for detecting the level of DNA damage localization through direct visualization. Atomic force microscopy (AFM) has a resolution at the nanometer/sub-nanometer scale; thus, DNA can be directly visualized. The team labeled DNA damage (abasic sites) by attaching aldehyde reactive probes with biotin to abasic sites and then attaching streptavidin to biotin. The large molecular size of streptavidin enabled the detection of the site of damage using AFM. Abasic sites were directly induced or further revealed by removing the damaged bases by DNA glycosylases after irradiation. Using the proposed method, the complex nature of clustered DNA damage was visualized. They found that various types of clustered DNA damage were generated: clusters that contained two base lesions, more than two base lesions, and double-strand breaks (DSBs) that accompanied base lesions. They further verified that the repair of clustered DNA damage was compromised. X-ray-induced clusters with more than two base lesions could be repaired, but the repair rate was slightly lower than that of other types of clustered DNA damage and was significantly lower than that of isolated base damage. Fe-ion-induced clusters with base damages could also be repaired, but their repair rates were lower than those with isolated base damage. The repair of Fe-ion-induced DSBs with base damage was markedly retarded. Surprisingly, the number of DSBs increased after 1 h of incubation, following which they decreased slowly. The research team further

## Institute of Quantum Life Science

Using cutting-edge quantum technologies and advanced computer simulations, the Institute aims to contribute to the (1) elucidation of the basic principles of life, and in longer term, (2) improving the everyday life of the society.

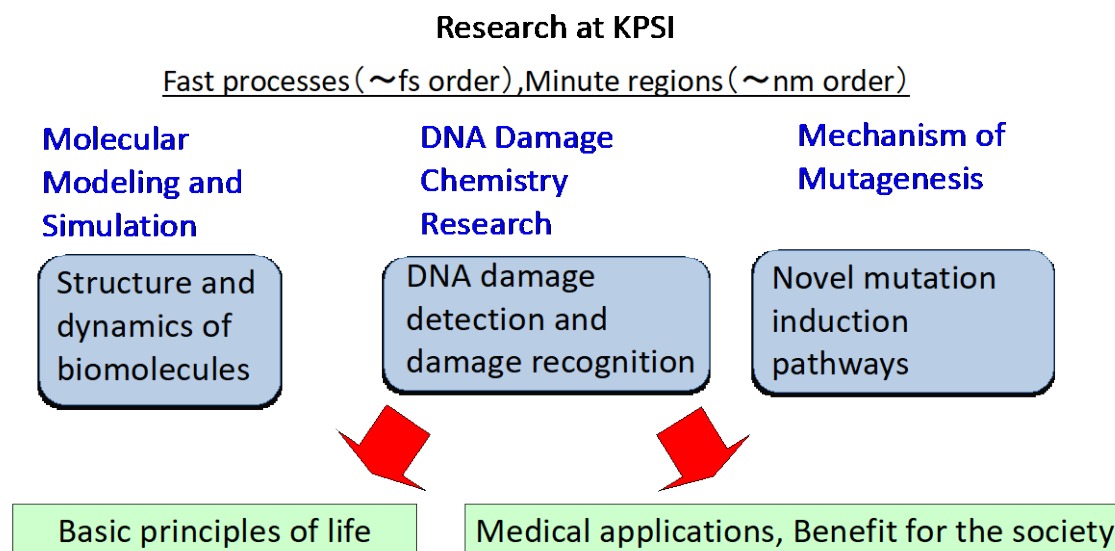


Figure 1.

developed a promising method to detect clustered DNA damage using fluorescence resonance energy transfer (FRET). In this method, aldehyde/ketone moieties such as those at the abasic sites in irradiated DNA were labeled by aminooxyl fluorophores. Fluorescence anisotropy facilitated the estimation of the apparent base-pair separations between lesions in a cluster produced by an ion track and revealed that clustered abasic sites were generated by ionizing radiation [1]. They detected clustered lesions in DNA that were irradiated under cell mimetic radical-scavenging conditions. A detailed description is provided in the following report. Both AFM and FRET approaches confirmed that these novel analyses had the potential to discover qualitative and quantitative differences in clustered DNA damage produced by various types of ionizing radiation.

The Mechanism of Mutagenesis Team aims to elucidate the underlying mechanisms causing mutations, which are highly relevant to carcinogenesis and the evolution of life. One aspect of the team's research focuses on events at very early stages (around a femtosecond to picosecond), within a space in the scale of nanometers, after energy transfer from ionizing radiation, particularly ion particles. Using Monte Carlo simulations, the research team demonstrated that when water was exposed to densely ionizing ion particles, some of the secondary electrons ejected from the water molecules were trapped within the electric potential created by the ionized water molecules. The result led to the realization that the radial dose near the track of a densely ionizing ion particle was much higher than that previously considered. The highly localized energy deposition is likely to produce a high yield of clustered DNA damage and thus, has important implications regarding the drastic effect of ion particles on cells. Another study that interests the team focuses on whether proton transfer, or more specifically proton tunneling, has a role in mutagenesis. A hypothesis that proton transfer may play an important role in mutagenesis was proposed more than 70 years

ago. Lowdin took it a step further that the transfer could occur via a quantum effect, which is known as proton tunneling. To study the importance of proton transfer in mutagenesis, the team took an approach to substitute hydrogens with deuteriums in cells. Although the chemical properties of hydrogens and deuteriums are similar, deuterium has a proton and a neutron in the nucleus, and the mass is as twice as large compared with hydrogen. This difference often leads to a change in reaction rates between substrates that contain hydrogens and that contain deuteriums. The team has found that substituting hydrogen with deuteriums slows down the initial growth of bacterial cultures. Interestingly, they observed an increase in mutation frequency when deuteriums are present. The reason why mutagenesis is stimulated by the presence of deuteriums is currently unknown. The team is now examining the mutation frequency at the DNA level with the DNA synthesized *in vitro*.

Quantum life science is related to the interactions between dynamical phenomena at extremely short time scales and minute length scales; from atto to femtosecond energy transfer processes at the (sub)nanometer scale. Over the long term, the field of quantum life science is expected to produce unparalleled discoveries based on the significance of quantum phenomena in biological systems. To achieve such goals, the research of the three teams of the Institute of Quantum Life Sciences at KPSI is ongoing.

### References

1. Akamatsu, K., Satoh, K., Shikazono, N., and Saito, T. Proximity estimation and quantification of ionizing radiation-induced DNA lesions in aqueous media using fluorescence spectroscopy. *Radiation Res.* 201, 150-159 (2024)

# Quantification and proximity estimation of ionizing radiation-induced DNA damage using fluorescence spectroscopy



AKAMATSU Ken

DNA Damage Chemistry Team, Institute for Quantum Life Science

A clustered DNA damage site (cluster), where two or more lesions exist within a few helical turns, is believed to be a key factor in determining the fate of a living cell exposed to a DNA-damaging agent including ionizing radiation. However, the structural details of clusters, such as the number of included lesions and their proximity, are unknown. In this study, a method is developed to characterize clusters by fluorescence anisotropy measurements based on Förster resonance energy transfer (homo-FRET) (Fig. 1).

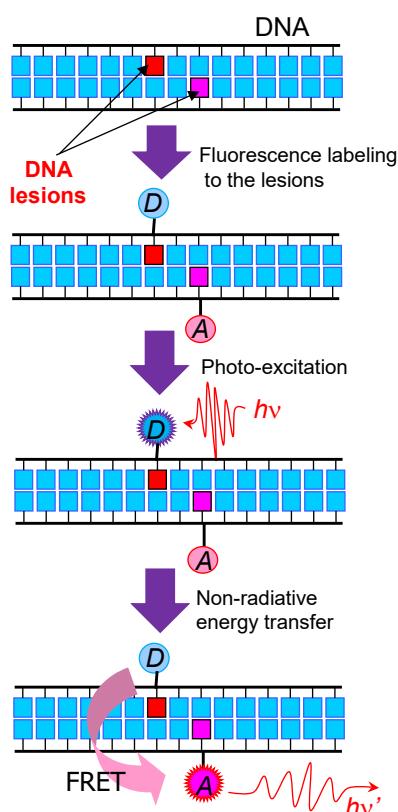
FRET has been used in molecular and cell biology to investigate the interaction between biomolecules as a “nanometer ruler”. Furthermore, FRET is applied to visualize clusters in living cells. There are generally two categories of FRET: hetero-FRET and homo-FRET. Hetero- and homo-FRET can evaluate

the energy transfer phenomena between structurally different molecules (a “donor” – “acceptor” ( $D-A$ ) pair) and the same dye molecules, respectively.

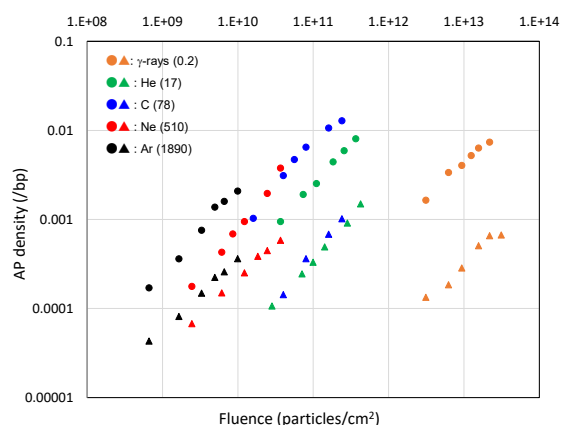
In our previous report, the hetero-FRET method is known to estimate the localization of abasic sites (APs) by fluorescence spectroscopy of a labeled plasmid sample solution [1,2]. However, the sensitivity is insufficient, in principle, particularly because all the clustered APs cannot be labeled with a  $D-A$  pair (such as a clustered AP labeled with a  $D-D$  or  $A-A$  pair is not detected as a cluster). Homo-FRET is attempted to compensate for the aforementioned disadvantage [3], as the homo-FRET method is better suited than hetero-FRET due to its sensitivity and simple experimental protocol. However, the efficiency of the method should be estimated by fluorescence anisotropy as the fluorescence intensities with and without FRET for a given emission wavelength are equal. The homo-FRET method has been applied to estimate AP localization in a plasmid DNA irradiated with helium and carbon ion beams in a solid state [4]. The study reveals that the possibility of cluster formation increases with linear energy transfer (LET). This study demonstrates the homo-FRET (fluorescence anisotropy) results of DNA irradiated by helium, carbon, neon, argon ion beams (i.e.,  ${}^4\text{He}^{2+}$ ,  ${}^{12}\text{C}^{6+}$ ,  ${}^{20}\text{Ne}^{8+}$ ,  ${}^{40}\text{Ar}^{13+}$ ), and  ${}^{60}\text{Co}$   $\gamma$ -rays in water and in 0.2 M Tris-HCl (pH 7.5), which has a radical scavenging capacity similar to that in a cell nucleus [5]. The radiations enable the study of LET dependence of DNA damage spectra, ranging from LET of  $10^{-1}$  to  $10^3$  keV/ $\mu\text{m}$ .

Figure 2 shows the average AP density (number of APs per base pair) as a function of fluence (particles/ $\text{cm}^2$ ). These results indicate that the dose-response is almost linear for all radiation sources and that the AP densities without the buffer were almost one order of magnitude larger than those with the buffer for each radiation source. This finding suggests that free radicals such as hydroxyl radical ( $\bullet\text{OH}$ ), hydrogen radical ( $\bullet\text{H}$ ), and hydrated electrons, that cause AP generation, are scavenged by Tris. Moreover, interestingly, the AP density ratio of Tris to water for Ne and Ar seems to be smaller than those for the other radiations. This implies that the high-LET sources are likely to ionize DNA molecules directly. Therefore, the chemical structures of the lesions formed by a high-LET source could be different from those of a low-LET one.

Figure 3 shows fluorescence anisotropy of irradiated DNA in water and Tris for the various radiations as a function of AP density. Regardless of the presence or absence of the Tris buffer, the anisotropy values generally decrease with increasing AP density. The decrease results from a sequentially-produced cluster due to overlapping two or more radiation tracks. It is noted that the values for all the radiations are significantly lower than those for heat-in-acid treated DNA with randomly-distributed APs, implying that low-energy electrons likely induce the clusters. Another possible reason for the difference may be the difference in the chemical structure of damaged sites such as an AP. Due to



**Fig. 1.** Strategy for estimating the localization of DNA lesions using FRET.  $D$  and  $A$  are “donor” and “acceptor” fluorescent probes, respectively. When  $D$  and  $A$  are the same, the FRET is referred to as “homo-FRET”. When  $D$  and  $A$  are different, it is referred to as “hetero-FRET”.



**Fig. 2.** Relationship between AP density and particle fluence for irradiated DNA dissolved in water and in 0.2 M Tris-HCl (10 mg DNA/mL). Although  $\gamma$ -rays are not “particle”, the apparent fluence of those were obtained using each of LET values. Each number in the parentheses represents the LET.

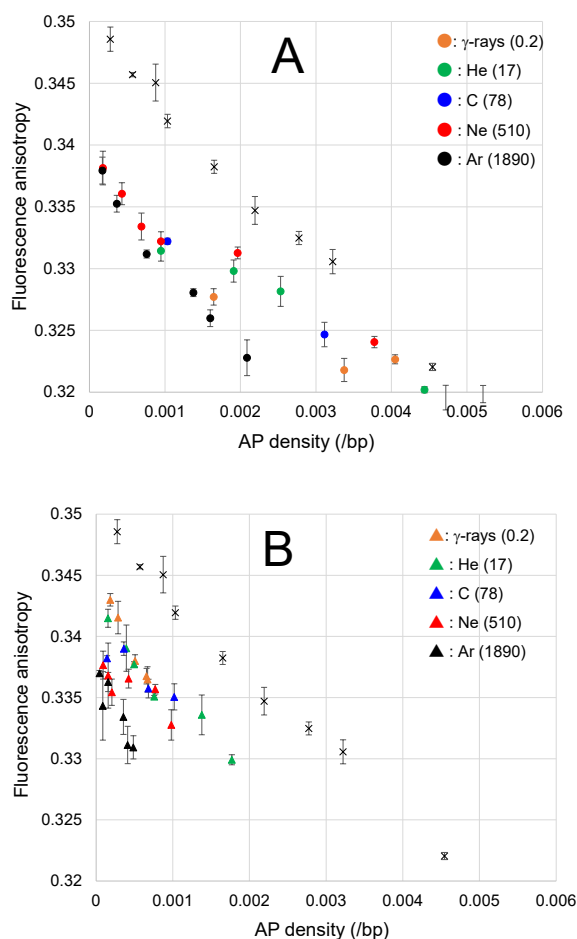


**Fig. 3.** Relationship between AP density and particle fluence for irradiated DNA dissolved in water (Panel A) and in 0.2 M Tris-HCl (Panel B). Although  $\gamma$ -rays are not “particle”, the apparent fluence of those were obtained using each of LET values. The cross marks represent the data for DNA treated in citrate buffer (pH 5) at 70°C.

the heat incubation, DNA is known to be depurinated by hydrolysis to produce a typical AP, with an aldehyde moiety at C1' of the sugar. In contrast, irradiation to the DNA solutions would produce a variety of electrophilic carbonyl groups that are reactive with an aminoxy fluorescent dye used as well as the typical AP. Furthermore, interestingly, no LET dependence of the anisotropy was found in the case of irradiation in water, whereas the anisotropy seems to slightly decrease with the increase of LET. This finding demonstrates that direct energy transfer from the radiation to DNA molecule causes a cluster DNA damage formation by a single radiation track.

## Acknowledgments

The author thanks Drs. Naoya Shikazono, Katsuya Satoh, and Takeshi Saito for supporting the overall experiments and  $\gamma$ -irradiation at the Institute for Integrated Radiation and Nuclear Science, Kyoto University. This work was supported by Grants-in-Aid for Scientific Research (for Scientific Research (C): 16K00551) from the Ministry of Education, Culture, Sports, Science, and Technology of Japan.

## References

1. Akamatsu K, Shikazono N. A methodology for estimating localization of apurinic/aprimidinic sites in DNA using fluorescence Resonance Energy Transfer. *Anal. Biochem.* 2013;433:171-180.
2. Akamatsu K, Shikazono N, Saito T. Localization estimation of ionizing radiation-induced abasic sites in DNA in the solid state using fluorescence Resonance Energy Transfer. *Radiat. Res.* 2015;183:105-113.
3. Akamatsu K, Shikazono N, Saito T. New method for estimating clustering of DNA lesions induced by physical/chemical mutagens using fluorescence anisotropy. *Anal. Biochem.* 2017;536:78-89.
4. Akamatsu K, Shikazono N, Saito T. Fluorescence anisotropy study of radiation-induced DNA damage clustering based on FRET. *Anal. Bioanal. Chem.* 2021;413:1185-1192.
5. Akamatsu K, Satoh, K., Shikazono N, Saito T. Proximity estimation of ionizing radiation-induced DNA lesions in aqueous media using fluorescence spectroscopy. *Radiat. Res.* 2024;201:150-159.



# Publication Lists

# Original Papers

## 1. Weakened Oxygen Adsorbing the Pt–O Bond of the Pt Catalyst Induced by Vacancy Introduction into Carbon Support.

Okazaki Hiroyuki, Idesaki Akira, Koshikawa Hiroshi, Ikeda Takashi, Yamamoto Shunya, Yamaki Tetsuya, Daiju Matsumura, *The Journal of Physical Chemistry C*, 127(49), 23628 - 23633, 2023, DOI:10.1021/acs.jpcc.3c04117

## 2. Design of soft x-ray varied-line-spacing (VLS) high-dispersion laminar-type grating coated with super-mirror-type (SMT) multilayer for flat-field spectrograph in a region of 2-4 keV.

Koike Masato, Hatano Tadashi, Alexander Pirozhkov, Ueno Yoshio, Terauchi Masami, *Review of Scientific Instruments*, 95, 023102, 2024, DOI:10.1063/5.0173068

## 3. Laminar-type gratings overcoated with carbon-based materials to enhance analytical sensitivity of flat-field emission spectrograph in the VUV region.

T. Murano, S. Koshiya, M. Koike, T. Hatano, A. Pirozhkov, T. Kakio, N. Hayashi, Y. Ohue, K. Konishi, T. Nagano, K. Kondo, M. Terauchi, *Review of Scientific Instruments*, 94(12), 125113, 2023, DOI:10.1063/5.0176783

## 4. 内視鏡下における食道病変部の面積計測法.

成田 凌, 南齊 俊佑, 星崎 みどり, 眞部 紀明, 春間 賢, 岡 潔, 長縄 明大, *産業応用工学会*, 12(1), 17 - 26, 2024, DOI:10.12792/jjiaae.12.1.17

## 5. Spectral stability of a synchronously pumped optical parametric oscillator with a spatially dispersed beam.

Keisuke Nagashima, Nobuhisa Ishii, Ryuji Itakura, *Journal of the Optical Society of America B*, 41(4), 936 - 942, 2024, DOI:10.1364/JOSAB.515148

## 6. Unsolved problem of long-range interactions: Dipolar spin-ice study.

Yonetani Yoshiteru, *Journal of Physics: Condensed Matter*, 36, 175401, 2024, DOI:10.1088/1361-648X/ad1ca6

## 7. Joint measurement of electron density, temperature, and emission spectrum of Nd:YAG laser-produced tin plasma.

Yiming Pan, Kentaro Tomita, Atsushi Sunahara, Akira Sasaki, Katsunobu Nishihara, *Applied Physics Letters* 123, 204103, 2023, DOI:10.1063/5.0174185

## 8. Spectral Shift and Split of Harmonic Lines in Propagation Affected High Harmonic Generation in a Long-Interaction Gas Tube.

Jozsef Seres, Enikoe Seres, Carles Serrat, Thanhhung Dinh, Hasegawa Noboru, Ishino Masahiko, Nishikino Masaharu, Shinichi Namba, *Atoms*, 11(12), 150-1 - 10, 2023, DOI:10.3390/atoms11120150

## 9. ミクロ-マクロシミュレーションから迫るレーザー加工.

乙部 智仁, *表面と真空*, 66(10), 587 - 592, 2023, DOI:10.1380/vss.66.587

## 10. 水の窓領域を超える軟 X 線高次高調波発生用赤外光パラメトリック増幅器を励起するための高出力イッテルビウムレーザー開発.

石井 順久, 圓山 桃子, 永島 圭介, 越智 義浩, 板倉 隆二, *レーザー研究*, 52(2), 84 - 88, 2024

## 11. Sub-nanometer scale depth patterning on Sapphire crystal by femtosecond soft x-ray laser pulse irradiation.

Mikami Kazuhiro, Ishino Masahiko, Motoyama Hiroto, Thanhhung Dinh, Yokomae Shunya, Yamaguchi Gota, Egawa Satoru, Sakaue Kazuyuki, Mimura Hidekazu, Higashiguchi Takeshi, Kubota Yuya, Owada Shigeki, Iwasaki Atsushi, Inubushi Yuichi, Nishikino Masaharu, *Optics Letters*, 48(19), 5041 - 5044, 2023, DOI:10.1364/OL.501589

**12. Induction heating for desorption of surface contamination for high-repetition laser-driven carbon-ion acceleration.**

Sadaoki Kojima, Tatsuhiko Miyatake, Hironao Sakaki, Hiroyoshi Kuroki, Yusuke Shimizu, Hisanori Harada, Norihiro Inoue, Thanhhung Dinh, Hata Masayasu, Hasegawa Noboru, Mori Michiaki, Ishino Masahiko, Nishiuchi Mamiko, Kondo Kotaro, Nishikino Masaharu, Kando Masaki, Shirai Toshiyuki, Kondo Kiminori, *Matter and Radiation at Extremes*, 8, 054002, 2023, DOI:10.1063/5.0153578

**13. Damage threshold of LiF crystal irradiated by femtosecond hard XFEL pulse sequence.**

Sergey Makarov, Sergey Grigoryev, Nail Inogamov, Evgny Filippov, Tatiana Pikuz, Norimasa Ozaki, Ishino Masahiko, Nishikino Masaharu, Thanhhung Dinh, Kawachi Tetsuya, Maxim Zhanavskiy, Mikako Makita, Motoaki Nakatsutsumi, Thomas R. Preston, Karen Appel, Zuzana Konopkova, Valerio Cerantola, Erik Brambrink, Jan-Patrik Schwinkendorf, Istvan Mohacsi, Vojtech Vozda, Vera Hajkova, Tomas Burian, Jaromir Chalupsky, Libor Juha, Vasily Zhakhovsky, Ulf Zastra, Sergey Pikuz, *Optics Express*, 31(16), 26383 - 26397, 2023, DOI:10.1364/OE.486868

**14. Observation of peripheral airways using ultra-thin fiberscope.**

Tomonari Kinoshita, Hideki Terai, Shinnosuke Ikemura, Nao Takada, Takahiro Fukui, Hidehiro Irie, Raita Miyazawa, Yohei Funatsu, Teppei Okamura, Hidefumi Koh, Tatsuya Yamamoto, Risa Shigematsu, Keiko Ohgino, Oka Kiyoshi, *Respirology*, 28, 881 - 884, 2023, DOI:10.1111/resp.14547

**15. Mixing time of homogeneous/heterogeneous solutions in a micro-mixer with free impinging jets.**

Tomoyuki Endo, Ryuji Itakura, *Bulletin of the Chemical Society of Japan*, 97(2), uoad021, 2023, DOI:10.1093/bulcsj/uoad021

**16. Optimum design of double-layer target for proton acceleration by ultrahigh intense femtosecond lasers considering relativistic rising edge.**

Hata Masayasu, Sano Takayoshi, Iwata Natsumi, Sentoku Yasuhiko, *Physical Review E*, 108(3), 035205-1 - 035205-8, 2023, DOI:10.1103/PhysRevE.108.035205

**17. Subcycle control of valley-selective excitation via dynamical Franz-Keldysh effect in WSe<sub>2</sub> monolayer.**

Shunsuke Yamada, Kazuhiro Yabana, Tomohito Otobe, *Physical Review B*, 108(3), 035404, 2023, DOI:10.1103/PhysRevB.108.035404

**18. Evaluation of a therapeutic carbon beam using a G2000 glass scintillator.**

Akihito Yokoyama, Wataru Kada, Makoto Sakai, Kenta Miura, Osamu Hanaizumi, *Applied Radiation and Isotopes*, 196, 110753, 2023, DOI:10.1016/j.apradiso.2023.110753

**19. Enhancement of valley selective excitation by a linearly polarized two-color laser pulse.**

Arqum Hashmi, Shunsuke Yamada, Kazuhiro Yabana, Tomohito Otobe, *Physical Review B*, 107(23), 235403-1 - 9, 2023, DOI:10.1103/PhysRevB.107.235403

**20. Thickness dependence of laser damage in silicon thin films.**

Prachi Venkat, Tomohito Otobe, Journal of Laser Micro/Nanoengineering, 18(3), 196 - 201, 2023, DOI:10.2961/jlmn.2023.03.2013

**21. Orientation-angle-resolved photoelectron angular distribution in dissociative ionization of methanol induced by an intense ultraviolet laser pulse.**

Shinichi Fukahori, Tomohito Otobe, Hiroshi Akagi, Kaoru Yamanouchi, Ryuji Itakura, Physical Review A, 107(5), 053118, 2023, DOI:10.1103/PhysRevA.107.053118

**22. Full characterization of few-cycle superradiant pulses generated from a free-electron laser oscillator.**

Heishun Zen, Hideaki Ohgaki, Hajima Ryoichi, Scientific Reports, 13, 6350, 2023, DOI:10.1038/s41598-023-33550-z

**23. Nonlinear Compression of Naturally Down-Chirped Superradiance Pulses from a Free-Electron Laser Oscillator by Thick Germanium Plates.**

Heishun Zen, Hajima Ryoichi, Hideaki Ohgaki, Optics Express, 31(24), 40928 - 40936, 2023, DOI:10.1364/OE.503090

**24. Laser output performance and temporal quality enhancement at the J-KAREN-P petawatt laser facility.**

Hiromitsu Kiriya, Yasuhiro Miyasaka, Akira Kon, Mamiko Nishiuchi, Akito Sagisaka, Hajime Sasao, Alexander S. Pirozhkov, Yuji Fukuda, Koichi Ogura, Kotaro Kondo, Nobuhiko Nakanii, Yuji Mashiba, Nicholas P. Dover, Liu Chang, Masaki Kando, Stefan Bock, Tim Ziegler, Thomas Püschel, Hans-Peter Schlenvoigt, Karl Zeil, Ulrich Schramm, Photonics, 10(9), 997, 2023, DOI:10.3390/photonics10090997

**25. Metrology for sub-Rayleigh-length target positioning in  $\sim 10^{22}$  W/cm<sup>2</sup> laser-plasma experiments.**

E. A. Vishnyakov, A. Sagisaka, K. Ogura, T. Zh. Esirkepov, B. Gonzalez Izquierdo, C. Armstrong, T. A. Pikuz, S. A. Pikuz, W. Yan, T. M. Jeong, S. Singh, P. Hadjisolomou, O. Finke, G. M. Grittani, M. Nevrkla, C. M. Lazzarini, A. Velyhan, T. Hayakawa, Y. Fukuda, J. K. Koga, M. Ishino, Ko. Kondo, Y. Miyasaka, A. Kon, M. Nishikino, Y. V. Nosach, D. Khikhlikha, I. P. Tsygvintsev, D. Kumar, J. Nejd, D. Margarone, P. V. Sasorov, S. Weber, M. Kando, H. Kiriya, Y. Kato, G. Korn, K. Kondo, S. V. Bulanov, T. Kawachi, A. S. Pirozhkov, High Power Laser Science and Engineering, 2024, DOI:10.1017/hpl.2024.11

**26. 固体飛跡検出器 CR-39 に形成される陽子線と重陽子線のエッチピット識別.**

望月 政一郎, 井上 千裕, 尾崎 玲於奈, 豊永 啓太, 前川 馨, 谷池 晃, 山内 知也, 福田 祐仁, 金崎 真聡, ESI-NEWS, 42, 1 - 7, 2024

**27. Automation of etch pit analyses on solid-state nuclear track detectors with machine learning for laser-driven ion acceleration.**

Tomoya Taguchi, Takumi Minami, Takamasa Hihara, Fuka Nikaido, Takafumi Asai, Kentaro Sakai, Yuki Abe, Akifumi Yogo, Yasunobu Arikawa, Hideki Kohri, Atsushi Tokiyasu, Chen Men Chu, Wei-Yen Woon, Satoshi Kodaira, Makoto Kanasaki, Yuji Fukuda, Yasuhiro Kuramitsu, Review of Scientific Instruments, 95(3), 3301-1 - 8, 2024, DOI:10.1063/5.0172202

**28. The Role of Collision Ionization of K-Shell Ions in Nonequilibrium Plasmas Produced by the Action of Super Strong, Ultrashort PW-Class Laser Pulses on Micron-Scale Argon Clusters with Intensity up to  $5 \times 10^{21}$  W/cm<sup>2</sup>.**

Igor Yu. Skobelev, Sergey N. Ryazantsev, Roman K. Kulikov, Maksim V. Sedov, Evgeny D. Filippov, Sergey A. Pikuz, Takafumi Asai, Masato Kanasaki, Tomoya Yamauchi, Satoshi Jinno, Masato Ota, Syunsuke Egashira, Kentaro Sakai, Takumi Minami, Yuki Abe, Atsushi Tokiyasu, Hideki Kohri, Yasuhiro Kuramitsu, Youichi Sakawa, Yasuhiro Miyasaka, Kotaro

Kondo, Akira Kon, Akito Sagisaka, Koichi Ogura, Alexander S. Pirozhkov, Masaki Kando, Hiromitsu Kiriya, Tatiana A. Pikuz, Yuji Fukuda, *Photonics*, 10, 1250, 2023, DOI:10.3390/photonics10111250

**29. Luminal Mirror.**

Esirkepov Timur, Sergey Bulanov, *Physical Review E*, 109(2), L023202-1 - 4, 2024, DOI:10.1103/PhysRevE.109.L023202

**30. X-ray free electron laser observation of ultrafast lattice behaviour under femtosecond laser-driven shock compression in iron.**

Sano Tomokazu, Matsuda Tomoki, Hirose Akio, Ohta Mitsuru, Terai Tomoyuki, Kakeshita Tomoyuki, Inubushi Yuichi, Sato Takahiro, Miyanishi Kohei, Yabashi Makina, Togashi Tadashi, Tono Kensuke, Sakata Osami, Tange Yoshinori, Arakawa Kazuto, Ito Yusuke, Okuchi Takuo, Sato Tomoko, Sekine Toshimori, Mashimo Tsutomu, Nakanii Nobuhiko, Seto Yusuke, Shigeta Masaya, Shobu Takahisa, Sano Yuji, Hosokai Tomonao, Matsuoka Takeshi, Yabuuchi Toshinori, Tanaka A. Kazuo, Ozaki Norimasa, Kodama Ryosuke, *Scientific Reports*, 13, 13796-1 - 10, 2023, DOI:10.1038/s41598-023-40283-6

**31. Focusing characteristic change and processing characteristic evaluation of femtosecond-to-picosecond pulse lasers above the air ionization threshold.**

Nishibata Itsuki, Nakanii Nobuhiko, Sano Tomokazu, *Optics Continuum*, 2(7), 1735 - 1751, 2023, DOI:/10.1364/OPTCON.496411

**32. Numerical studies of femtosecond electro-optical spatial decoding on the transition radiation from laser wakefield accelerated electron bunches.**

Kai Huang, Zhan Jin, Nakanii Nobuhiko, Hosokai Tomonao, Kando Masaki, *Physical Review Accelerators and Beams*, 26(11), 112801, 2023, DOI:10.1103/PhysRevAccelBeams.26.112801

**33. Design of soft X-ray laminar-type gratings coated with supermirror-type multilayer to enhance diffraction efficiency in a region of 2-4 keV.**

Masato Koike, T Hatano, Alexander Pirozhkov, Yoshihiro Ueno, Masami Terauchi, *Review of Scientific Instruments*, 94(4), 045109-1 - 045109-5, 2023, DOI:10.1063/5.0148908

**34. Half-life of the nuclear cosmochronometer  $^{176}\text{Lu}$  measured with a windowless 4n solid angle scintillation detector.**

Takehito Hayakawa, Toshiyuki Shizuma, Tsuyoshi Iizuka, *Communications Physics*, 6, 299, 2023, DOI:10.1038/s42005-023-01406-7

**35. Development of a time-gated epithermal neutron spectrometer for resonance absorption measurements driven by a high-intensity laser.**

Zechen Lan, Yasunobu Arikawa, Yuki Abe, S. Reza Mirfayzi, Alessio Morace, Takehito Hayakawa, Tianyun Wei, Akifumi Yogo, *Quantum beam science*, 8(9), qubs8010009, 2024, DOI:10.3390/qubs8010009

**36. Advances in laser-driven neutron sources and applications.**

A. Yogo, Y. Arikawa, Y. Abe, S. R. Mirfayzi, T. Hayakawa, K. Mima, R. Kodama, *The European Physical Journal A*, 59, 191, 2023, DOI:10.1140/epja/s10050-023-01083-8

**37. Application of the spectral determination method to liquid scintillation spectra.**

Masumi Oshima, Jun Goto, Takehito Hayakawa, Hirofumi Shinohara, Katsuyuki Suzuki, Yuichi Sano, Masato Asai, *Journal of Nuclear Science and Technology*, 2023, DOI:10.1080/00223131.2023.2282552

**38. Photon Vortex Generation by Synchrotron Radiation Experiments in Relativistic Quantum Approach.**

Tomoyuki Maruyama, Hayakawa Takehito, Hajima Ryoichi, Toshitaka Kajino, Myung-Ki Cheoun, *Physical Review Research*, 5, 043289, 2023, DOI:10.1103/PhysRevResearch.5.043289

**39. Feasibility study of laser-driven neutron sources for pharmaceutical applications.**

Takato Mori, Akifumi Yogo, Yasunobu Arikawa, Takehito Hayakawa, Seyed R. Mirfayzi, Zechen Lan, Tianyun Wei, Yuki Abe, Mitsuo Nakai, Kunioki Mima, Hiroaki Nishimura, Shinsuke Fujioka, Ryosuke Kodama, *High Power Laser Science and Engineering*, 11, e20, 2023, DOI:10.1017/hpl.2023.4

**40. Measurement of the spatial polarization distribution of circularly polarized gamma rays produced by inverse Compton scattering.**

Yoshitaka Taira, Shunsuke Endo, Shiori Kawamura, Taro Nambu, Mao Okuizumi, Toshiyuki Shizuma, Mohamed Omer, Heishun Zen, Yasuaki Okano, Masaaki Kitaguchi, *Physical Review A*, 107, 063503, 2023, DOI: 10.1103/PhysRevA.107.063503

**41. Generation of flat-laser Compton scattering  $\gamma$ -ray beam.**

Hideaki Ohgaki, Khaled Ali, Toshiteru Kii, Heishun Zen, Takehito Hayakawa, Toshiyuki Shizuma, Masaki Fujimoto, Yoshitaka Taira, *Physical Review Accelerators and Beams*, 26, 093402, 2023, DOI:10.1103/PhysRevAccelBeams.26.093402

**42. Parity Assignment for Low-lying Dipole States in  $^{58}\text{Ni}$ .**

T. Shizuma, M. Omer, T. Hayakawa, F. Minato, S. Matsuba, S. Miyamoto, N. Shimizu, Y. Utsuno, *Physical Review C*, 109, 014302, 2024, DOI:10.1103/PhysRevC.109.014302

**43. High-intensity single-pulse extraction using a laser-activated GaAs reflective switch for a terahertz free-electron laser.**

Kawase Keigo, Goro Isoyama, *Nuclear Instruments and Methods in Physics Research Section A: Accelerators, Spectrometers, Detectors and Associated Equipment*, 1056, 168618, 2023, DOI:10.1016/j.nima.2023.168618

**44. An X-ray and neutron scattering study of aqueous  $\text{MgCl}_2$  solution in the gigapascal pressure range.**

Yamaguchi Toshio, Fukuyama Nami, Yoshida Koji, Katayama Yoshinori, Machida Shin-ichi, Hattori Takanori, *Liquids*, 3(3), 288 - 302, 2023, DOI:10.3390/liquids3030019

**45. Temperature dependence of liquid-gallium ordering on the surface of epitaxially grown GaN.**

Takuo Sasaki, Takuya Iwata, Kanya Sugitani, Takahiro Kawamura, Tohru Akiyama, Masamitsu Takahashi, *Applied Physics Express*, 17(2), 025502, 2024, DOI:10.35848/1882-0786/ad237b

**46. Real-time observation of liquid-gallium ordering on epitaxially-grown GaN(0001) by X-ray scattering measurements.**

Takuo Sasaki, Takuya Iwata, Kanya Sugitani, Masamitsu Takahashi, *Japanese Journal of Applied Physics*, 63(2), 020901, 2024, DOI:10.35848/1347-4065/ad1f08

**47. Temperature-gradient investigation of phase transitions in ferroelectrics using cooling and heating stage.**

Shinya Tsukada, Akari Kanagawa, Kenji Ohwada, *Japanese Journal of Applied Physics*, 62(10), 106501, 2023, DOI:10.35848/1347-4065/acf908

**48. Lattice strain visualization inside a 400 nm single grain of BaTiO<sub>3</sub> in polycrystalline ceramics by Bragg coherent X-ray diffraction imaging.**

Norihiro Oshime, Kenji Ohwada, Akihiko Machida, Nagise Fukushima, Kosuke Shirakawa, Shintaro Ueno, Ichiro Fujii, Satoshi Wada, Kento Sugawara, Ayumu Shimada, Tetsuro Ueno, Tetsu Watanuki, Kenji Ishii, Hidenori Toyokawa, Koichi Momma, Sangwook Kim, Shinya Tsukada, Yoshihiro Kuroiwa, Japanese Journal of Applied Physics, 62(SM), SM1022, 2023, DOI:10.35848/1347-4065/ace832

**49. Direct momentum imaging of charge transfer following site-selective ionization.**

Felix Allum, Yoshiaki Kumagai, Kiyonobu Nagaya, James Harries, Hiroshi Iwayama, Mathew Britton, Philip H Bucksbaum, Michael Burt, Mark Brouard, Briony Downes-Ward, Taran Driver, David Heathcote, Paul Hockett, Andrew Howard, Jason W L Lee, Yusong Liu, Edwin Kukk, Joseph W McManus, Denis Milesevich, Akinobu Niozu, Johannes Niskanen, Andrew J Orr-Ewing, Shigeki Owada, Patrick A Robertson, Artem Rudenko, Kiyoshi Ueda, James Unwin, Claire Vallance, Tiffany Walmsley, Russell S Minns, Daniel Rolles, Michael R Ahsfold, Physical Review A, 108, 043113, 2023, DOI:10.1103/PhysRevA.108.043113

**50. Polarization behavior in a compositionally graded relaxor-ferroelectric crystal visualized by angle-resolved polarized Raman mapping.**

Shinya Tsukada, Yasuhiro Fujii, Akari Kanagawa, Yukikuni Akishige, Kenji Ohwada, Communications Physics, 6, 107, 2023, DOI:10.1038/s42005-023-01219-8

**51. Phase transformation and equation of state in Ti-45Al alloy under high pressure.**

Xi Li, Ruixiang Zhu, Jinghua Xin, Minsi Luo, Shun-Li Shang, Zi-Kui Liu, Chongshan Yin, Ken-Ichi Funakoshi, Rian Johannes Dippenaar, Yuji Higo, Shiro Ayumi, Mark Reid, Shobu Takahisa, Koichi Akita, Wei-Bing Zhang, Klaus-Dieter Liss, Calphad, 84, 102641, 2024, DOI:10.1016/j.calphad.2023.102641

**52. Revisiting first principles van der Waals corrections based on maximally localized Wannier functions.**

Ikeda Takashi, Chemical Physics Letters, 839, 141134, 2024, DOI:10.1016/j.cplett.2024.141134

**53. Characteristic microstructural phase evolution and the compressive strength development mechanisms of tricalcium silicate pastes under various initial carbonation curing environments.**

Seongmin Cho, Heongwon Suh, Sumin Im, Gyeongryul Kim, Manabu Kanematsu, Satoshi Morooka, Akihiko Machida, Takahisa Shobu, Sungchul Bae, Construction and Building Materials, 409(15), 133866, 2023, DOI:10.1016/j.conbuildmat.2023.133866

**54. *In situ* Ga K-edge XANES study of Ga-exchanged zeolites at high temperatures under different atmospheres including vacuum, CO, and pressurized H<sub>2</sub>.**

Mengwen Huang, Tetsuya Kinjo, Shunsaku Yasumura, Takashi Toyao, Daiju Matsumura, Hiroyuki Saitoh, Ken-ichi Shimizu, Norikazu Namiki, Zen Maeno, Catalysis Science & Technology, 13, 6832, 2023, DOI:10.1039/d3cy01250f

**55. Impact of interatomic structural characteristics of aluminosilicate hydrate on the mechanical properties of metakaolin-based geopolymer.**

Gyeongryul Kim, Seongmin Cho, Sumin Im, Heongwon Suh, Satoshi Morooka, Takahisa Shobu, Manabu Kanematsu, Akihiko Machida, Sungchul Bae, Construction and Building Materials, 411, 134529, 2023, DOI:10.1016/j.conbuildmat.2023.134529

**56. Critical role of initial multi-phase microstructure on the phase transformations during hydrogenation in Fe-Mo alloy system.**

Rama Srinivas Varanasi, Motomichi Koyama, Reina Utsumi, Hiroyuki Saitoh, Toyoto Sato, Shin-ichi Orimo, Eiji Akiyama, International Journal of Hydrogen Energy, 50, 1418 - 1434, 2023, DOI:10.1016/j.ijhydene.2023.09.268

**57. Stability and Metastability of  $\text{Li}_3\text{YCl}_6$  and  $\text{Li}_3\text{HoCl}_6$ .**

Hiroaki Ito, Yuki Nakahira, Naoki Ishimatsu, Yosuki Goto, Aichi Yamashita, Yoshikazu Mizuguchi, Chikako Moriyoshi, Takashi Toyao, Kenichi Shimizu, Hiroshi Oike, Masanori Enoki, Nataly Carolina Rosero-Navarro, Akira Miura, Kiyoharu Tadanaga, Bulletin of the Chemical Society of Japan, 96(11), 1262 - 1268, 2024, DOI:10.1246/bcsj.20230132

**58. 中 Mn 鋼と TRIP 型ベイニティックフェライト鋼の応力、塑性ひずみ分配挙動と残留オーステナイトのマルテンサイト変態挙動.**

北條 智彦, 小山 元道, 熊井 麦弥, 周 宇涛, 柴山 由樹, 城 鮎美, 菖蒲 敬久, 齋藤 寛之, 味戸 沙耶, 秋山 英二, 鉄と鋼, 110(3), 227 - 240, 2024, DOI:10.2355/tetsutohagane.TETSU-2023-062

**59. Absence of  $T_c$ -Pinning Phenomenon Under High Pressure in High-Entropy  $\text{REO}_{0.5}\text{F}_{0.5}\text{BiS}_2$  Layered Superconductor.**

Yoshikazu Mizuguchi, Kazuki Yamane, Ryo Matsumoto, Kazuhisa Hoshi, Aichi Yamashita, Akira Miura, Yuki Nakahira, Hirokazu Kadobayashi, Saori I. Kawaguchi, Yoshihiko Takano, Journal of the Physical Society of Japan, 92(11), 114702, 2023, DOI:10.7566/JPSJ.92.114702

**60. Pressure induced amorphization of  $\text{Pb}^{2+}$  and  $\text{Pb}^{4+}$  in perovskite  $\text{PbFeO}_3$ .**

Qiumin Liu, Hena Das, Takumi Nishikubo, Yuki Sakai, Ko Mibu, Tomoko Onoue, Takateru Kawakami, Tetsu Watanuki, Akihiko Machida, Xubin Ye, Jianhong Dai, Zhao Pan, Lei Hu, Satoshi Nakano, Masayuki Fukuda, Shiori Kihara, Koomok Lee, Takehiro Koike, Youwen Long, Masaki Azuma, Chemistry of Materials, 36(4), 1899 - 1907, 2024, DOI:10.1021/acs.chemmater.3c02569

**61. Abnormal Grain Growth: A Spontaneous Activation of Competing Grain Rotation.**

Klaus-Dieter Liss, Pinguang Xu, Xiaojing Liu, Ayumi Shiro, Shuoyuan Zhang, Eitaro Yukutake, Takahisa Shobu, Koichi Akita, Advanced Engineering Materials, 26, 2300470, 2024, DOI:10.1002/adem.202300470

**62. High entropy alloys containing immiscible Mg and refractory elements: synthesis, structure and hydrogen storage properties.**

Renato Belli Strozi, Kouji Sakaki, Hyunjeong Kim, Akihiko Machida, Yuki Nakahira, Jakub Cizek, Oksana Melikhova, Guilherme Zepon, Walter José Botta, Claudia Zlotea, Journal of Alloys and Compounds, 969(25), 172415, 2023, DOI:10.1016/j.jallcom.2023.172415

**63. Revealing the evolution of local structure in the formation process of alkaline earth metal cation-containing zeolite from glass.**

Peidong Hu, Makiko Deguchi, Hiroki Yamada, Kentaro Kobayashi, Koji Ohara, Sohei Sukenaga, Mariko Ando, Hiroyuki Shibata, Akihiko Machida, Yutaka Yanaba, Zhendong Liu, Tatsuya Okubo, Toru Wakihara, Physical Chemistry Chemical Physics, 26, 116 - 122, 2023, DOI:10.1039/d3cp04954j

**64. Hydrogenation behavior of a C14 Laves phase under ultra-high hydrogen pressure.**

V. Charbonnier, R. Utsumi, Y. Nakahira, H. Enoki, K. Asano, H. Kim, T. Sato, S. Orimo, H. Saitoh, K. Sakaki, Journal of Alloys and Compounds, 965, 171348, 2023, DOI:10.1016/j.jallcom.2023.171348

**65. Elucidating primary degradation mechanisms in high cycling capacity, compositionally tunable high entropy hydrides.**

Renato Strozi, Matthew Witman, Vitalie Stavila, Jakub Cizek, Kouji Sakaki, Hyunjeong Kim, Oksana Melikhova, Loïc Perrière, Akihiko Machida, Yuki Nakahira, Guilherme Zepon, Walter J. Botta, Claudia Zlotea, ACS Applied Materials & Interfaces, 6(24), 12560 - 12572, 2023, DOI:10.1021/acsaem.3c02696

**66. Selective Synthesis of Perovskite Oxyhydrides Using a High-Pressure Flux Method.**

Jinya Suzuki, Hiroyasu Okochi, Naoki Matsui, Teppei Nagase, Takumi Nishikubo, Yuki Sakai, Takuya Ohmi, Zhao Pan, Takashi Saito, Hiroyuki Saitoh, Atsunori Ikezawa, Hajime Arai, Ryoji Kanno, Takafumi Yamamoto, Masaki Azuma, Journal of the American Chemical Society, 145(30), 16398 - 16405, 2023, DOI:10.1021/jacs.3c02240

**67. Local structural changes of V-Ti-Cr alloy hydrides with on hydrogen absorption/desorption cycling.**

Kazutaka Ikeda, Sho Sashida, Toshiya Otomo, Hidetoshi Ohshita, Takashi Honda, Takafumi Hawaii, Hiraku Saito, Shinichi Itoh, Tetsuya Yokoo, Kouji Sakaki, Hyunjeong Kim, Yumiko Nakamura, Akihiko Machida, Daiju Matsumura, Wojciech Slawinski, International Journal of Hydrogen Energy, 51, 79 - 87, 2023, DOI:10.1016/j.ijhydene.2023.10.318

**68. Sound velocity and elastic properties of Fe-Ni-S-Si liquid: the effects of pressure and multiple light elements.**

Iori Yamada, Hidenori Terasaki, Sarotu Urakawa, Tadashi Kondo, Akihiko Machida, Yoshinori Tange, Yuji Higo, Physics and Chemistry of Minerals, 50, 19, 2023, DOI:10.1007/s00269-023-01243-8

**69. Integrating abnormal thermal expansion and ultralow thermal conductivity into (Cd,Ni)<sub>2</sub>Re<sub>2</sub>O<sub>7</sub> via synergy of local structure distortion and soft acoustic phonons.**

Feiyu Qin, Lei Hu, Yingcai Zhu, Yuki Sakai, Shogo Kawaguchi, Akihiko Machida, Tetsu Watanuki, Yue-Wen Fang, Jun Sun, Xiangdong Ding, Masaki Azuma, Acta Materialia, 264, 119544, 2023, DOI:10.1016/j.actamat.2023.119544

**70. Atom-Selective Analyses Reveal the Structure-Directing Effect of Cs Cation on the Synthesis of Zeolites.**

Hiroki Yamada, Hirofumi Horikawa, Chokkalingam Anand, Koji Ohara, Toshiaki Ina, Akihiko Machida, Satoshi Tominaka, Tatsuya Okubo, Zhendong Liu, Kenta Iyoki, Toru Wakihara, The Journal of Physical Chemistry Letters, 14(14), 3574 - 3580, 2023, DOI:10.1021/acs.jpcllett.3c00432

**71. 放射光 X 線と中性子を相補的に用いた小口径突合せ溶接配管の実応力解析.**

鈴木 賢治, 三浦 靖史, 城 鮎美, 豊川 秀訓, 佐治 超爾, 菖蒲 敬久, 諸岡 聡, 材料, 72(4), 316 - 323, 2023, DOI:10.2472/jsms.72.316

**72. Hydrogen occupation and hydrogen-induced volume expansion in Fe<sub>0.9</sub>Ni<sub>0.1</sub>D<sub>x</sub> at high-PT conditions.**

Shito Chikara, Kagi Hiroyuki, Kakizawa Sho, Aoki Katsutoshi, Komatsu Kazuki, Iizuka-Oku Riko, Abe Jun, Saitoh Hiroyuki, Sano-Furukawa Asami, Hattori Takanori, American Mineralogist, 108(4), 659 - 666, 2023, DOI:10.2138/am-2022-8348

**73. Synchrotron Mössbauer Micro  $\gamma$ -ray Diffractometer Installed on BL11XU at SPring-8.**

Kosuke Fujiwara, Shin Nakamura, Susumu Shimomura, Takaya Mitsui, JPS Conference Proceedings, 41, 011002, 2024, DOI:10.7566/JPSCP.41.011002

**74. Measurement of the Sub-nanometer Vibration Amplitudes Using <sup>57</sup>Fe Synchrotron Mössbauer Source.**

Hiroyuki Yamashita, Shinji Kitao, Yasuhiro Kobayashi, Hidetoshi Ota, Ryo Masuda, Kosuke Fujiwara, Takaya Mitsui, Makoto Seto, Interactions, 245, 15, 2024, DOI:10.1007/s10751-024-01854-9

**75. Anomalous Interference Effect in Pure Nuclear Bragg Reflection of  $\text{Fe}_3\text{O}_4$ .**

Shin Nakamura, Kosuke Fujiwara, Takaya Mitsui, Susumu Shimomura, Journal of the Physical Society of Japan, 92(12), 124708, 2023, DOI:10.7566/JPSJ.92.124708

**76. Feasibility Study of Thin Film Surface Analysis Using Synchrotron Low-Angle Incidence Conversion Electron Mössbauer Spectroscopy.**

Takaya Mitsui, Kosuke Fujiwara, Ko Mibu, Ryo Masuda, Yasuhiro Kobayashi, Makoto Seto, Journal of the Physical Society of Japan, 93(3), 034705, 2024, DOI:10.7566/JPSJ.93.034705

**77. Cubic-type Heusler compound  $\text{Mn}_2\text{FeGa}$  thin film with strain-induced large perpendicular magnetic anisotropy.**

Phillip David Bentley, Songtian Li, Keisuke Masuda, Yoshio Miura, Du Ye, Takaya Mitsui, Kosuke Fujiwara, Yasuhiro Kobayashi, Tengyu Guo, Guoqiang Yu, Chihiro Suzuki, Shunya Yamamoto, Fu Zheng, Yuya Sakuraba, Seiji Sakai, Physical Review Materials, 7, 064404, 2023, DOI:10.1103/PhysRevMaterials.7.064404

**78. Magnetic spin-flop transition of  $\epsilon\text{-FeOOH}$  at pressure 8 GPa.**

Osamu Ikeda, Tatsuya Sakamaki, Takaya Mitsui, Kosuke Fujiwara, Catherine A. McCammon, Akio Suzuki, Journal of the Physical Society of Japan, 92(4), 043702, 2023, DOI:10.7566/JPSJ.92.043702

**79. Quantitative measure of correlation strength among intertwined many-body interactions.**

Hideaki Iwasawa, Tetsuro Ueno, Yoshiyuki Yoshida, Hiroshi Eisaki, Yoshihiro Aiura, Kenya Shimada, Physical Review Research, 5, 043266, 2023, DOI:10.1103/PhysRevResearch.5.043266

**80. Cu  $K$ -edge X-ray Absorption Fine Structure Study of  $T'$ -type  $\text{RE}_2\text{CuO}_{4+\alpha-\delta}$  ( $\text{RE}$  = Rare earth): Toward a Unified Understanding of the Electronic State of  $T'$ -type Cuprate.**

Yizhou Chen, Shun Asano, Tong Wang, Peiao Xie, Shinnosuke Kitayama, Kenji Ishii, Daiju Matsumura, Takuya Tsuji, Takanori Taniguchi, Masaki Fujita, JPS Conference Proceedings, 38, 011050, 2023, DOI:10.7566/JPSCP.38.011050

**81. Theoretical Study of the Time-Resolved Spin Excitation Spectrum in the Photoexcited Mott Insulator.**

Kenji Tsusui, Kazuya Shinjo, Takami Tohyama, JPS Conference Proceedings, 38, 011159, 2023, DOI:10.7566/JPSCP.38.011159

**82. Photoemission Study of One-Dimensional Electronic States of (6,5), (6,6), and (7,4) Single-Walled Carbon Nanotubes.**

Ryousuke Suzuki, Ryusuke Kakihara, Hiroyoshi Ishii, Tsuneaki Miyahara, Yutaka Maniwa, Kazuhiro Yanagi, Hideaki Iwasawa, Kenya Shimada, Hirofumi Namatame, Masaki Taniguchi, Journal of The Physical Society of Japan, 92(2), 024703, 2023, DOI:10.7566/JPSJ.92.024703

**83. Laser-based angle-resolved photoemission spectroscopy with micrometer spatial resolution and detection of three-dimensional spin vector.**

Takuma Iwata, T. Kousa, Y. Nishioka, K. Ohwada, K. Sumida, E. Annese, M. Kakoki, Kenta Kuroda, H. Iwasawa, M. Arita, S. Kumar, A. Kimura, K. Miyamoto, T. Okuda, Scientific Reports, 14, 127, 2024, DOI:10.1038/s41598-023-47719-z

**84. Exploring spin-polarization in Bi-based High- $T_c$  cuprates.**

Hideaki Iwasawa, Kazuki Sumida, Shigeyuki Ishida, Patrick Le Fèvre, François Bertran, Yoshiyuki Yoshida, Hiroshi Eisaki, Andrés F. Santander-Syro, Hiroshi Eisaki, Scientific Reports, 13, 13451, 2023, DOI:10.1038/s41598-023-40145-1

**85. Three-temperature Model for Silicon Damage Process (3 温度モデルによるシリコンの損傷閾値の解析).**

Venkat Prachi, Otobe Tomohito, Journal of Japan Laser Processing Society (レーザー加工学会誌) 31(1), 26-32, 2024

**86. ローミング反応における分子構造変形の時間分解イメージング.**

遠藤 友随, 日本物理学会誌, 78(7), 410 - 414, 2023, DOI:10.11316/butsuri.78.7\_410

**87. 安定高繰り返しサブ 10 フェムト秒可視光光源の開発とその時間分解分光への応用.**

坪内 雅明, 分光研究, 72(3), 136, 2023

**88. Anomalously large heat generation of hydration water 1 under microwave.**

Hiroshi Murakami, The Journal of Physical Chemistry B, 128, 3898 - 3903, 2024, DOI:10.1021/acs.jpcc.3c07759

**89. Structural and Dynamical Changes of Nucleosome upon GATA3 binding.**

Ishida Hisashi, Atsushi Matsumoto, Hiroki Tanaka, Paul A. Wade, Aya Okuda, Ken Morishima, Hitoshi Kurumizaka, Masaaki Sugiyama, Hidetoshi Kono, Journal of Molecular Biology, 435(23), 168308, 2023, DOI:10.1016/j.jmb.2023.168308

**90. Synthetic DNA binders for fluorescent sensing of thymine glycol-containing DNA duplexes and inhibition of endonuclease activity.**

Sato Yusuke, Takaku Yoshihide, Nakano Toshiaki, Akamatsu Ken, Inamura Dai, Nishizawa Seiichi, Chemical Communications, 59, 6088 - 6091, 2023, DOI:10.1039/d3cc01501g

**91. Proximity estimation and quantification of ionizing radiation-induced DNA lesions in aqueous media using fluorescence spectroscopy.**

Akamatsu Ken, Sato Katsuya, Shikazono Naoya, Takeshi Saito, Radiation Research, 201(2), 150 - 159, 2023, DOI:10.1667/RADE-23-00145.1

## Proceedings

**1. X 線吸収微細構造法によるヒト血清中ウランの化学形解析.**

上原 章寛, 松村 大樹, 城 鮎美, 田中 泉, 辻 卓也, 齋藤 寛之, 石原 弘, 武田 志乃, Fundamental Toxicological Sciences, 10, 127, 2023

**2. 第一原理計算による半導体ナノ構造の非線形光学効果のシミュレーション.**

木原 康輝, 松浦 豪介, 山田 俊介, 植本 光治, 第 34 回光物性研究会論文集, 235 - 238, 2023

**3. Generation of Naturally Down-Chirped Few-Cycle Pulse from Free-Electron Laser Oscillator and Its Pulse Compression.**

Heishun Zen, Hideaki Ohgaki, Ryoichi Hajima, 2023 48th International Conference on Infrared, Millimeter, and Terahertz Waves (IRMMW-THz), 2024, DOI:10.1109/IRMMW-THz57677.2023.10299308

#### 4. Laser-induced gas breakdown by a train of femtosecond long-wave infrared FEL pulses.

R. Hajima, Keigo Kawase, James K. Koga, H. Zen, H. Ohgaki, 2023 48th International Conference on Infrared, Millimeter, and Terahertz Waves (IRMMW-THz), 2024, DOI:10.1109/IRMMW-THz57677.2023.10299282

#### 5. 光伝搬に外部境界条件を組み込んだ自由電子レーザーのシミュレーション.

坂本 文人, 加藤 龍好, 本田 洋介, 島田 美帆, 阪井 寛志, 中村 典雄, 谷川 貴紀, 羽島 良一, 第 20 回日本加速器学会年会プロシーディングス, 361 - 364, 2024

#### 6. 自由電子レーザーで駆動する高繰り返しアト秒光源の研究: 2023.

羽島 良一, 川瀬 啓悟, 全 炳俊, 大垣 英明, 早川 恭史, 境 武志, 第 20 回日本加速器学会年会プロシーディングス, 899 - 901, 2024

#### 7. Carrier-envelope phase stabilization in FEL oscillators.

Hajima Ryoichi, Kawase Keigo, Heishun Zen, Hideaki Ohgaki, Journal of Physics: Conference Series, 2687, 032013, 2024, DOI:10.1088/1742-6596/2687/3/032013

#### 8. Laser-induced gas breakdown at KU-FEL.

Hajima Ryoichi, Heishun Zen, Hideaki Ohgaki, Proceedings of FEL 2022, 2023, DOI:10.18429/JACoW-FEL2022-MOP28

#### 9. Unaveraged simulation of superradiance in FEL oscillators.

Hajima Ryoichi, Proceedings of FEL 2022, 2023, DOI:10.18429/JACoW-FEL2022-MOP27

#### 10. スポーク空洞における HOM 減衰の研究.

沢村 勝, Proceedings of the 20th Annual Meeting of Particle Accelerator Society of Japan, 646 - 648, 2023

#### 11. 中赤外自由電子レーザーによる気体のトンネルイオン化電子のエネルギー計測.

川瀬 啓悟, 羽島 良一, 大垣 英明, 全 炳俊, 第 20 回日本加速器学会年会プロシーディングス, 741 - 743, 2023

#### 12. 放射線照射によって生じた DNA 損傷の構造解析と修復速度.

中野 敏彰, 赤松 憲, 鹿園 直哉, 放射線化学, 116, 15 - 19, 2023

#### 13. Multi-scale simulations aiming to advance heavy ion beam cancer therapy.

Moribayashi Kengo, Matsubara Hiroshi, Yonetani Yoshiteru, Shikazono Naoya, AIP conference proceedings, 2756, 030001-1 - 8, 2023, DOI: 10.1063/5.0140807

## 表彰

#### 1. 第 47 回レーザー学会 業績賞 (論文賞) .

榊 泰直「レーザー加速炭素ビーム粒子数のシングルショット診断」  
レーザー学会, 2023-05-31

#### 2. HPCI ソフトウェア賞開発部門賞奨励賞.

山田 俊介, 廣川 祐太, 飯田 健二, 岩田 潤一, 野田 真史, 乙部 智仁, 佐藤 駿丞, 篠原 康, 竹内 嵩, 谷 水城, 植本 光治, 矢花 一浩, 山田 篤志

「SALMON (Scalable Ab-initio Light-Matter simulator for Optics and Nanoscience)」  
一般社団法人 HPCI コンソーシアム, 2023-05-19

**3. 優秀若手表彰（オーラルの部）受賞.**

内海 伶那「Mn に富む Al-Mn 合金水素化物の水素吸蔵放出能の評価」  
公益社団法人日本金属学会 水素が関わる材料科学の課題共有研究会, 2023-12-08

**4. 令和 5 年度 科学技術分野の文部科学大臣表彰.**

三井 隆也、境 誠司「一原子層毎の磁性探査法を用いた鉄表面の特異な磁性の研究」  
文部科学省, 2023-04-07

**5. 大阪ニュークリアサイエンス協会賞受賞（ONSA 賞）.**

中野 敏彰「Formation of clustered DNA damage in vivo upon irradiation with ionizing radiation: visualization and analysis with atomic force microscopy」  
一般社団法人 大阪ニュークリアサイエンス協会 (ONSA) , 2023-06-05

## 特許登録

**1. Laser device, light source, and measurement device.**

Akahane Yutaka, Aoyama Makoto, Ogawa Kanade, Yamakawa Koichi  
欧州 EP3680998 (2023-06-14)

**2. 組織識別装置、組織識別システム、組織識別方法、検査方法、内視鏡システム、組織識別プログラムおよび記録媒体.**

Yamakawa Koichi, Aoyama Makoto, Morioka Takamitsu, Imaoka Tatsuhiko  
台湾 I819004 (2023-10-21)

**3. 計測装置、計測システム、移動体、および計測方法.**

Nishikino Masaharu, Hasegawa Noboru, Mikami Katsuhiro, Kitamura Toshiyuki, Kondo Shuji, Okada Hajime, Kawachi Tetsuya  
米国 US2023/0258609 A1 (2023-08-17)

**4. 計測装置、計測システム、移動体、および計測方法.**

Nishikino Masaharu, Hasegawa Noboru, Mikami Katsuhiro, Kitamura Toshiyuki, Kondo Shuji, Okada Hajime, Kawachi Tetsuya  
中国 6466407 (2023-11-07)

**5. インプラント設置強度評価方法、インプラント設置強度評価装置、およびプログラム.**

Nishikino Masaharu, Hasegawa Noboru, Mikami Katsuhiro, Kitamura Toshiyuki, Kondo Shuji, Okada Hajime  
米国 11737705 (2023-08-29)

**6. 計測装置、計測システム、移動体、および計測方法.**

Nishikino Masaharu, Hasegawa Noboru, Mikami Katsuhiro, Kitamura Toshiyuki, Kondo Shuji, Okada Hajime, Kawachi Tetsuya  
インド 451962 (2023-09-15)

**7. レーザー増幅装置.**

錦野 将元, 長谷川 登, 三上 勝大, 近藤 修司, 岡田 大, 河内 哲哉  
日本 7286898 (2023-05-29)

# 特許出願

## 1. イオン発生装置、イオン発生方法、およびイオン発生用ターゲット。

小島 完興, 榊 泰直, 宮武 立彦, 近藤 公伯, 黒木 宏芳, 清水 祐輔, 原田 寿典, 井上 典洋  
PCT/JP2023/ 41213 (2023-11-16)

## 2. 損傷評価装置及び損傷評価用プログラム。

長谷川 登, 錦野 将元, 岡田 大, 近藤 修司  
特願 2023-122463 (2023-07-27)

## 3. イオン加速方法およびイオン加速装置。

福田 祐仁, 金崎 真聡, 井上 千裕  
特願 2023-141144 (2023-08-31)

## 4. 顕微計測方法及び顕微計測装置。

藤原 孝将, 三井 隆也, 長谷川 登  
特願 2023-147113 (2023-09-11)

# The Kids' Science Museum of Photons

## 概要

4月は事前予約制と滞在時間制限を廃止しつつ、閉館後の展示装置消毒作業のための閉館時間の30分繰り上げ、プラネタリウム鑑賞の入場制限(60名/116席)ならびに一部展示装置の利用制限を維持しての開館となりました。

5月のゴールデンウィークには特別イベントとして工作体験コーナーを実施。開館時間以前に来館者が長蛇の列を成す光景が3年3か月ぶりに復活しました。

6月21日(水)からはプラネタリウム映像ホールへの入場制限を廃止し、大人数の団体受入が可能となりました。また、大阪科学技術館での展示期間が終了したHIMAC施設の模型などを科学館に移設しました。

7月は11日には開館22周年を迎え、また29日から8月20日にかけて夏休み特別イベントとして工作体験コーナーを実施しました。

11月は木津川市の木津南地区で開催されたイベント「木津川アート2023」に協力。館内において3件の特別展示を受入れ、さらにイベント出展の全天映像5作品の上映を行いました。また、11日(土)に関西研の一般公開が行われた際には、その特別イベントコーナーとしてレーザーラボを実演しました。

12月2日より、土日・祝日の親子工作コーナーを再開しました。また27日から翌年1月7日にかけては冬休みイベントとして、さらには3月27日から新年度4月7日にかけては春休みイベントとして、親子工作コーナーを実施しました。

## 2023年度の活動

### 1. 主な行事

2023年5月3日～7日	こどもワークショップ
7月29日～8月20日	こどもワークショップ 夏休み工作
11月3日～19日	木津川アート2023
11月11日	関西光量子科学研究所 施設公開
12月2日～28日	Photons Merry Christmas 2023
2024年1月4日～28日	A Happy New Year 2024
2月3日～25日	Photons Happy Valentine
3月27日～4月7日	こどもワークショップ 春休み工作

### 2. 来館者状況

平日は主に、学校、自治体、各種支援団体などによる団体見学や、幼児連れの方の利用が中心で、土・日・祝日や長期の休みなどにはご家族によるご利用が中心となります。2023年度の総入館者数は28,206人となりました。例年、月間入館者数が最も多いのは8月ですが、2023年は8月期の4,558人のほか、11月にもほぼ同数の4,516人をお迎えしました。これは木津川市のイベント「木津川アート2023」への協力が表れたものと思われます。特に11月11日には関西研の施設公開とも重なったことから、1日で1,165名と歴代第2位の来館者数を記録しました(それまでの記録は2019年4月30日の1,001名。なお歴代第1位は同じく関西研施設公開日であった2016年10月23日の1,333名)。

来館実績

年 月	開館日数	月別	累計
2023年4月	22日	1,917人	1,917人
5月	21日	2,339人	4,256人
6月	21日	1,635人	5,891人
7月	22日	2,556人	8,447人
8月	22日	4,558人	13,005人
9月	21日	1,786人	14,791人
10月	20日	1,373人	16,164人
11月	22日	4,516人	20,680人
12月	20日	1,283人	21,963人
2024年1月	20日	1,724人	23,687人
2月	22日	2,020人	25,707人
3月	23日	2,499人	28,206人
年度合計	256日	28,206人	-

3. 事業内容（工作・映像・実験）

(1) 工作教室

マルチホールにおいて、親子工作教室を午前（10:15～10:45）、午後（15:00～15:30）の2回、それぞれ定員10名にて行いました。工作内容は主に小学生を対象としていますが、一部は幼児から参加できるものも用意いたしました。

工作教室実績

年 月	実施日数	実施回数	参加者数
2023年4月	-	-	-
5月	5日	10回	98人
6月	-	-	-
7月	2日	4回	39人
8月	15日	30回	289人
9月	-	-	-
10月	-	-	-
11月	-	-	-
12月	10日	18回	113人
2024年1月	10日	20回	155人
2月	9日	18回	144人
3月	14日	28回	227人
年度合計	65日	128回	1,065人

## (2) 映像コンテンツの上映

光の映像ホール（ドーム型全天周映像ホール）における上映は、開館時間の 30 分短縮に伴い、午前（11:10～11:30）、午後（14:00～14:30）の 2 回とし、午後 2 回目（15:40～16:10）の上映は現在休止しています。なお団体見学者の要望があった場合は適宜、臨時上映を行いました。

6 月 21 日（水）からは入場制限を解除し、全ての座席（116 席）を開放しての上映を開始いたしました。

11 月の木津川アート期間中には、1 日 3 回目の特別枠（15:15～15:45）を設け、同イベントに参加したアーティストの映像作品 5 作品（合計約 23 分）の上映を行いました。2023 年度の観覧者数は 16,947 人です。

### 入場制限の様子



### 上映実績

年 月	上映日数	上映回数	観覧者数	累積観覧者数
2023 年 4 月	22 日	39 回	1,065 人	1,065 人
5 月	20 日	43 回	1,525 人	2,590 人
6 月	21 日	36 回	981 人	3,571 人
7 月	22 日	43 回	1,613 人	5,184 人
8 月	22 日	46 回	3,196 人	8,380 人
9 月	20 日	39 回	1,180 人	9,560 人
10 月	20 日	38 回	924 人	10,484 人
11 月	22 日	52 回	1,400 人	11,884 人
12 月	20 日	36 回	840 人	12,724 人
2024 年 1 月	19 日	37 回	1,139 人	13,863 人
2 月	22 日	45 回	1,393 人	15,256 人
3 月	23 日	45 回	1,691 人	16,947 人
年度合計	253 日	499 回	16,947 人	-

### (3) レーザーラボ

Nd:YAG レーザーや He-Ne レーザー、分光器等を用いた光及びレーザーに関するライブ実験を実演するコーナーです。2023 年度は定例実演を休止しておりましたが、11 月の関西研施設公開の特別コーナーとして 2 ステージ、また 2024 年 2 月に学校関連団体の方からのご要望に応じて 3 ステージの計 5 回を実施しました。2023 年度の観覧者数は 220 人です。





# Appendix

## 共同研究課題、施設共用課題

### 1) 木津地区

#### 【共同研究課題】

共同研究先	共同研究課題名	担当研究グループ
株式会社 EX-Fusion、神戸大学	クライオターゲットに関する研究	先端レーザー科学研究グループ
東北大学、株式会社島津製作所	電子顕微鏡用次世代型軟X線回折格子分光器の開発	先端レーザー科学研究グループ
同志社大学	フェムト秒パルスレーザーの位相受動整合コヒーレント加算に関する研究	先端レーザー科学研究グループ
大阪大学、東北大学	シンチレータを用いた相対論的イオン検出手法の開発	先端レーザー科学研究グループ
神戸大学、名古屋大学	固体飛跡検出器を用いた高エネルギーイオン検出手法の高精度化	先端レーザー科学研究グループ
大阪大学、青山学院大学、九州大学	宇宙物理の手法に基づく粒子加速・電磁放射に関する研究	先端レーザー科学研究グループ
近畿大学	振動計測による光学素子の損傷検出と損傷予知に関する研究	先端レーザー科学研究グループ
東海大学、大阪産業大学	レーザー微細加工によるチタンサファイアの寄生発振抑制に関する研究	先端レーザー科学研究グループ
大阪大学	レーザー電子加速の安定化・性能評価研究	高強度場科学研究グループ
株式会社日本防振工業	レーザー電子加速に資する防振・光軸安定化に関する研究	高強度場科学研究グループ
金属技研株式会社	レーザー加速による小型X線光源加速器の設計研究	高強度場科学研究グループ
高エネルギー加速器研究機構	超伝導加速器のための高調波モード減衰器の高性能化の研究開発	LCSガンマ線研究グループ
日本原子力研究開発機構、分子科学研究所	透過型核共鳴蛍光散乱を用いた核検知測定技術の研究開発	LCSガンマ線研究グループ
日本原子力研究開発機構、兵庫県立大学	レーザー・コンプトン散乱ガンマ線を用いた元素分析技術の研究開発	LCSガンマ線研究グループ
日本電子株式会社	電子顕微鏡用次世代型軟X線回折格子分光器の開発	量子応用光学研究部
ライトタッチテクノロジー株式会社	中赤外レーザーを用いた医療応用計測技術の開発	量子応用光学研究部
奈良先端科学技術大学院大学	遷移金属ダイカルコゲナイド薄膜を利用した光誘起相転移デバイスの開発	超高速電子ダイナミクス研究プロジェクト

東京大学	高強度極短パルスレーザーによる分子のイオン化過程の解明	超高速電子ダイナミクス研究プロジェクト
東京大学	レーザー加工のための学理シミュレーターの研究開発	超高速電子ダイナミクス研究プロジェクト
兵庫県立大学	機能性磁性薄膜材料の高速光磁気効果に関する研究	超高速電子ダイナミクス研究プロジェクト
京都大学、東海大学	TW 級チタンサファイアレーザーを用いた量子ビーム発生と応用に関する研究	レーザー駆動イオン加速器開発プロジェクト
兵庫県粒子線医療センター	量子メスに向けた粒子線照射計測及び制御技術に関する研究	レーザー駆動イオン加速器開発プロジェクト
住友重機械工業株式会社	量子メス用レーザー加速入射器の炭素ビーム評価手法の開発	レーザー駆動イオン加速器開発プロジェクト
日立造船株式会社	量子メス用レーザー加速入射器のターゲット駆動装置に関する開発	レーザー駆動イオン加速器開発プロジェクト
奈良女子大学	量子メス用レーザー加速入射器からのイオンビーム利用に関する研究	レーザー駆動イオン加速器開発プロジェクト
株式会社フォトラボ	レーザー誘起振動波計測技術の小型化・長距離化に関する研究	X 線超微細加工技術研究プロジェクト
宇都宮大学、広島大学、東北大学	高輝度軟 X 線発生に関する基礎研究	X 線超微細加工技術研究プロジェクト
核融合科学研究所、京都工芸繊維大学、富山高等専門学校	凝縮相の量子・分子動力学計算に関する研究	X 線超微細加工技術研究プロジェクト
近畿大学	軟 X 線レーザー照射による酸化物表面の微細加工に関する研究	X 線超微細加工技術研究プロジェクト
株式会社建設技術研究所、東海国立大学機構、計測検査株式会社	道路トンネル用レーザー打音ロボット検査装置の製作	X 線超微細加工技術研究プロジェクト

#### 【施設共用課題】

課題番号	利用区分	施設装置	利用課題
2023A-K01	公開	QUADRA-T レーザーシステム	数サイクル高強度中赤外光により誘起される分子の電子状態間結合の解明
2023A-K02	公開	J-KAREN-P レーザー装置	磁気ボトル型電子分光器による BISER X 線の特性評価
2023A-K03	公開	J-KAREN-P レーザー装置	高強度レーザー駆動非平衡輻射高 Z プラズマの形成過程と輻射特性の解明(続)
2023A-K10	公開	kHz チタンサファイアレーザー	二次元層状半導体を用いた超高速非線形光デバイスの開発

## 2) 播磨地区

### 【共同研究課題】

共同研究先	共同研究課題名	担当研究グループ
日本原子力研究開発機構	放射光による物質科学に関する研究	放射光科学研究センター
京都大学	同位体特定による局所状態解明のための先進的メスbauer分光法の開発研究	磁性科学研究グループ
JEF テクノリサーチ株式会社	磁気円偏光発光を用いた方向性珪素鋼板の内部磁区観察のための研究開発	磁性科学研究グループ
SLAC National Accelerator Laboratory	高温超伝導における複種多体相互作用の協奏(受託研究: 二国間交流事業共同研究/セミナー)	先進分光研究グループ
上智大学	X線吸収分光・発光分光による銅酸化物超伝導体の研究	先進分光研究グループ
東北大学	RIXSの超高エネルギー分解能活用に向けた遷移金属酸化物における電子相の研究	先進分光研究グループ
東北大学	二次元物質・規則合金ヘテロ構造界面磁性の解明による革新的強磁性トンネル接合素子の創成に関する研究	先進分光研究グループ
広島大学	コヒーレント X 線を利用した強誘電体一粒子計測	コヒーレント X 線利用研究グループ
TDK 株式会社、広島大学	放射光 X 線回折を用いた構造解析技術の開発	コヒーレント X 線利用研究グループ
産業技術総合研究所	水素雰囲気その場・時分割放射光 X 線全散乱を利用した水素吸蔵合金の構造変化の観測	水素材料科学研究グループ
物質・材料研究機構	放射光 X 線全散乱を利用した先端機能性材料のナノ構造評価手法の開発	水素材料科学研究グループ
京都大学	放射光単色 X 線を利用した新規がん治療技術の開発	水素材料科学研究グループ
東北大学	新規アルミニウム合金水素化物の探索に関する研究	水素材料科学研究グループ

### 【施設共用課題】

播磨地区では、2021年度より文部科学省マテリアル先端リサーチインフラ事業を受託しています。当該事業では2021年度まで行われたナノテクノロジープラットフォーム事業に引き続き2022年度から放射光科学研究施設を成果非専有課題で利用する外部研究者に対して、特に専用ビームラインにおける研究支援を強化しています。また、従来の設備の共用に加えて、データの共用も重要になります。課題は年2回、SPring-8を運営する公益財団法人高輝度光科学研究センターの一般課題募集時期(5月及び11月)に合わせて募集しています。

課題番号	利用区分	施設装置	利用課題
2023A-H01	公開	放射光メスbauer分光装置	核共鳴散乱を用いた混合原子価鉄酸化物の電荷秩序配列の検証(2)
2023A-H02	公開	放射光メスbauer分光装置	ガンマ線光子相関時間測定系の開発研究II
2023A-H03	公開	放射光メスbauer分光装置	超高压下における地球下部マントル物質中の鉄の電子状態とその分配係数への寄与
2023A-H04	公開	共鳴非弾性X線散乱装置	イルメナイト型構造Ir酸化物における結晶場励起の系統的観測
2023A-H05	公開	共鳴非弾性X線散乱装置	Key Technique Research and Performance Characterization of the Diced Crystal Analyzer for High Energy Resolution Inelastic X-ray Scattering Spectroscopies
2023A-H06	公開	共鳴非弾性X線散乱装置	高分解能 XAFS を利用した燃料電池カソード鉄錯体系電極触媒上における酸素還元反応時の吸着構造解明研究
2023A-H07	公開	表面X線回折計	その場X線回折測定を用いた逆臨界膜厚エピタキシー過程の観察
2023A-H08	公開	表面X線回折計	スパッタアニールAlNの表面クリーニングによる極性制御メカニズムの解明
2023A-H09	公開	表面X線回折計	GaNリモートエピタキシーのサファイア基板面方位依存性のリアルタイムX線回折による解析
2023A-H10	公開	表面X線回折計	赤色発光InGaN量子構造形成におけるその場X線回折測定
2023A-H11	公開	高温高压プレス装置	量子ビームハイブリット実応力解析の小口径溶接配管の残留応力マップへの応用
2023A-H12	公開	高温高压プレス装置	高压下のイオン拡散を利用した酸素化物BaTiO <sub>3-x</sub> H <sub>x</sub> のその場観察
2023A-H13	公開	高温高压プレス装置	水素誘起アモルファス化後の水素吸蔵反応の観測
2023A-H14	公開	高温高压プレス装置	圧力効果を利用したP2型Na <sub>2/3</sub> Mn <sub>2/3</sub> Ni <sub>1/3</sub> O <sub>2</sub> の低温合成
2023A-H15	公開	高温高压プレス装置	高压合成技術を活用した100MPa級超高压作動型水素吸蔵合金の探索
2023A-H16	公開	高温高压プレス装置	Hf系高水素配位錯イオンを含む錯体水素化物の探索
2023A-H19	公開	高速2体分布関数計測装置	Ti <sub>50+y</sub> (Fe <sub>1-x</sub> Mn <sub>x</sub> ) <sub>50-y</sub> の水素吸蔵・放出反応の相変化挙動のTiおよびMn組成依存性
2023A-H20	公開	高速2体分布関数計測装置	Phase evolution, mechanical properties, and morphology of cementitious silicate hydrates subjected to carbonation

2023A-H21	公開	コヒーレントX線回折イメージング装置	電場印加下における電子デバイス内部のナノ粒子非破壊3次元的位置特定技術および構造可視化手法の開発
2023A-H22	公開	コヒーレントX線回折イメージング装置	Bragg-CDIによる正方晶巨大負熱膨張物質のドメイン構造温度変化の観察II
2023A-H23	公開	コヒーレントX線回折イメージング装置	ナノヘテロ構造体電子セラミクス材料における構造傾斜領域の観察
2023A-H24	公開	コヒーレントX線回折イメージング装置	遷移金属酸水素化物の結晶歪観察
2023A-H25	公開	コヒーレントX線回折イメージング装置	半導体用シリコン単結晶の内部に孤立形成された微結晶の解析
2023A-H26	非公開	コヒーレントX線回折イメージング装置	車載用円筒缶二次電池のかしめ部の応力測定
2023A-H27	非公開	高温高压プレス装置	Fe系磁性体の圧力印加試験
2023B-H01	公開	放射光メスバウアー分光装置	メスバウアー分光法を用いたGdFe合金のミクロな原子構造の解析と磁気異方性発現機構の調査
2023B-H02	公開	放射光メスバウアー分光装置	超高压下における地球下部マントル物質中の鉄の電子状態とその分配係数への寄与
2023B-H03	公開	放射光メスバウアー分光装置	核共鳴散乱を用いた混合原子価鉄酸化物の電荷秩序配列の検証(3)
2023B-H04	公開	放射光メスバウアー分光装置	ガンマ線光子相関時間測定系の開発研究III
2023B-H05	公開	放射光メスバウアー分光装置	高水素圧力下におけるEu水素化物の電子状態分析III
2023B-H06	公開	共鳴非弾性X線散乱装置	Exploring orbital excitations in bulk pyrochlore rhenates
2023B-H07	公開	共鳴非弾性X線散乱装置	燃料電池触媒を志向したFe, Cu化合物のHERFD-XAS, XESフィジビリティスタディ
2023B-H08	公開	共鳴非弾性X線散乱装置	高分解能XAFSを利用した燃料電池カソード鉄錯体系電極触媒上における酸素還元反応時の吸着構造解明研究
2023B-H09	公開	共鳴非弾性X線散乱装置	深さ分解手法を用いた方向性電磁鋼板の内部磁区構造調査
2023B-H10	公開	表面X線回折計	その場X線回折測定を用いたGaNリモートエピタキシー過程の観察
2023B-H11	公開	表面X線回折計	その場X線CTR散乱を利用した-c極性AlN極性反転メカニズムの解明
2023B-H12	公開	表面X線回折計	ScAlMgO <sub>4</sub> 基板上InGaN成長におけるその場X線回折測定

2023B-H13	公開	高温高圧プレス装置	高温高圧下におけるバナジウム酸水素化物のアニオン秩序-無秩序相転移のメカニズム解明
2023B-H14	公開	高温高圧プレス装置	高温水素環境での鉄鋼材料の損傷組織のその場観測技術の開発
2023B-H15	公開	高温高圧プレス装置	高圧下での $Y_3Al_2$ の水素吸蔵反応の観測
2023B-H16	公開	高温高圧プレス装置	高圧合成技術を活用した $TiFeH_4$ 相の合成
2023B-H17	公開	高温高圧プレス装置	高温高圧合成によるTi、ならびにTi基合金でのfcc構造の形成
2023B-H18	公開	高温高圧プレス装置	放射光X線その場観察による物性評価用高純度試料の合成
2023B-H19	公開	高速2体分布関数計測装置	非混合性のハイエントロピー合金と複合化したMgの水素吸蔵放出反応に伴う構造変化の解明
2023B-H20	公開	高速2体分布関数計測装置	放射光全散乱測定による低結晶性 $P2-Na_{2/3}Mn_{2/3}Ni_{1/3}O_2$ のin situ, ex situ PDF解析を用いた劣化機構解析
2023B-H21	公開	コヒーレントX線回折イメージング装置	ナノヘテロ構造体電子セラミクス材料における構造傾斜領域の精察
2023B-H22	公開	コヒーレントX線回折イメージング装置	ナノ粒子非破壊3次元構造可視化による故障解析技術の開発: 電場印加による電子デバイス内部の誘電体材料の疲労の起源解明
2023B-H23	公開	コヒーレントX線回折イメージング装置	Bragg-CDIによる正方晶巨大負熱膨張物質のドメイン構造温度変化の観察III
2023B-H24	非公開	コヒーレントX線回折イメージング装置	電池材料粉末のBragg-CDI測定
2023B-H25	非公開	コヒーレントX線回折イメージング装置	車載用円筒缶二次電池のかしめ部の応力測定

関西光量子科学研究所での各種シンポジウム・施設公開・出展・アウトリーチ活動

【木津地区】

1	13-14-JUN-2023	大阪大学レーザー科学研究 所（オンライン・現地ハイブ リッド開催）	主催：関西光量子科学研究所、大阪大学 レーザ ー科学研究所
	光・量子ビーム科学合同シンポジウム 2023 The Joint Symposium on Optical and Quantum Beam Science (OPTO2023)		
2	20-JUN-2023	オンライン開催	主催：科学技術振興機構
	新技術説明会		
3	10-13-JUL-2023	淡路夢舞台国際会議場	主催：関西光量子科学研究所
	第 79 回藤原セミナー：高強度場科学の展望 Prospects for High Field Science, PHFS2023		
4	29-30-JUL-2023	科学技術館	主催：日本科学技術振興財団
	青少年のための科学の祭典 2023 全国大会 偏光スタンドグラス工作		
5	5-6-OCT-2023	オンライン開催	主催：関西文化学術研究都市推進機構
	けいはんなビジネスメッセ 2023		
6	6-7-OCT-2023	けいはんなオープンイノベ ーションセンター	主催：けいはんな R&D フェア実行委員会
	けいはんな R&D フェア 2023 ワークショップの出展：偏光スタンドグラス		
7	5-NOV-2023	京田辺市田辺中央体育館	主催：京田辺市
	京田辺市民文化フェスティバル 偏光スタンドグラス工作		
8	11-NOV-2023	関西光量子科学研究所	主催：関西光量子科学研究所
	関西光量子科学研究所（木津地区）施設公開		
9	10-DEC-2023	大阪科学技術館	主催：大阪科学技術館
	クリスマススペシャルイベント 2023 実験ショーと偏光スタンドグラス工作		
10	23-24-JAN-2024	理化学研究所 和光事業所	主催：理化学研究所 光量子工学研究センター、 関西光量子科学研究所
	The 7th RIKEN-RAP and QST-KPSI Joint Seminar		
11	20-MAR-2024	国際高等研究所	主催：国際高等研究所
	学生の学生による学生のための教養講座 けいはんな科学コレクション		

【播磨地区】

1	9-12-JUL-2023	SPring-8	主催：兵庫県立大学理学部・大学院理学研究科、 関西学院大学理学部・工学部・生命環境学部・ 大学院理工学研究科、岡山大学、大阪大学光科学 連携センター・蛋白質研究所・核物理研究セン ター、茨城大学大学院理工学研究科、理化学 研究所 放射光科学研究センター、(公財) 高輝 度光科学研究センター (JASRI)、日本原子力 研究開発機構 物質科学研究センター、量子科 学技術研究開発機構 関西光量子科学研究所
	第 23 回 SPring-8 夏の学校		
2	22-23-AUG-2023 14-16-NOV-2023 15-17-NOV-2023	SPring-8 自然科学研究機構分子科学 研究所 香川大学	主催：物質・材料研究機構マテリアル先端リサ ーチインフラセンターハブ運営室
	文部科学省マテリアル先端リサーチインフラ 技術スタッフ交流プログラム		
3	10-13-SEP-2023	SPring-8	主催：SPring-8 ユーザー協団体、(公財) 高輝 度光科学研究センター
	第 7 回 SPring-8 秋の学校		
4	11-12-SEP-2023	大阪大学吹田キャンパス	主催：日本放射光学会、科研費・学術変革領域 研究(A)「データ記述科学」材料科学班
	第 15 回 日本放射光学会 若手研究会 ―放射光と顕微鏡技術・機械学習との交差点―		
5	26-27-SEP-2023	大阪大学会館（オンライン・ 現地ハイブリッド開催）	主催：SPring-8 ユーザー協団体、理化学研究所 放射光科学研究センター、(公財) 高輝度光科 学研究センター、大阪大学
	SPring-8 シンポジウム 2023 ―SPring-8/SACLA とデータ科学の融合が生み出す可能性―		
6	29-SEP-2023	萌光館（オンライン・現地ハ イブリッド開催）	主催：原子力機構物質科学研究センター、関西 光量子科学研究所 放射光科学研究センター
	令和 5 年度文部科学省マテリアル先端リサーチインフラ事業 JAEA & QST 合同放射光利用講習会 ―放射光分光・イメージングによる電子状態・構造分析―		
7	17-OCT-2023	播磨高原東中学校	主催：関西光量子科学研究所
	令和 5 年度播磨高原東中学校出前授業（3 年生対象）		
8	21-NOV-2023	九州大学 伊都キャンパス	主催：物質・材料研究機構マテリアル先端リサ ーチインフラセンターハブ運営室
	文部科学省マテリアル先端リサーチインフラ 技術スタッフ集合研修会		
9	19-DEC-2023	東京大学	主催：物質・材料研究機構マテリアル先端リサ ーチインフラセンターハブ運営室
	文部科学省マテリアル先端リサーチインフラ 第 1 回計測技術スタッフ全体研修会		
10	21-DEC-2023	SPring-8	主催：物質・材料研究機構マテリアル先端リサ ーチインフラセンターハブ運営室
	文部科学省マテリアル先端リサーチインフラ サイトビジット		

11	10-12-JAN-2024	アクリエひめじ	主催：第 37 回日本放射光学会年会・放射光科学合同シンポジウム組織委員会
	第 37 回日本放射光学会年会・放射光科学合同シンポジウム		
12	31-JAN-2-FEB-2024	東京ビッグサイト	主催：nano tech 2024 実行委員会
	第 23 回国際ナノテクノロジー総合展・技術会議 (nano tech 2024) マテリアル先端リサーチインフラ事業ブースに説明員派遣		
13	11-MAR-2024	オンライン開催	主催：物質・材料研究機構
	文部科学省マテリアル先端リサーチインフラ 第 1 回マテリアル循環-量子・電子制御領域合同セミナー		
14	14-MAR-2024	アクリエひめじ	主催：兵庫県立大学高度産業科学技術研究所
	ニューズバルシンポジウム 2024		

### KPSI セミナー (第 97 回～104 回)

木津地区では国内外の著名な研究者をお招きして学術的に最先端の専門的なセミナーを開催しています。今年度は合計 8 回開催しました。開催にあたっては KPSI Web サイトを活用し、関西研内外に開催案内を行っています。 <https://www.qst.go.jp/site/kansai-topics/29853.html>

97	14-APR-2023	Dr. Paul Mason	Science & Technology Facilities Council, Rutherford Appleton Laboratory, Oxfordshire, UK
	The Extreme Photonics Applications Centre: A New Facility for Ultrafast Science & Applications in the UK		
98	16-JUN-2023	Dr. Kenta Kitano	Department of Physical Sciences, Aoyama Gakuin University
	Superfluorescence from rubidium vapor ~ Results with heated gas cells and prospects for experiments with cold atoms ~		
99	19-JUN-2023	Dr. Sanasam Sunderlal Singh	Department of Mechanical Engineering, Indian Institute of Technology, Madras
	Near-infrared femtosecond laser writing of controlled surface wettability		
100	23-JUN-2023	山本 佳世子 論説委員 兼 編集 局科学技術部編集委員	日刊工業新聞社
	書かれてなんぼ、プレスリリースの真価とは		
101	28-OCT-2023	Assoc. Prof. Yu-ichiro Matsushita	National University Corporation Tokyo Institute of Technology
	Implementation of imaginary-time evolution method on a quantum computer and its applications to quantum chemical calculations		
102	20-NOV-2023	Dr. Hikaru Souda	Graduate School of Medicine, Yamagata University
	Present and Future Accelerator Performance for Carbon Ion Radiotherapy		

103	11-DEC-2023	Dr. Tenio Popmintchev	University of California San Diego
Quantum Optics Meets Strong Field Physics: Novel Regimes of Coherent X-ray Generation with Strong Electron Correlation Dynamics and Attosecond Rabi Oscillations			
104	26-JAN-2024	Assoc. Prof. Zhong Yin	International Center for Synchrotron Radiation Innovation Smart, Tohoku University
Ultrafast Spectroscopy with Modern Light Sources			



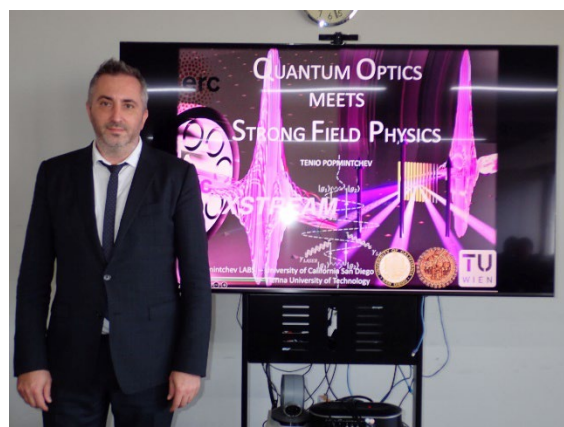
第 98 回 青山学院大学  
北野 健太 博士



第 99 回 インド工科大学  
Dr. Sanasam Sunderlal Singh



第 100 回 日刊工業新聞  
山本 佳世子 氏 (写真中央)



第 103 回 カリフォルニア大学  
Dr. Tenio Popmintchev

### QST 播磨セミナー (第 31 回～第 39 回)

播磨地区では QST 内の研究者や国内外の著名な研究者によるセミナーを開催しています。2023 年度も他拠点からも広く参加をしていただきやすいようにオンライン開催としました。

31	26-JUL-2023	Dr. Takashi Ikeda	Hydrogen Materials Research Group, QST
Simulating Vibrational Spectra of Hydrogen Clathrate Hydrates Using First Principles Molecular Dynamics			

32	30-AUG-2023	Dr. Kosuke Fujiwara	Magnetism Research Group, QST
	Development of Synchrotron-based Mössbauer Microscope		
33	15-SEP-2023	Prof. Kaoru Mizuno	Faculty of Education, Shimane University
	X-ray Topography and Its Application for Characterization of Diamond Crystal		
34	20-SEP-2023	Dr. Hideaki Iwasawa	Advanced Spectroscopy Research Group, QST
	Spin-resolved ARPES on High-Tc Cuprate Superconductors		
35	25-OCT-2023	Dr. Kenji Ohwada	Coherent X-ray Research Group, QST
	Structural Properties Research Using Coherent X-rays - From Relaxors to Nanocrystals		
36	22-NOV-2021	Dr. Kento Sugawara	Beamline Operation Office, QST
	Development of Bulk-sensitive Magnetic Microscope Utilizing X-ray Magnetic Circularly Polarized Emission		
37	24-JAN-2024	Dr. Hiroyuki Saitoh	Hydrogen Materials Research Group, QST
	Synthesis Study of Novel Hydride with The Aid of In-situ Synchrotron Radiation X-ray Diffraction Observation and Its Future Plan		
38	21-FEB-2024	Dr. Takuji Nomura	Magnetism Research Group, QST
	Theoretical study of x-ray magnetic circular dichroism based on first-principles band calculations		
39	26-MAR-2024	Dr. Kenji Tsutsui	Advanced Spectroscopy Research Group, QST
	Theoretical Study of Magnetic Excitations in Photoexcited Antiferromagnetic Mott Insulators		

### S-cube (スーパーサイエンスセミナー)

中学高校生を中心に一般の方に光量子科学についての理解を深めていただくことを目的に、第一線の研究者による講義「S-cube (エスキューブ：スーパーサイエンスセミナー)」を開講しています。2023年度は合計12回(第222回～第233回)開催しました。

<https://www.qst.go.jp/site/kansai-topics/29911.html>

222	16-May-2023	畑 昌育	レーザー駆動イオン加速器開発プロジェクト	34人参加
	レーザーでつくる夢のイオンビーム？次世代がん治療装置の最前線			
223	8-Aug-2023	田中 淳	関西光量子科学研究所長	23人参加
	QST 関西研の量子科学技術研究について			

224	25-Aug-2023	畑 昌育	レーザー駆動イオン加速器開発プロジェクト	12人参加
			レーザーでつくる夢のイオンビーム～次世代がん治療装置の最前線～	
225	20-Oct-2023	小島 完興	レーザー駆動イオン加速器開発プロジェクト	20人参加
			レーザーでつくる夢のイオンビーム～次世代がん治療装置の最前線～	
226	23-Oct-2023	近藤 康太郎	高強度場科学研究グループ	13人参加
			ハイパワーレーザーが拓く新しい科学の世界	
227	8-Nov-2023	福田 祐仁	光量子ビーム科学研究部	42人参加
			光の不思議を解き明かそう「偏光と複屈折」	
228	10-Nov-2023	田中 淳	関西光量子科学研究所長	33人参加
			関西光量子科学研究所の研究紹介	
229	22-Nov-2023	James Kevin Koga	高強度場科学研究グループ	25人参加
			Overview of High Intensity Laser-Matter Interaction Physics	
230	1-Dec-2023	宮坂 泰弘	先端レーザー科学研究グループ	17人参加
			超高強度レーザー「J-KAREN-P」と身の回りのレーザー	
231	29-Jan-2024	赤松 憲	DNA損傷化学研究チーム	8人参加
			放射線によってできるDNAの傷とその種類、生物による損傷修復の方法について	
232	1-Feb-2024	小島 完興	レーザー駆動イオン加速器開発プロジェクト	42人参加
			レーザーでつくる夢のイオンビーム～次世代がん治療装置の最前線～	
233	14-Feb-2024	近藤 康太郎	高強度場科学研究グループ	20人参加
			ハイパワーレーザーが拓く新しい科学の世界	



左：第 227 回 東京工業大学附属科学技術高等学校 S-cube での実験の様子  
 右：第 230 回 三重県立上野高等学校 (S-cube)

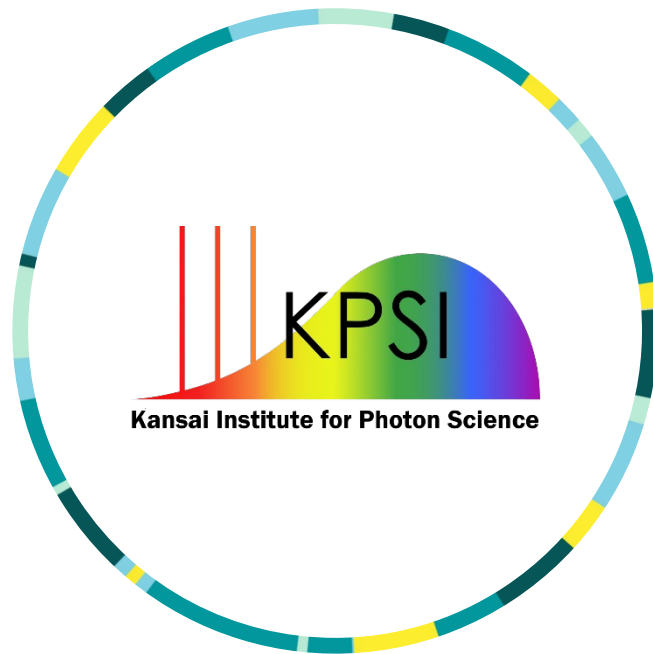
関西光量子科学研究所2023年度年報  
KPSI Annual Report 2023

【発行】  
2024(令和6)年6月

【編集・発行】  
国立研究開発法人量子科学技術研究開発機構  
関西光量子科学研究所 管理部庶務課

©2024 国立研究開発法人量子科学技術研究開発機構





**Kansai Institute for Photon Science**  
**National Institutes for Quantum Science and Technology**

8-1-7, Umemidai, Kizugawa-shi, Kyoto 619-0215, Japan  
<https://www.qst.go.jp/site/kansai/>